bioRxiv preprint doi: https://doi.org/10.1101/456574; this version posted October 30, 2018. The copyright holder for this preprint (which was not certified by peer review) is the author/funder, who has granted bioRxiv a license to display the preprint in perpetuity. It is made available under aCC-BY-NC 4.0 International license.

Complementary networks of cortical somatostatin interneurons enforce layer specific control

Alexander Naka[1], Julia Veit[1], Ben Shababo[1], Rebecca K. Chance[2], Davide Risso[3,4], David Stafford[2], Benjamin Snyder[2], Andrew Y. Egladyous[2], Desi Chu[2], Savitha Sridharan[2], Liam Paninski[5,6,7,8], John Ngai[1,2,9], and Hillel Adesnik[1,2,10]

[1]Helen Wills Neuroscience Institute, [2]Department of Molecular and Cell Biology, and [9]QB3 Functional Genomics Laboratory at the University of California, Berkeley; Berkeley, California, USA

[3]Department of Statistical Sciences, University of Padova; Padova, Italy, and [4]Division of Biostatistics and Epidemiology, Department of Healthcare Policy and Research at Weill Cornell Medicine; New York, NY

[5]Neurobiology and Behavior Program, [6]Center for Theoretical Neuroscience, [7]Departments of Statistics and Neuroscience, and [8]Grossman Center for the Statistics of Mind at Columbia University; New York, USA.

[10]Corresponding author

Abstract

The neocortex is organized into discrete layers of excitatory neurons: layer 4 receives the densest 'bottom up' projection carrying external sensory data, while layers 2/3 and 5 receive 'top down' inputs from higher cortical areas that may convey sensory expectations and behavioral goals. A subset of cortical somatostatin (SST) neurons gate top down input and control sensory computation by inhibiting the apical dendrites of pyramidal cells in layers 2/3 and 5. However, it is unknown whether an analogous inhibitory mechanism separately and specifically controls activity in layer 4. We hypothesized that distinct SST circuits might exist to inhibit specific cortical layers. By enforcing layer-specific inhibition, distinct SST subnetworks could mediate pathway-specific gain control, such as regulating the balance between bottom up and top down input. Employing a combination of high precision circuit mapping, *in vivo* optogenetic perturbations, and single cell transcriptional profiling, we reveal distinct and complementary SST circuits that specifically and

bioRxiv preprint doi: https://doi.org/10.1101/456574; this version posted October 30, 2018. The copyright holder for this preprint (which was not certified by peer review) is the author/funder, who has granted bioRxiv a license to display the preprint in perpetuity. It is made available under aCC-BY-NC 4.0 International license.

reciprocally interconnect with excitatory cells in either layer 4 or layers 2/3 and 5. Our data further define a transcriptionally distinct SST neuronal sub-class that powerfully gates bottom up sensory activity during active sensation by regulating layer 4 activity. This integrated paradigm further represents a potentially generalizable approach to identify and characterize neuronal cell types and reveal their *in vivo* function.

Keywords: cerebral cortex; interneuron; somatostatin; neural circuit; inhibition; cortical layers; optogenetics; connectivity; mouse; barrel cortex

Introduction

The neocortex is divided across its vertical axis into discrete layers. Excitatory principal cells (PCs) in each layer differentially encode and process sensory information[1,2], due in part to the fact that they receive different external inputs. 'Bottom-up' sensory inputs primarily enter L4, while 'top down' inputs target PCs in supragranular and infragranular layers. The relative impact of these two main input pathways is likely to be crucial for sensory-guided behavior. Dendrite-targeting somatostatin (SST)-expressing interneurons are well known for shaping sensory coding through lateral and recurrent inhibition, and for gating top-down input by regulating dendritic spiking and synaptic plasticity[3–10]. While it is well established that SST neurons send and receive synaptic connections with neurons across multiple cortical layers[11–17], it is unclear whether SST circuits impact all layers in a global manner, or if instead they selectively control specific layers, which could have profound impacts for cortical computation.

bioRxiv preprint doi: https://doi.org/10.1101/456574; this version posted October 30, 2018. The copyright holder for this preprint (which was not certified by peer review) is the author/funder, who has granted bioRxiv a license to display the preprint in perpetuity. It is made available under aCC-BY-NC 4.0 International license.

Studies which have examined connectivity of SST cells[18] and GABAergic interneurons more generally[19–22] have found that inhibitory neurons interconnect with excitatory cells densely and non-selectively, which has led to the emerging hypothesis that excitatory circuits are overlaid by a 'blanket of inhibition'. While these studies have usually focused on connectivity within a single layer, one possibility is that this principle generalizes to the rest of the circuit, meaning that SST cells wire up irrespective of layer to globally regulate cortical networks. However, the SST population is highly heterogeneous[7,23] and can be divided into multiple subgroups of cells which exhibit distinct electrophysiological, morphological, genetic[24], and *in vivo* functional properties[4,5,25–28]. Intriguingly, some of these subgroups target their axons to different laminar domains[29–31], and it has been hypothesized that subgroups of SST cells might be specialized to differentially modulate the activity of specific layers[25], perhaps by forming distinct subnetworks. Such an architecture would allow for independent gating of different cortical pathways by complementary networks of SST interneurons.

We addressed these contrasting hypotheses by combining high-resolution optogenetic circuit mapping, paired intracellular recordings, single-cell RNA sequencing, and *in vivo* optogenetics. With a focus on SST neurons in layer 5, the layer in which they are most numerous, we identified two distinct sub-networks of SST neurons with strikingly contrasting connectivity and *in vivo* function. The first sub-group of SST neurons was composed of Martinotti cells (MCs), a well-studied cell type which has classically been defined by its ascending axonal projection to L1. The second subgroup was morphologically, transcriptionally, and synaptically distinct from MCs and composed of SST neurons that primarily target L4 instead of L1. The connectivity and function of this second

bioRxiv preprint doi: https://doi.org/10.1101/456574; this version posted October 30, 2018. The copyright holder for this preprint (which was not certified by peer review) is the author/funder, who has granted bioRxiv a license to display the preprint in perpetuity. It is made available under aCC-BY-NC 4.0 International license.

sub-class of SST neurons, which have sometimes been referred to simply as 'non-Martinotti' cells or 'NMCs' [25,29,31], are largely unknown.

Our data on L5 SST neurons show that these two SST subgroups comprise highly distinct inhibitory subnetworks that exhibit exquisitely specific and strikingly complementary laminar patterns of connectivity and *in vivo* impact. MCs receive input from L2/3 and L5, whereas NMCs receive input from L4 and L6. In turn, MCs provide reciprocal inhibition to PCs in L5 but not to those in L4, while NMCs selectively inhibit PCs in L4. Optogenetically activating MCs and NMCs *in vivo* results in extremely distinct laminar patterns of suppression, suggesting they may have contrasting roles in sensory computation and behavior. Single-cell RNA sequencing on >2,000 individual SST neurons revealed transcriptomically defined SST sub-classes that showed distinct somal lamination profiles across the cortical range of depth. Taken together, these results demonstrate that of these, two major subgroups of cortical SST cells, by virtue of their layer-selective synaptic connectivity, can independently modulate the activity of different cortical layers during sensation. This highly selective synaptic and functional architecture supports a model in which distinct sub-networks of SST neurons may fine tune the balance of activity across the layers of the neocortex.

Results

Two distinct sub-networks of SST neurons defined by layer-specific connectivity

To probe the synaptic architecture of SST circuits, we employed a combination of one and two photon optogenetics, single cell reconstructions, and paired recording. To make targeted recordings from SST neurons belonging to putatively different sub-classes, we

bioRxiv preprint doi: https://doi.org/10.1101/456574; this version posted October 30, 2018. The copyright holder for this preprint (which was not certified by peer review) is the author/funder, who has granted bioRxiv a license to display the preprint in perpetuity. It is made available under aCC-BY-NC 4.0 International license.

took advantage of transgenic reporter mouse lines that label either all SST neurons (*Sst*-IRES-Cre)[32], or different anatomical sub-classes of SST neurons in the barrel cortex (GIN, X94, and X98)[29,33]. We focused our investigation on SST neurons in L5 which harbors a large and diverse population of SST cells[34,35]. Consistent with prior data, the anatomy and intrinsic physiology of L5 GIN cells demonstrated that they are MCs (41/44; 93%; Fig. 1a and Fig. S1)[36–39]. By similar analyses, neurons in the X94 line were non-Martinotti cells (32/35; 91%), which formed a dense axonal plexus in L4 rather than L1 (Fig. 1a, Fig. S2) and exhibited quasi-fast-spiking electrophysiological phenotypes (Fig. 1b, Fig. S1). While the X94 line labels only ~15% of SST cells in L5[29], additional recordings from L5 SST-TdT cells suggested that the X94 line subsamples the NMC population (consistent with a previous report) since 30 - 40% of recorded L5 SST cells exhibited an NMC phenotype (Fig. S1c-g; Supplementary Text). Aligning biocytin reconstructions of L5 MCs and NMCs revealed that these two populations have strikingly complementary vertical profiles of neurite density: MCs primarily innervated layers 1, 2/3 and 5, and NMCs primarily innervated L4 and the L5/L6 border (Fig. 1c). Although some is known about their differing anatomical and physiological features[25,29,31], relatively little is understood about how these two sub-classes of SST neurons, especially NMCs, might differentially integrate into and influence the cortical excitatory network.

To begin to answer this question, we first asked whether MCs and NMCs receive different patterns of excitatory inputs across the cortical layers. We transgenically expressed ChR2 in cortical excitatory neurons across all layers, and used scanning photostimulation to map the spatial profile of excitatory inputs to NMCs and MCs (Fig. 1d,e,f; Fig. S4). Remarkably, we found that L5 MCs and NMCs receive inputs from highly

bioRxiv preprint doi: https://doi.org/10.1101/456574; this version posted October 30, 2018. The copyright holder for this preprint (which was not certified by peer review) is the author/funder, who has granted bioRxiv a license to display the preprint in perpetuity. It is made available under aCC-BY-NC 4.0 International license.

specific and largely non-overlapping sources. MCs, but not NMCs, frequently received excitatory input from either upper L5, L2/3, or from both L2/3 and L5, but received little input from L4 or L6, broadly consistent with prior studies[11,12,14,17]. In contrast, NMCs received strong input from L4 and/or the L5B/L6 border (Fig. 1e,f; input from L4 and L6 was 62 ± 7% of total input for n = 14 NMCs versus 25 ± 3% for n = 15 MCs; $p = 6.5 \cdot 10^{-10}$; two sample T-test; see also Fig. S3) but relatively little input from L2/3 and L5. Thus, L5 MCs and NMCs appear to receive distinct and complementary patterns of excitatory innervation.

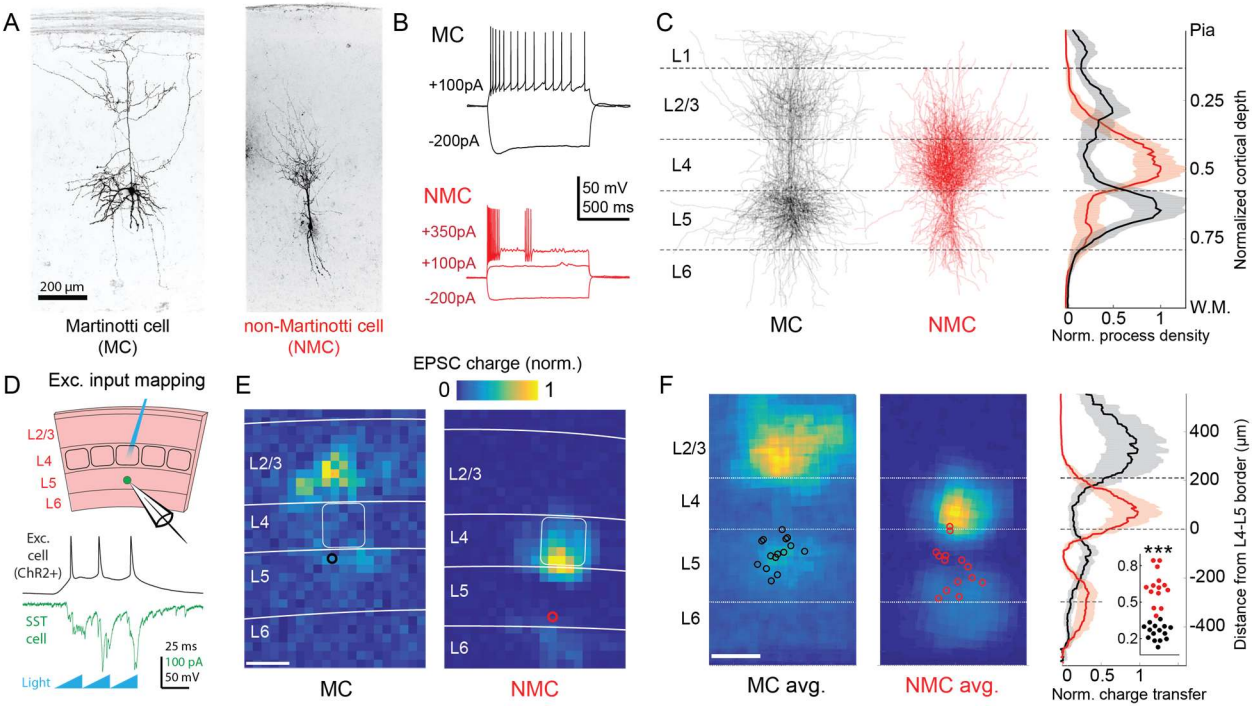

Figure 1. Optogenetic circuit mapping reveals complementary synaptic input patterns to two subtypes of L5 SST cells.

(A) Confocal images of dye filled neurons revealing two morphological phenotypes of L5 SST cells. Left: an L5 GIN cell. Right: an L5 X94 cell. Scale bar: 200 µm.

(B) Example traces during current step injections from an L5 GIN cell (black) and an L5 X94 cell (red).

bioRxiv preprint doi: https://doi.org/10.1101/456574; this version posted October 30, 2018. The copyright holder for this preprint (which was not certified by peer review) is the author/funder, who has granted bioRxiv a license to display the preprint in perpetuity. It is made available under aCC-BY-NC 4.0 International license.

(C) Left: Overlaid morphological reconstructions of L5 GIN/MC cells (black, n=14) and L5 X94/NMCs (red, n=10) showing differences in laminar distribution of neurites. Right: Normalized neurite density versus cortical depth for L5 GIN (black) and L5 X94 cells (red). Data are represented as mean ± C.I.

(D) Schematic of experimental configuration. A digital micromirror device was used to focally photo-stimulate excitatory cells in different regions of the slice in order to map the spatial profile of excitatory inputs to GFP+ L5 MCs (Emx1-Cre; GIN) or GFP+ L5 NMCs (Emx1-Cre; X94).

(E) Example heat maps of median EPSC charge transfer evoked at each stimulus site for example L5 SST cells. Left: An L5 MC that received inputs from L5 and L2/3. Right: An L5 NMC that received inputs from L4 and the L5/6 border. Soma locations are indicated by red/black bordered white dot). Scale bar: 200 μm.

(F) Left: Grand averages of input maps reveal cell-type specific patterns of laminar input. Soma locations are indicated as above. Right: Normalized charge transfer versus distance from L4-L5 border for MC (black) and NMC (red) populations. Scale bar: 200 μm.

Inset: Swarm plots showing the proportion of total evoked charge transfer in each map that originated from sites in L4+L6, i.e. [L4+L6] / [L2/3+L4+L5+L6] for the MC (black; median, 27%; range, 13-36%) and NMC (red; median, 62%; range, 38-84%) populations. Proportions were significantly different between L5 MCs and L5 NMCs (25 ± 3% in n = 15 MCs versus 62 ± 7% in n = 14 NMCs, mean ± C.I.; $p = 6.5 \cdot 10^{-10}$; two-sample t-test)

See also Figures S1-4.

The striking laminar differences in inputs to NMCs and MCs suggested that they might be differentially recruited by activity of different cortical layers. To test this possibility, we specifically photo-stimulated L4 excitatory neurons via Cre-dependent expression of ChR2 in *Scnn1*-Cre mice (crossed to GIN or X94; Fig. 2a). L4-specific photo-stimulation (with two different stimulus protocols, across four different intensities) drove large EPSCs in NMCs but evoked little to no input in MCs under identical conditions (Fig. 2b,c; Fig. S5). Current clamp recordings under the same conditions showed that L4 photo-stimulation reliably drove spiking in L5 NMCs, but not in L5 MCs (Fig. 2b,d; Fig. S5) despite the fact that MCs are intrinsically more excitable than NMCs (Fig. S1). The lack of evoked responses in MCs was not due to differences in the degree of L4 activation (see supplementary text and Fig. S5 for controls). Thus, these results indicate a stark difference

bioRxiv preprint doi: https://doi.org/10.1101/456574; this version posted October 30, 2018. The copyright holder for this preprint (which was not certified by peer review) is the author/funder, who has granted bioRxiv a license to display the preprint in perpetuity. It is made available under aCC-BY-NC 4.0 International license.

between L5 NMCs and MCs: L4 densely innervates and powerfully drives firing in L5 NMCs, but not L5 MCs.

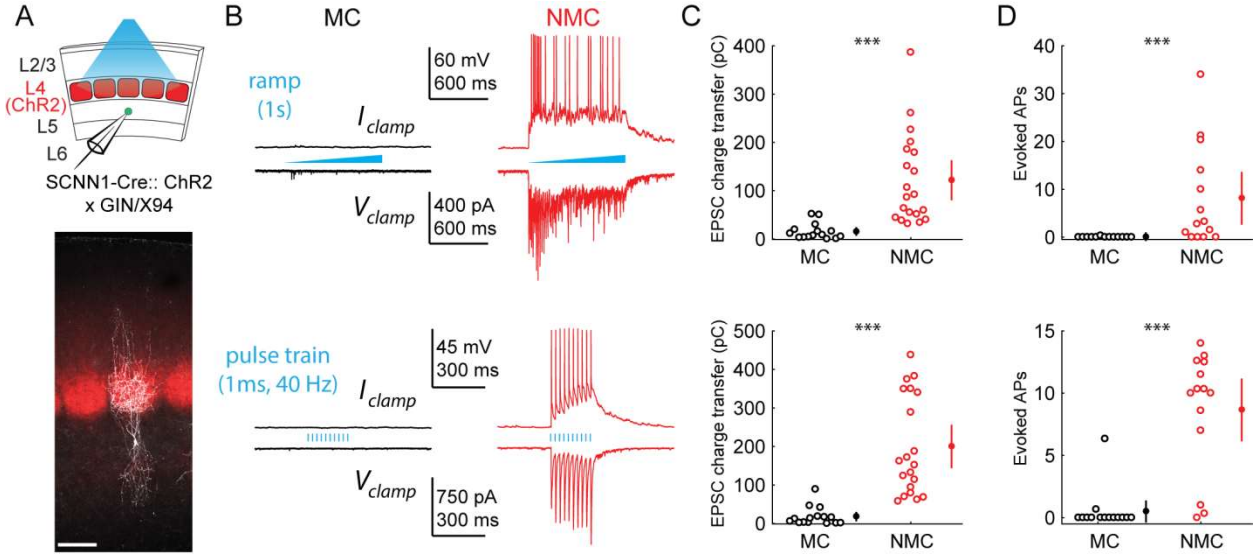

Figure 2. L4 photo-stimulation excites L5 NMCs but not L5 MCs

(A) Top: Schematic of the experimental configuration. L5 X94 or GIN cells were recorded during photo-stimulation of L4 excitatory neurons. Bottom: Confocal image of a filled L5 X94 neuron (white) with ChR2-TdTomato expression (red) visible in L4. Scale bar: 150 µm.

(B) Top row: Example traces recorded in the current clamp (upper traces) or voltage clamp (lower traces) configurations during a 1-second ramp photo-stimulation. Bottom row: As above, but for photo-stimulation with a 40 Hz train of ten 1ms pulses.

(C) Quantification of excitatory charge transfer during maximum intensity 1-second ramp stimulation trials. Mean 122 ± 41 pC in n = 20 NMCs versus 15 ± 8 pC in n = 15 MCs; $p = 3.9 \cdot 10^{-6}$, Wilcoxon rank sum test.

(D) Quantification of the mean number of evoked action potentials during maximum intensity 1-second ramp stimulation trials. Mean 8.1 ± 5.5 spikes per trial in n = 15 NMCs versus 0.03 ± 0.05 spikes per trial in n = 15 MCs; $p = 6.6 \cdot 10^{-4}$, Wilcoxon rank sum test.

(E) As in C, for maximum intensity 40Hz pulse train stimulation. Mean 200 ± 56 pA in n = 20 NMCs versus 18 ± 12 pA in n = 15 MCs; $p = 2.8 \cdot 10^{-6}$, Wilcoxon rank sum test.

(F) As in D, for maximum intensity 40Hz pulse train stimulation. Mean 8.7 ± 2.4 spikes per trial in n = 15 NMCs versus 0.5 ± 0.9 spikes per trial in n = 15 MCs; $p = 1.5 \cdot 10^{-6}$, Wilcoxon rank sum test.

Error bars denote mean ± 95% confidence interval. Three asterisks denotes p<0.001. See also Figure S5.

bioRxiv preprint doi: https://doi.org/10.1101/456574; this version posted October 30, 2018. The copyright holder for this preprint (which was not certified by peer review) is the author/funder, who has granted bioRxiv a license to display the preprint in perpetuity. It is made available under aCC-BY-NC 4.0 International license.

Common input mapping reveals subnetwork structure in L5 SST cell output

We next asked whether NMCs and MCs also exhibit layer-specificity in their inhibitory outputs. Since SST cells have been implicated in generating feedback inhibition [3,17,40], we hypothesized that MCs and NMCs might target their inhibitory outputs in order to reciprocally inhibit the same PC populations that excite them. For example, NMCs but not MCs would inhibit L4 PCs, whereas MCs but not NMCs would inhibit L5 PCs. Alternatively, MCs, NMCs, or both cell types could globally target PCs within and across layers non-selectively. To address this, we used two photon optogenetic circuit mapping to determine whether the outputs of individual SST cells (in the non-specific SST-Cre line) diverge onto PCs in multiple layers. If individual SST cells target either L4 or L5 PCs, but not both, then we should never observe common input to pairs of L4 and L5 PCs when photo-stimulating single SST neurons. This can be tested by mapping optogenetically evoked unitary SST inhibitory connections onto multiple PCs recorded simultaneously and analyzing the spatiotemporal coincidence of evoked IPSCs onto different pairs of PCs, thereby measuring the amount of common input shared between pairs of PCs in different layers[41,42,43]. Although this approach does not discriminate between MCs and NMCs directly, it performs a more stringent test by extending our hypothesis to apply to the structure of the outputs of the L5 SST population as a whole, rather than the sparser subsets set labeled in the GFP lines. To maximize the spatial precision of photo-stimulation we used a soma-targeted opsin (Fig. 3a,b,c)[44] and computer-generated holography (Fig. 3a,b; Fig. S9a). Since SST → PC synapses are often located on the distal dendrites of PCs, we recorded IPSCs using a cesium-based internal solution, and took additional steps to minimize false negatives (see

bioRxiv preprint doi: https://doi.org/10.1101/456574; this version posted October 30, 2018. The copyright holder for this preprint (which was not certified by peer review) is the author/funder, who has granted bioRxiv a license to display the preprint in perpetuity. It is made available under aCC-BY-NC 4.0 International license.

Methods). Using this method, we simultaneously mapped SST inputs to pairs of L4-L5 PCs and L5-L5 PCs (Fig. 3d,e,f; Fig. S10f).

In L4-L5 PC pairs we observed very little common input when photo-stimulating SST neurons, but substantial common input in L5-L5 pairs (2.4 ± 1.3% spatially coincident inputs out of all input locations in n = 10 L4-L5 pairs, versus 28 ± 6.7% in n = 10 L5-L5 pairs; $p = 1.2 \cdot 10^{-3}$, Wilcoxon rank sum test). Given that occasionally more than one SST cell might be photostimulated at any given target location (Fig. S9d,g), we employed a statistical test for fine time scale synchrony of IPSCs between the patched cells at each candidate location (where both cells received input) to determine whether the IPSCs truly arose from a single SST cell diverging onto both recorded PCs (Amarasingham et al., 2012, Fig. 3g, Fig. S10g,h,i,j). Using this far more conservative test for the detection of common input, we detected no locations in which stimulation evoked common inputs for L4-L5 pairs, whereas we detected at least one common input in 7 of 10 L5-L5 pairs (Fig 3h; no locations in n = 10 L4-L5 pairs versus 13.7 ± 5.1% of all input locations in n = 10 L5-L5 pairs; $p = 1.1 \cdot 10^{-3}$, Wilcoxon rank sum test; see also Fig. S10k). These data argue that individual L5 SST cells connect to either L4 PCs or to L5 PCs, but never to both. In other words, L4 PCs and L5 PCs are inhibited by non-overlapping subnetworks of L5 SST cells.

bioRxiv preprint doi: https://doi.org/10.1101/456574; this version posted October 30, 2018. The copyright holder for this preprint (which was not certified by peer review) is the author/funder, who has granted bioRxiv a license to display the preprint in perpetuity. It is made available under aCC-BY-NC 4.0 International license.

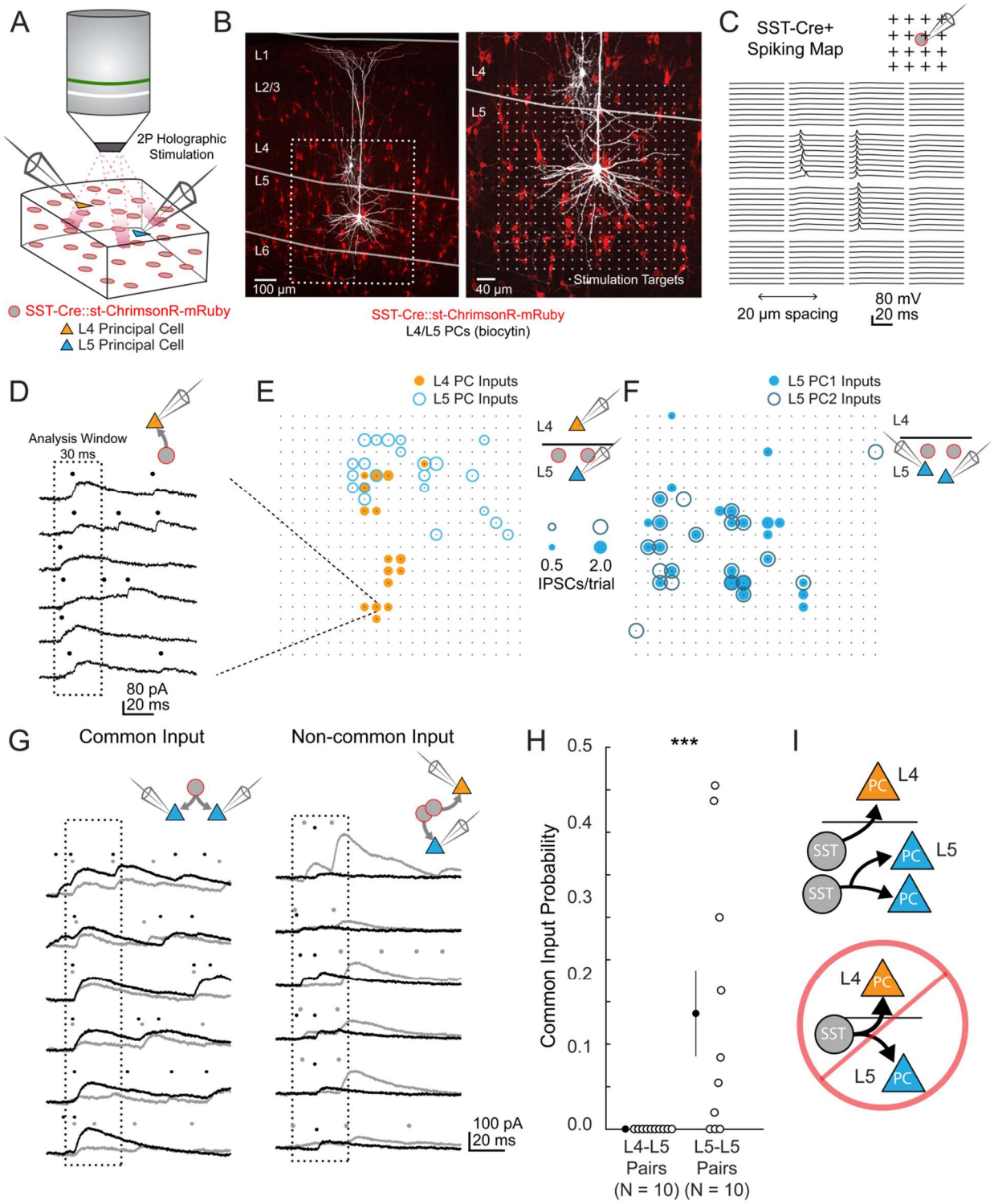

Figure 3. 2 photon optogenetic circuit mapping reveals that L4 and L5 PCs are inhibited by separate populations of L5 SST cells.

bioRxiv preprint doi: https://doi.org/10.1101/456574; this version posted October 30, 2018. The copyright holder for this preprint (which was not certified by peer review) is the author/funder, who has granted bioRxiv a license to display the preprint in perpetuity. It is made available under aCC-BY-NC 4.0 International license.

(A) Schematic of the experimental configuration. IPSCs are recorded from a pair of PCs (either an L4/L5 pair or an L5/L5 pair) while SST cells expressing soma-targeted ChrimsonR-mRuby2 are focally activated using 2P photo-stimulation and computer generated holography.

(B) Left: post-hoc confocal image showing SST cells expressing soma-targeted-ChrimsonR-mRuby2 (red) and biocytin fills of recorded PCs in L4 and L5 (white) at 10x magnification. Right: Confocal image at 20x magnification showing the grid of photo-stimulated target locations. Both images are max z-projections over 100 μm.

(C) Spatial photo-excitation profile of a soma-targeted-ChrimsonR-mRuby2 expressing SST cell. Whole cell current-clamp recordings from this cell showing multiple trials of photo-stimulation at a 4 x 4 subsection of the photo-stimulation grid with 20 μm spacing between stimulation locations. The SST cell is recruited to spike only at a small number of stimulation sites, but does so reliably and with low jitter across trials at these sites.

(D) Example traces showing IPSCs recorded from an L4 PC during SST photo-stimulation at a single site (corresponding to black boxed square in E) over multiple trials. Dots above each trace indicate the onset time of detected IPSCs ($p = .0003$, Poisson detection).

(E) Example overlay of maps showing the mean number of IPSCs at detected input locations during photo-stimulation for a simultaneously recorded L4 PC-L5 PC pair. Bubble size indicates the mean number of IPSCs evoked (deviation from background rate) per trial.

(F) As in E, but for an L5 PC-L5 PC pair.

(G) Example traces illustrating method for detection of common SST-mediated inputs to pairs of simultaneously recorded PCs. Left: IPSC traces at a single site recorded simultaneously in two PCs (each PC is indicated by black or grey traces) and corresponding detected IPSCs. IPSCs with synchronous onset occur in many trials, despite the trial-to-trial jitter in IPSC onset, suggesting that a SST cell which diverges onto both recorded PCs is being stimulated at this site ($p = .0005$, synchrony jitter test). Right: IPSC traces from a different site. Evoked IPSCs are observed in both cells, but the lack of synchronicity suggests they arise from separate, neighboring SST cells ($p = .4$). Dots above each trace indicate the estimated onset time of detected IPSCs.

(H) Probability of detecting common SST input per photo-stimulated site for pairs consisting of L4 PCs and L5 PCs versus pairs consisting of two L5 PCs. No common input locations were detected in $n = 10$ L4-L5 pairs versus 13.7 ± 5.1% of all input locations locations stimulated in $n = 10$ L5-L5 pairs; $p = 1.1 \cdot 10\text{-}3$, Wilcoxon rank sum test Data are summarized by mean ± S.E.M.

(I) Schematic of main result for SST outputting mapping. Individual L5 SST cells form inhibitory connections onto L4 PCs and or L5 PCs but not both. See also Figure S9, S10.

Paired recordings show dense, reciprocal, and selective intra- and translaminar connectivity

bioRxiv preprint doi: https://doi.org/10.1101/456574; this version posted October 30, 2018. The copyright holder for this preprint (which was not certified by peer review) is the author/funder, who has granted bioRxiv a license to display the preprint in perpetuity. It is made available under aCC-BY-NC 4.0 International license.

To unequivocally confirm the input/output mapping suggested by the optogenetic data presented above, we made paired intracellular recordings between both types of SST neurons and PCs in L4 and L5. We targeted L5 MCs and NMCs with the GIN and X94 lines as above, but also used the SST-TdT line to identify L5 SST cells more generally, and classified SST-TdT cells as putative MCs or NMCs based on their electrophysiological properties (Fig. S1g; Table S1) and/or morphology. We observed extremely frequent L5 NMC → L4 PC connections (36/67 pairs tested; 54%; Fig. 4a,b), even across long inter-somatic distances (183 ± 67 μm, mean ± S.D.; Fig. S6), suggesting that L5 NMCs connect densely onto L4. In the opposite direction, we also frequently observed monosynaptic excitatory connections from L4 PCs onto L5 NMCs, consistent with the optogenetic experiments above (39/72 pairs tested; 54%). These synapses exhibited profound facilitation during sustained high-frequency firing in the presynaptic cell (Fig. 4a; Fig. S8), the hallmark of excitatory connections onto SST cells[17,46,47]. In cases where we tested connectivity bidirectionally, we frequently observed reciprocal connections (23/56 pairs tested; 41%). Thus, L5 NMCs and L4 PCs form a translaminar feedback inhibitory motif. We also observed frequent connections from L5 NMCs onto L4 fast-spiking (FS) cells (12/23 pairs tested; 52%; Fig. S7), similar to a known circuit in which L4 non-Martinotti SST cells inhibit L4 FS cells[29,48].

In contrast, we almost never observed monosynaptic excitatory connections from L4 PCs to L5 MCs (1/95 pairs tested; 1%; Fig. 4a,b) or from L5 MCs onto L4 PCs (4/68 pairs tested; 6%), despite the fact that these pairs were separated by smaller inter-somatic distances than L4 PC - L5 NMC pairs (143 ± 47 μm, mean ± S.D.; Fig. S6). In a subset of these experiments, we recorded from L4 PCs in the voltage clamp configuration at +10mV (using a cesium-based internal solution), but did not observe connections any more

bioRxiv preprint doi: https://doi.org/10.1101/456574; this version posted October 30, 2018. The copyright holder for this preprint (which was not certified by peer review) is the author/funder, who has granted bioRxiv a license to display the preprint in perpetuity. It is made available under aCC-BY-NC 4.0 International license.

frequently (0/38 pairs tested; 0%). These data suggest that L5 NMCs are integrated into the densely interconnected network of L4 PCs and interneurons[49,50], whereas L5 MCs are essentially isolated from it.

We next sought to confirm the notion raised by our 2P mapping experiments that L5 MCs would specifically and reciprocally connect to L5 PCs, while NMCs would not. Indeed, we observed frequent inhibitory connections from L5 MCs onto L5 PCs (24/46 pairs tested; 52%; Fig. 4c,d), in agreement with prior literature[12,18,51]. We also observed excitatory connections from L5 PCs onto L5 MCs, albeit more rarely (4/29 pairs tested; 14%; Fig. 4c,d) but at a rate consistent with the literature [12,52]. In contrast, we detected very few inhibitory outputs from L5 NMCs onto L5 PCs (2/65 pairs tested; 3%; Fig. 4c,d) or excitatory connections from L5 PCs onto L5 NMCs (1/60 pairs tested; 2%; Fig. 3c,d), despite the fact that L5 PCs were on average located much closer to L5 NMCs than were L4 PCs. The surprising dearth of intralaminar connectivity between L5 PCs and L5 NMCs stands in stark contrast to the dense intralaminar connectivity observed between L5 PCs and L5 MCs, as well as in other inhibitory circuits[18,22,52]. Furthermore, our finding that MCs and NMCs specifically target L5 PCs and L4 PCs very closely replicates results from a recent study[31], lending further support to the notion that MCs and NMCs are wired into selective subnetworks with distinct laminar populations.

bioRxiv preprint doi: https://doi.org/10.1101/456574; this version posted October 30, 2018. The copyright holder for this preprint (which was not certified by peer review) is the author/funder, who has granted bioRxiv a license to display the preprint in perpetuity. It is made available under aCC-BY-NC 4.0 International license.

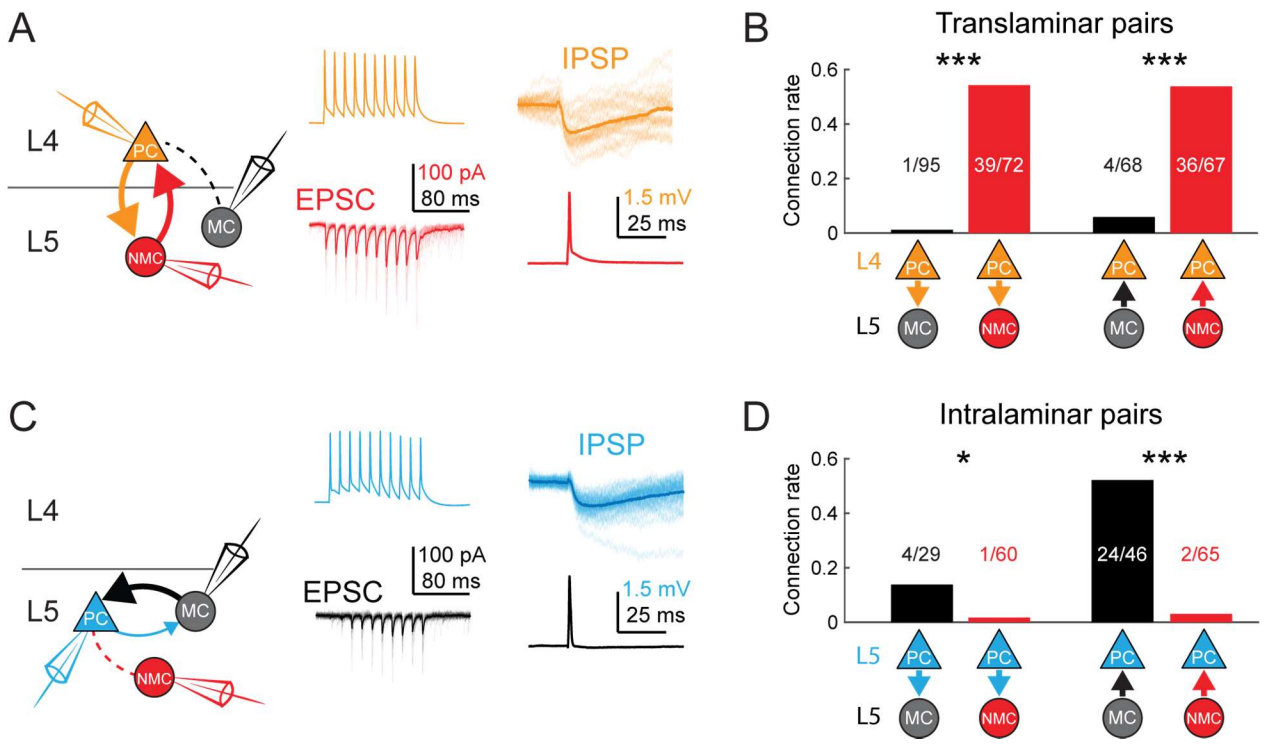

Figure 4. MCs and NMCs exhibit different patterns of monosynaptic connectivity with L4 and L5 PCs.

(A) Paired recordings of L4 PCs (orange) and L5 NMCs/MCs (red/black).). Left: schematic of the tested circuit. Middle: example traces of evoked spikes in a L4 PC (orange) and the excitatory synaptic current in a L5 NMC (red). Right: example traces of evoked IPSPs in a L4 PC (orange) in response to a single action potential in a L5 NMC (red).

(B) Bar graph summarizing translaminar connection rates between L4 PCs and L5 MCs (black bars) and L4 PCs and L5 NMCs (red bars). $p < 10^{-6}$ for L4PC→L5MC (n = 95 connections tested onto 39 MCs) versus L4 PC→L5 NMC connection rate (n = 72 connections tested onto 51 NMCs); $p = 2{\cdot}10^{-6}$ for L5MC→L4PC (n = 68 connections tested from 35 MCs) versus L5 NMC →L4PC connection rate (n = 67 connections tested from 51 NMCs); Monte Carlo permutation test.

(C) As in A, but intralaminar pairs between L5 MCs/NMCs and L5 PCs (blue).

(D) As in B, but for intralaminar connections with L5 PCs. p = 0.020 for L5 PC→L5 MC (n = 29 connections tested onto 20 MCs) versus L5 PC→L5 NMC connection rate (n = 60 connections tested onto 35 NMCs); $p<10^{-6}$ for L5 MC→L5 PC (n = 46 connections tested from 30 MCs) versus L5 NMC →L5 PC connection rate (n = 65 connections tested from 37 NMCs); Monte Carlo permutation test.

See also Figures S6-8 and Table S1.

CRE-DOG enables genetic access to subtypes of SST cells

bioRxiv preprint doi: https://doi.org/10.1101/456574; this version posted October 30, 2018. The copyright holder for this preprint (which was not certified by peer review) is the author/funder, who has granted bioRxiv a license to display the preprint in perpetuity. It is made available under aCC-BY-NC 4.0 International license.

The highly specific connectivity revealed by our circuit mapping experiments suggests that MCs and NMCs are specialized for different functions in cortical computation. If this is the case, we would expect that manipulating the activity of these groups of interneurons will have different effects on cortical dynamics. Based on our circuit mapping results (Fig. 3, Fig. 4), we hypothesized that increasing NMC activity optogenetically would primarily affect L4, whereas increasing MC activity would impact neurons in L5, but not in L4. Since no recombinase driver line is available for NMCs, we sought to instead use the GFP lines themselves for selective expression of ChR2. To do this, we employed the CRE-Dependent-on-GFP (CRE-DOG) system which uses two split fragments of Cre recombinase, that unite as a functional Cre molecule only in the presence of GFP[53]. We co-injected AAVs to drive expression of the CRE-DOG system, along with an AAV driving flexed ChR2-TdT, into X94 and GIN mice in order to target ChR2-TdT to GFP+ SST cells in these mice.

In X94 mice injected with this cocktail (referred to hereafter as X94-ChR2 mice) we observed revealed a bright band of TdT+ axonal arborization in L4, indicating effective labeling of GFP+ NMCs (Fig. 5a,b). While nearly all TdTomato expression colocalized with GFP, we observed a small number of GFP-/TdT+ neurons, which mostly appeared to be pyramidal cells. This off-target expression is probably the result of CRE-DOG leakage, since injecting GFP- wildtype animals in the same manner also results in sparse expression of TdT in cortical neurons (Fig. S11c). However, most (232/267; 87%) TdT+ neurons were GFP+, indicating that CRE-DOG allows expression of ChR2-TdT in GFP+ X94 cells with high specificity. Furthermore, immunostaining confirmed that the large majority (240/267; 90%) of TdT+ cells expressed SST (Fig. S11d,e).

bioRxiv preprint doi: https://doi.org/10.1101/456574; this version posted October 30, 2018. The copyright holder for this preprint (which was not certified by peer review) is the author/funder, who has granted bioRxiv a license to display the preprint in perpetuity. It is made available under aCC-BY-NC 4.0 International license.

To confirm the efficacy and selectivity of optogenetically activating NMCs, we recorded IPSCs from PCs in layers 2- 6 while photo-stimulating X94 cells with blue light (Fig. 5c,d). Consistent with our previous experiments, NMC photostimulation reliably evoked powerful IPSCs in L4 PCs, whereas PCs in other layers usually received small IPSCs or showed no response (mean charge transfer ± C.I: L2/3 = 2.0 ± 1.4 pC; L4 = 10.7 ± 4.8 pC; L5 = 0.8 ± 0.5 pC; L6 = 1.1 ± 0.4 pC). At the population level, the evoked IPSC was only significant in L4 PCs (L2/3: $p = 0.41$, $n = 20$; L4: $p < 10^{-8}$, $n = 30$; L5: $p = 0.67$, $n = 27$; L6: $p = 0.84$, $n = 22$; F-test on linear mixed-effects model compared to baseline charge), though a small number of individual L2/3 PCs did exhibit substantial IPSCs. While this was expected for L2/3 and L5 PCs, the lack of evoked inhibition in L6 PCs is notable, since it suggests that the L6 to NMC connection is asymmetric, unlike the highly reciprocal connectivity pattern seen between L4 PCs and NMCs. It is important to note that we illuminated all layers non-selectively in these experiments (e.g. photostimulated X94 cells both within and outside of L5, though these likely have similar connectivity; see Supplementary note, Fig. S3) in order to mimic the pattern of activation we would expect to achieve during *in vivo* photostimulation in ensuing experiments. We conducted these experiments while pharmacologically blocking glutamatergic synaptic transmission, but observed very small or no EPSCs in response to photostimulation in a subset of experiments carried out without glutamatergic blockade (Fig. S11f). These results indicate that CRE-DOG can be used with the X94-GFP line to achieve specific optogenetic control of NMCs.

Unfortunately, we found that GIN mice were unsuitable for specifically labeling MCs since we unexpectedly observed very bright TdT expression in a large number of L6 neurons (Fig. S11j) that were electrophysiologically and morphologically different from

bioRxiv preprint doi: https://doi.org/10.1101/456574; this version posted October 30, 2018. The copyright holder for this preprint (which was not certified by peer review) is the author/funder, who has granted bioRxiv a license to display the preprint in perpetuity. It is made available under aCC-BY-NC 4.0 International license.

MCs (Fig. S11l) and negative for Cre expression in SST-Cre mice (Fig. S11m). The GIN line also labels a heterogeneous population of SST cells (including some L4 NMCs; see Supplementary note and Supplementary Table 2). We therefore turned to an alternative GFP line, X98, which also labels MCs and not NMCs[29]. An important caveat of this strategy is that the population of MCs labeled by the X98 line differs from that labeled by the GIN line[29], which makes it difficult to draw a direct link between the circuits described above and X98-based *in vivo* manipulation of MCs. Nevertheless, we reasoned that X98-ChR2 mice would provide a useful comparison to X94-ChR2 experiments, since it would allow us to target a distinct but similarly sized population of non-NMC SST cells using exactly the same protocol used to target X94 cells.

Injecting CRE-DOG/flexed-ChR2-TdT in X98 mice yielded expression which was strikingly complementary to the expression of X94-ChR2, with bright axonal fluorescence in L1, L2/3, and L5, but virtually none in L4 (Fig. 5b). X98 has been described as labeling MCs primarily in deep L5 and upper L6[29], as well as in L2/3. We observed a large number of TdT+ neurons in L2/3 and throughout L5. In X98 mice injected with CRE-DOG/flexed-ChR2-TdT (X98-ChR2 mice), a substantial fraction of TdT+ neurons (81/204; 40%) lacked visible GFP expression, but immunohistochemical staining for somatostatin showed that nearly all TdT+ neurons (192/204; 94%), including GFP- neurons, were somatostatin positive; this discrepancy might arise from some SST cells expressing GFP only transiently during development. Slice recordings revealed that photostimulation of these neurons drove strong inhibition in L2/3 and L5 PCs, but relatively little in L4 and L6 PCs (mean charge transfer ± C.I: L2/3 = 33.9 ± 18.7 pC; L4 = 4.7 ± 3.0 pC; L5 = 17.9 ± 5.0 pC; L6 = 4.9 ± 2.7 pC; Fig. 5d). In contrast to X94-ChR2, in X98-ChR2 slices evoked responses at the

bioRxiv preprint doi: https://doi.org/10.1101/456574; this version posted October 30, 2018. The copyright holder for this preprint (which was not certified by peer review) is the author/funder, who has granted bioRxiv a license to display the preprint in perpetuity. It is made available under aCC-BY-NC 4.0 International license.

population level were only significant in L2/3 and L5 PCs (L2/3: $p < 10^{-11}$, n = 6; L4: p = 0.46, n = 7; L5: $p < 10^{-6}$, n = 15; L6: p = 0.53, n = 4; F-test on linear mixed-effects model). These results, along with the patterns of axonal fluorescence, suggests that ChR2-TdT+ cells in X98-ChR2 mice are a population of SST cells which includes MCs but not NMCs, making X98-ChR2 mice a useful comparison for X94-ChR2 mice. As before, we illuminated the entire slice in these experiments, meaning that MCs in L2/3 were also photostimulated. Since L2/3 MCs inhibit L5 PCs and L5 MCs inhibit L2/3 PCs[12,13,54], the inhibition we observed in L2/3 and L5 PCs likely reflects contributions from both L2/3 MCs and L5 MCs.

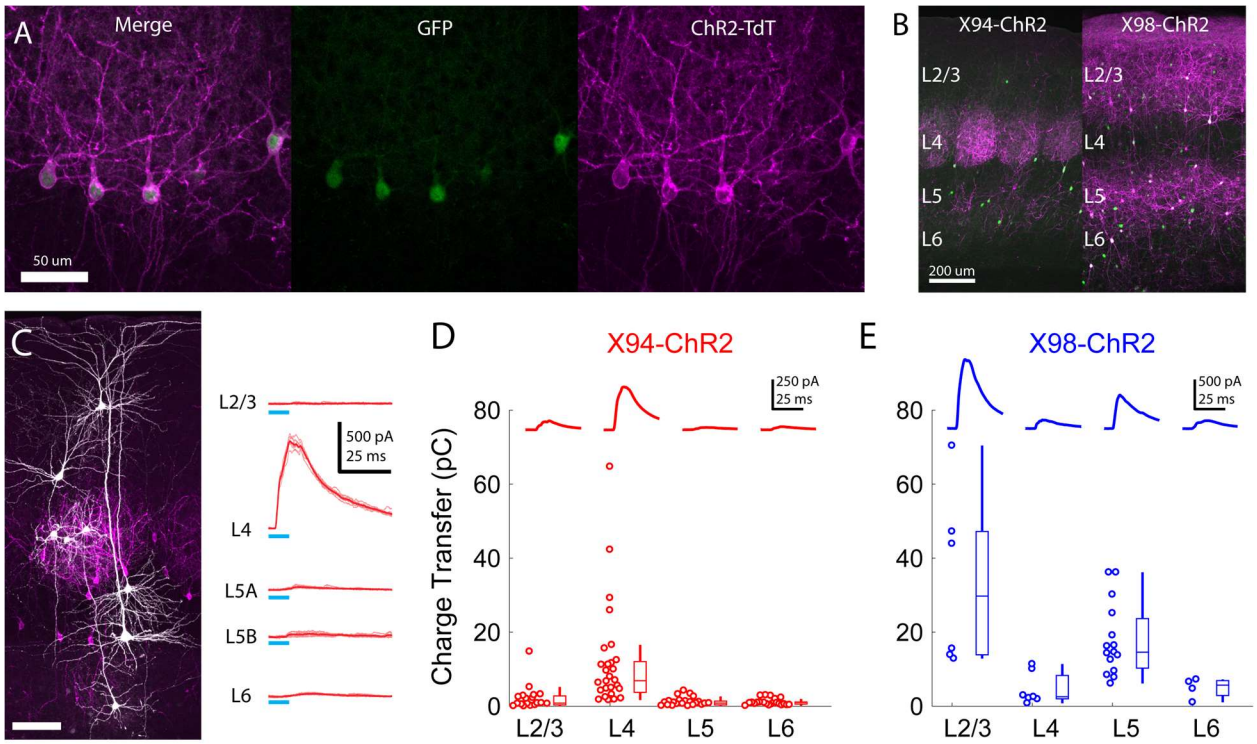

Figure 5. Cre-DOG enables optogenetic control of SST subtypes targeting different cortical layers

(A) Confocal image of cortical section from an X94 mouse injected with Cre-DOG AAVs (AAV2/8. EF1a.C-CreintG WPRE.hGH and AAV2/8. EF1a. N-Cretrcintc WPRE.hGH) along with AAV9.CAGGS.Flex.ChR2-tdTomato.WPRE.SV40. Left: X94- GFP cells (green). Middle: ChR2-TdT expression (magenta). Right: Merged image

bioRxiv preprint doi: https://doi.org/10.1101/456574; this version posted October 30, 2018. The copyright holder for this preprint (which was not certified by peer review) is the author/funder, who has granted bioRxiv a license to display the preprint in perpetuity. It is made available under aCC-BY-NC 4.0 International license.

(B) Side by side comparison of X94-ChR2 mice and X98-ChR2 mice showing laminar differences in localization of ChR2-TdT+ axons

(C) Recording light-evoked IPSCs in X94-ChR2 slices. Left: post-hoc confocal image showing recorded neurons (white) and ChR2-TdT+ NMCs (magenta). Right: example traces of light-evoked IPSCs recorded in neurons in different layers

(D) Median charge transfer of evoked IPSCs in each PC recorded in X94-ChR2 slices, grouped by layer and accompanied by box and whisker plots. Top inset: grand average IPSC

(E) As in D, but for X98-ChR2 mice

SST subtypes drive layer-specific effects during active sensation

To test whether these two different SST subtypes differentially impact sensory processing across the cortical layers, we next optogenetically stimulated X94 and X98 cells while recording barrel cortex activity while animals actively touched a stimulus bar placed in different locations in their whisking field. A simple prediction based on our circuit mapping data is that these two subtypes of SST cells should suppress different cortical layers: NMCs should suppress L4, whereas MCs should suppress L2/3 and L5. However, since SST neurons can also disinhibit PCs by suppressing PV cells, it is possible that the net impact on PCs in different layers could instead be to increase activity. Furthermore, a previous *in vitro* study showed that PV cells are more effectively inhibited by NMCs than by MCs[48]; thus a second hypothesis is that activating NMCs would cause a net disinhibition, whereas MCs would result in a net suppression.

Recording from X94-ChR2 mice, we observed that photostimulating NMCs powerfully suppressed the spontaneous activity of all units in L4, both FS (Fig. S13; 5.2 ± 1.7 Hz control versus 1.1 ± 0.5 Hz light; $p < 10^{-6}$, n = 39 L4 FS units), and RS units (1.8 ± 1.2 Hz control versus 0.9 ± 0.7 Hz light; $p < 0.001$, n = 15 L4 RS units; Fig. 6a,b,e,f; Fig. S12).

bioRxiv preprint doi: https://doi.org/10.1101/456574; this version posted October 30, 2018. The copyright holder for this preprint (which was not certified by peer review) is the author/funder, who has granted bioRxiv a license to display the preprint in perpetuity. It is made available under aCC-BY-NC 4.0 International license.

Similarly, stimulating NMCs strongly attenuated the response to sensory stimulation in L4 units (L4 RS: 3.8 ± 1.7 Hz control versus 2.3 ± 1.2 Hz light; $p < 10^{-6}$, n = 15; L4 FS: 7.1 ± 4.0 Hz control versus 2.9 ± 1.0 Hz light; $p < 10^{-6}$, n = 39; Fig. 6c,d,g,h; Fig. S12). This indicates that, in these conditions, enhancing NMC firing potently suppresses L4 and does not cause a net disinhibition of L4 excitatory neurons. NMC photostimulation caused little to no in the activity of the L5 RS and L6 RS populations (L5 RS spontaneous: 5.1 ± 1.2 Hz control versus 5.1 ± 1.3 Hz light; p = 0.20, n = 59; L6 RS spontaneous: 1.9 ± 1.0 Hz control versus 1.6 ± 0.7 Hz light; p = 0.42, n = 13; L5 RS sensory-driven: 5.9 ± 1.2 Hz control versus 5.6 ± 1.3 Hz light; $p < 10^{-6}$, n = 59; L6 RS sensory-driven: 2.1 ± 1.0 Hz control versus 1.9 ± 0.9 Hz light; p = 0.04, n = 13), although some individual L5 RS units exhibited substantial increases or decreases in their firing rates. This is consistent with the lack of NMC inhibitory connections to PCs in these layers and supports the notion that NMC-mediated inhibition has layer-specific effects on cortical dynamics. Although our *in vitro* data did not reveal a strong monosynaptic connection from NMCs to L2/3 PCS, NMC photostimulation also robustly reduced spontaneous and sensory-evoked activity in the L2/3 RS population (L2/3 RS spontaneous: 0.9 ± 0.5 Hz control versus 0.1 ± 0.1 Hz light; $p < 10^{-4}$, n = 10; L2/3 sensory-driven: 3.4 ± 1.4 Hz control versus 1.5 ± 0.5 Hz light; $p < 10^{-6}$, n = 10), as well as that of nearly all FS units, including those outside of L4 (L2/3 FS sensory-driven: 8.3 ± 4.0 Hz control versus 5.6 ± 3.0 Hz light; $p < 10^{-6}$, n = 11; L5 FS sensory-driven: 7.6 ± 2.8 Hz control versus 4.5 ± 3.0 Hz light; $p < 10^{-6}$, n = 38; L6 FS sensory-driven: 8.3 ± 3.8 Hz control versus 7.0 ± 4.4 Hz light; $p < 10^{-6}$, n = 9; Fig. S13). Because L4 is an important source of excitatory drive to L2/3 PCs and FS cells[55], the most likely explanation is that that NMC

bioRxiv preprint doi: https://doi.org/10.1101/456574; this version posted October 30, 2018. The copyright holder for this preprint (which was not certified by peer review) is the author/funder, who has granted bioRxiv a license to display the preprint in perpetuity. It is made available under aCC-BY-NC 4.0 International license.

photoactivation indirectly reduces activity in L2/3 by dramatically reducing excitatory input from L4.

Photostimulating SST cells in X98-ChR2 mice yielded dramatically different effects. The activity of the L2/3 and L5 RS populations was substantially reduced both during spontaneous conditions (L2/3 RS spontaneous: 0.8 ± 0.6 Hz control versus 0.3 ± 0.2 Hz light; $p < 10^{-6}$, n = 29; L5 RS spontaneous: 5.4 ± 1.5 Hz control versus 4.0 ± 1.8 Hz light; $p < 10^{-6}$, n = 42; Fig. 6a,b,e,f; Fig. S12), and during sensory stimulation (L2/3 RS sensory-driven: 2.4 ± 0.8 Hz control versus 1.2 ± 0.4 Hz light; $p < 10^{-6}$, n = 29; L5 RS sensory-driven: 6.4 ± 1.6 Hz control versus 4.5 ± 1.8 Hz light; $p < 10^{-6}$, n = 42; Fig. 6c,d,g,h ; Fig. S12), whereas the activity of the L4 RS population showed no change or small reductions under the same conditions (L4 RS spontaneous: 1.1 ± 0.4 Hz control versus 1.2 ± 0.5 Hz light; p = 0.82, n = 12; L4 RS sensory-driven: 2.3 ± 0.8 Hz control versus 2.0 ± 0.6 Hz light; p < 0.01, n = 12). We also observed a substantial increase in the firing of L5 RS units following photostimulation (Fig. S12); interestingly, we noted that this rebound effect was also present in L5 RS units recorded in X94-ChR2 mice, though we did not analyze it further here. X98-ChR2 photostimulation did not cause a significant effect in the L6 RS population (L6 RS spontaneous: 4.3 ± 4.7 Hz control versus 3.2 ± 2.5 Hz light; p = 0.13, n = 6; L6 RS sensory-driven: 4.6 ± 5.0 Hz control versus 4.1 ± 4.1 Hz light; p = 0.24, n = 6), though we sampled few L6 units. As with X94-ChR2 mice, we also observed a global suppression of FS units across all layers when photostimulating in X98-ChR2 mice (Fig. S13); however, the magnitude of FS suppression was somewhat smaller in X98-ChR2 mice relative to X94-ChR2 mice (L2/3 FS sensory-driven: 5.2 ± 4.2 Hz control versus 2.4 ± 1.6 Hz light; $p < 10^{-6}$, n = 10; L4 FS sensory-driven: 7.2 ± 1.9 Hz control versus 5.4 ± 1.6 Hz light; $p < 10^{-6}$, n = 47;

bioRxiv preprint doi: https://doi.org/10.1101/456574; this version posted October 30, 2018. The copyright holder for this preprint (which was not certified by peer review) is the author/funder, who has granted bioRxiv a license to display the preprint in perpetuity. It is made available under aCC-BY-NC 4.0 International license.

L5 FS sensory-driven: 7.1 ± 1.9 Hz control versus 5.5 ± 1.9 Hz light; $p < 10^{-6}$, n = 34; L6 FS sensory-driven: 7.8 ± 2.8 Hz control versus 5.6 ± 2.1 Hz light; $p < 10^{-6}$, n = 6).

Taken together, these data suggest that the activation of SST neurons in X98-ChR2 mice exerts a wholly different effect on the cortical microcircuit than that of SST neurons in X94 mice, which labels NMCs. Furthermore, we did not observe any effect on cortical activity when we repeated these experiments in wild-type mice (injected with the same viral cocktail used with X94/X98 mice), indicating that the effects we observed depended specifically on the optogenetic stimulation of GFP+ SST cells (Fig. S12, G-J). Two important caveats should be noted in interpreting these results in the context of our L5 MCs circuit mapping data: 1) photostimulation in these experiments activates X98 cells both in L5 and L2/3, and 2) the cells labeled in X98-ChR2 represent a population that is different from the population labeled by the GIN line, which might be expected to exhibit different connectivity[56]. However, taken together with our X94-ChR2 data, these results demonstrate that SST subtypes are specialized to modulate specific cortical layers and suggest that MCs and NMCs exert very different effects on cortical activity.

bioRxiv preprint doi: https://doi.org/10.1101/456574; this version posted October 30, 2018. The copyright holder for this preprint (which was not certified by peer review) is the author/funder, who has granted bioRxiv a license to display the preprint in perpetuity. It is made available under aCC-BY-NC 4.0 International license.

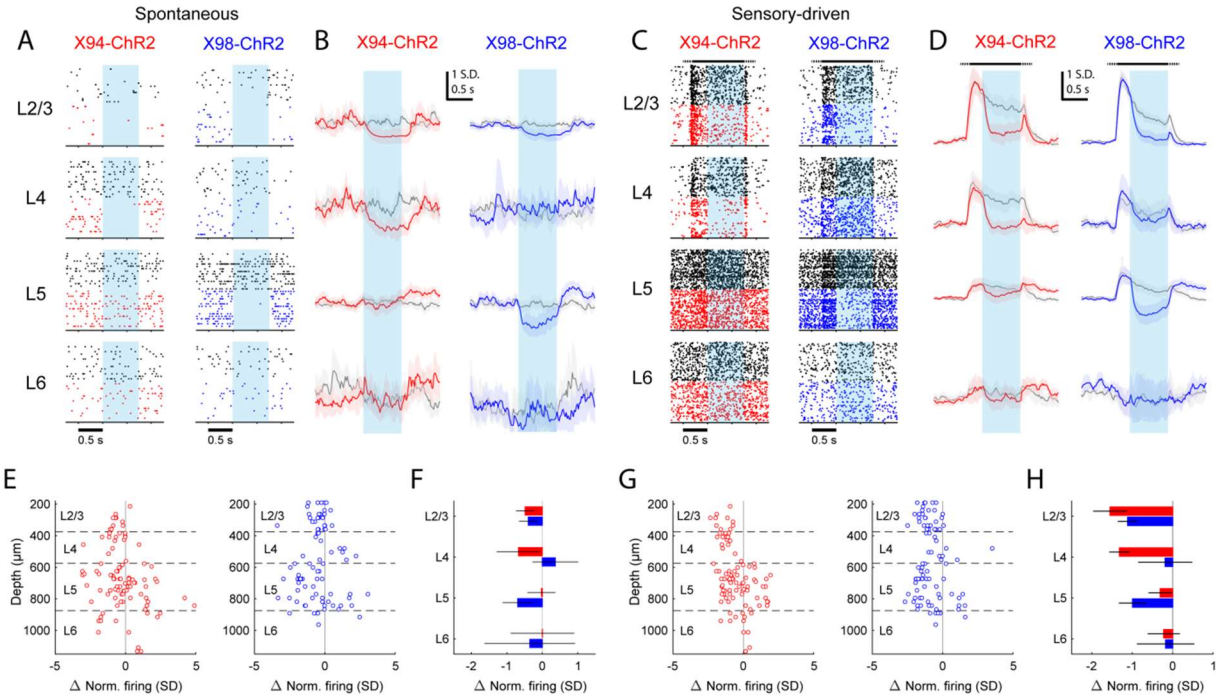

Figure 6. Differential layer-specific modulation of cortical activity by optogenetic activation of NMCs and MCs *in vivo*

(A) Raster plots showing activity in example RS units recorded from different layers in X94-ChR2 and X98-ChR2 mice. Black rasters show trials with no stimulus i.e. spontaneous activity. Colored rasters show trials with photostimulation of X94-ChR2 (red) or X98-ChR2 (blue). Light blue region indicates photostimulation period.

(B) Grand averages of z-scored RS unit activity in L2/3, L4, L5, and L6 showing spontaneous activity (gray) and activity on photostimulation trials (red, X94-ChR2; blue, X98-ChR2). Responses have been smoothed with a 100ms alpha kernel and downsampled to 50 Hz. Shaded regions indicate 95% confidence interval.

(C) As in A, but for sensory-driven activity from trials in which a vertical pole is presented to the whiskers as a tactile stimulus

(D) As in B, but for sensory-driven activity

(E) Change in normalized spontaneous firing of RS units versus depth below pia for X94-ChR2 (left, red) and X98-ChR2 (right, blue) mice

(F) Mean change in normalized firing rate by layer for X94-ChR2 (red bars) and X98-ChR2 (blue bars). Errorbars indicate 95% confidence interval.

(G) As in E, but for change in sensory-driven activity

(H) As in F, but for change in sensory-driven activity

bioRxiv preprint doi: https://doi.org/10.1101/456574; this version posted October 30, 2018. The copyright holder for this preprint (which was not certified by peer review) is the author/funder, who has granted bioRxiv a license to display the preprint in perpetuity. It is made available under aCC-BY-NC 4.0 International license.

Single-cell RNA sequencing maps NMCs onto transcriptomic clusters

Prior studies using transcriptomic approaches have identified multiple clusters within the cortical SST population[24,57]. However, very few molecularly identified SST cell types have been mapped onto physiological/functional phenotypes in the brain[58]. Basing on their striking physiological and circuit differences, we next asked whether NMCs might be transcriptionally distinct. To address this we performed single-cell RNA sequencing on tdTomato$^+$ or GFP$^+$/ tdTomato$^+$ cells isolated by fluorescence activated cell sorting from S1 cortex of SST-Cre; LSL-tdTomato; X94-GFP triple transgenic mice. Clustering tdTomato$^+$ and GFP$^+$/ tdTomato$^+$ cells together based on the 1000 top variable genes yielded 10 distinguishable clusters of SST$^+$ neurons (Figure 7a). These clusters showed remarkable correspondence to clusters similarly generated from single-cell RNA-seq on SST$^+$ neurons from primary visual cortex (V1sp) and anterior lateral motor cortex (ALM) (Figure S14), supporting the idea that SST cell types are conserved across cortical regions[57]. We then asked whether single-cell RNA-seq could distinguish X94-GFP$^+$ cells. Indeed, ~84% (157 out of 188) GFP$^+$/SST$^+$ neurons were distributed among three clusters, with just over half of all GFP cells (102 cells) falling within a single cluster (cluster m10) that could be defined by the specific expression of the gene *Hpse* (Figure 7A). Although cluster m10 contains a small number of cells expressing *Calb1*, they are distinct from X94-GFP$^+$ cells and *Hpse*-expressing cells, consistent with the finding that X94 cells do not co-localize with calbindin immunostaining (Fig. 7a)[29]. Significant numbers of GFP$^+$ cells were also found in clusters m1 (32 cells or 17%) and m12 (23 cells or 12%), however, suggesting that the population of cells labeled in the X94 transgenic mouse line may in fact be somewhat heterogeneous.

bioRxiv preprint doi: https://doi.org/10.1101/456574; this version posted October 30, 2018. The copyright holder for this preprint (which was not certified by peer review) is the author/funder, who has granted bioRxiv a license to display the preprint in perpetuity. It is made available under aCC-BY-NC 4.0 International license.

We next performed triple-label RNA in situ hybridizations using cluster-specific marker genes to validate and characterize the SST cell clusters predicted by single-cell RNA-seq. Tissue sections were prepared from brains of SST-Cre; LSL-tdTomato; X94-GFP triple transgenic mice and hybridized to probes for genes differentially-expressed in selected SST clusters together with probes for GFP and tdTomato to identify SST$^+$ cells. The numbers of marker gene/ GFP/tdTomato triple-positive and GFP/tdTomato double-positive cells were scored from tissue sections from S1 cortex of three mice. The results of this analysis together with a representative image showing Hpse/GFP/tdTomato triple-label RNA in situ hybridization are shown in Figure 7b. The co-localization of *Hpse* expression in ~67% of GFP/tdTomato-positive cells validates the assignment of ~half of X94-GFP cells to cluster m10 based on single-cell RNA-seq. Similarly, few if any GFP-expressing cells co-express *Crh* or *Pld5*, markers for clusters in which X94-GFP cells are largely absent. The inclusion of 16% of GFP$^+$/SST$^+$ cells in cluster m1 is curious, given the expression of *Calb2* – a MC marker – by most cells in this cluster. However, single-cell RNA-seq indicates that X94-GFP cells do not express *Calb2*, a conclusion supported by the paucity of Calb2/GFP/tdTomato triple-positive cells by RNA in situ hybridization (1/58 cells; Figure 7b).

We next analyzed the localization of cells expressing markers for 5 of the 10 major SST cell clusters predicted from single-cell RNA-seq to determine whether molecularly-defined SST neurons correspond to cells with distinct laminar positions in S1 cortex (Figure 7c). Notably, *Hpse* – a marker for the cluster m10, the main X94-GFP-containing cluster – labels SST-cre;tdTomato$^+$ cells found primarily within L4 and L5, similar to the laminar distribution of X94 cells. Crh$^+$/tdTomato$^+$ cells (cluster m9) were found mostly in deep

bioRxiv preprint doi: https://doi.org/10.1101/456574; this version posted October 30, 2018. The copyright holder for this preprint (which was not certified by peer review) is the author/funder, who has granted bioRxiv a license to display the preprint in perpetuity. It is made available under aCC-BY-NC 4.0 International license.

L5/upper L6 and Pld5⁺/tdTomato⁺ cells (cluster m2) in mid-L5; Tacr1⁺/tdTomato⁺ cells (corresponding to cluster m4) were distributed broadly across all laminae. Calb2⁺ cells (cluster m1) colocalizing with tdTomato were found to be broadly distributed among all layers except L4, which instead is largely occupied by *Hpse* neurons. Taken together, these data strongly suggest that *Hpse* defines the L4/L5 NMC cells, and further support the idea that the transcriptomically defined SST neurons described here represent biologically meaningful sub-classes with distinct characteristics based on their anatomy, morphology, connectivity and physiology.

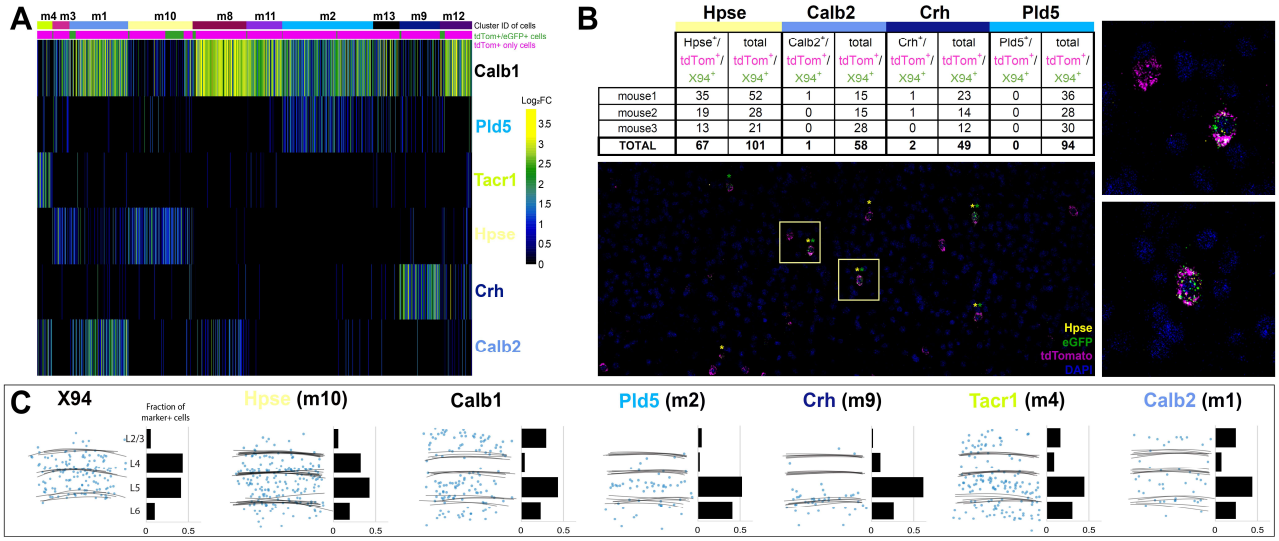

	Hpse		Calb2		Crh		Pld5	
	Hpse⁺/ tdTom⁺/ X94⁺	total tdTom⁺/ X94⁺	Calb2⁺/ tdTom⁺/ X94⁺	total tdTom⁺/ X94⁺	Crh⁺/ tdTom⁺/ X94⁺	total tdTom⁺/ X94⁺	Pld5⁺/ tdTom⁺/ X94⁺	total tdTom⁺/ X94⁺
mouse1	35	52	1	15	1	23	0	36
mouse2	19	28	0	15	1	14	0	28
mouse3	13	21	0	28	0	12	0	30
TOTAL	**67**	**101**	**1**	**58**	**2**	**49**	**0**	**94**

Figure 7. Single cell RNA sequencing of X94 and SST cells

(A) Single-cell RNA-seq was performed on SST-TdTomato⁺ and GFP⁺/tdTomato⁺ cells FACS-purified from primary somatosensory cortex of *X94-eGFP;Sst-cre;LSLtdTomato* mice. Cells were clustered using the Louvain algorithm and organized into vertical columns based on their cluster identity (top bar), with distribution of GFP+/tdTomato+ cells indicated below. Horizontal rows correspond to mRNA expression for highly differentially expressed genes that were selected as cluster classifiers.

(B) Triple-label RNA in situ hybridizations were performed on *X94-eGFP;Sst-cre;LSLtdTomato* mice to validate the predictions made by single-cell RNA-seq. The table shows quantitation of cells co-labeled with probes for selected marker genes, GFP and tdTomato (a proxy for *Sst* expression). Representative image shows overlapping signals from cluster classifier *Hpse*, GFP and tdTomato. Insets show examples of triple-positive cells at higher magnification.

bioRxiv preprint doi: https://doi.org/10.1101/456574; this version posted October 30, 2018. The copyright holder for this preprint (which was not certified by peer review) is the author/funder, who has granted bioRxiv a license to display the preprint in perpetuity. It is made available under aCC-BY-NC 4.0 International license.

(C) Summary of laminar distribution of X94 cells cluster classifier/tdTomato double-positive cells based on tracing and scoring positions of labeled cells across three animals for each condition. Horizontal lines represent estimated positions of laminar boundaries. Left-hand panel shows localization of X94 NMCs using anti-GFP for X94 cells and anti-dsRed for Sst-tdTomato cells. Histograms give normalized frequency values for cluster classifier+/tdT+ cells for each indicated cortical layer.

Discussion

Despite recent strides in understanding cortical inhibitory circuitry, many key features remain unknown. Our data establish the existence of two subnetworks of SST interneurons that make exquisitely selective and reciprocal interactions with different sets of cortical layers. Optogenetic circuit mapping shows that L5 MCs receive excitatory inputs chiefly from PCs in L2/3 and L5, the primary cortical output layers, while L5 NMCs receive inputs mainly from PCs in L4 and upper L6, the primary input zones for afferent input from the ventral posteromedial thalamus[59]. Paired recordings and 2-photon holographic optogenetic interrogation indicate that, in turn, these same SST subtypes selectively inhibit the same PC populations that excite them, at least within L4 and L5. *In vivo*, NMCs and MCs differentially suppress the activity of specific cortical layers. Thus NMCs and MCs are functionally segregated into two distinct networks with selective and complementary laminar connectivity, and functional impacts in the awake brain. Transcriptome profiling further suggests that SST neurons break down into as many as 10 sub-clusters that might compose unique neocortical inhibitory microcircuits. More specifically, our data point to a transcriptionally distinct subset of SST neurons (referred to here at 'NMCs' but marked by the selective expression of the gene *Hpse*) that powerfully controls PC activity in Layer 4, potentially gating bottom up input into the cortex. Conversely, several transcriptionally

bioRxiv preprint doi: https://doi.org/10.1101/456574; this version posted October 30, 2018. The copyright holder for this preprint (which was not certified by peer review) is the author/funder, who has granted bioRxiv a license to display the preprint in perpetuity. It is made available under aCC-BY-NC 4.0 International license.

distinct subsets of SST neurons, commonly referred to as 'MCs', have no direct impact on L4, and instead potently control supragranular and infragranular PCs, the major targets of top down input from other cortical areas.

These results reveal a previously unknown, striking degree of specificity in the inhibitory cortical wiring diagram. In particular, the observation that L5 NMCs exhibit nearly no intralaminar connectivity with L5 PCs, but do engage in dense, reciprocal connectivity with L4 PCs is inconsistent with the idea of a single, global blanket of SST-mediated inhibition. Instead, SST-PC circuits appear to more closely resemble a patchwork quilt, comprised of multiple networks of SST subtypes which independently modulate separate spatial domains. SST-PC connectivity can be extremely dense and non-selective within one of these domains (e.g. creating a blanket within a single laminar microcircuit), but highly selective on the scale of layers and columns.

Functional implications of separate, layer-specific SST feedback circuits

The striking difference in the input and output circuitry of SST subtypes suggested that these two interneuron classes might have different functional effects during sensory processing. Indeed, our Cre-DOG optogenetics experiments demonstrate that MCs nearly exclusively suppress the cortical output layers that they innervate, namely, L2/3 and L5. Conversely, NMCs potently suppress L4, but have a minimal impact on L5 activity. Notably, NMC photo-stimulation did cause a prominent deactivation of L2/3 cells. Since our slice data indicate that NMCs make only weak or infrequent connections onto L2/3 PCs, much of this reduction in L2/3 activity can likely be attributed to a loss of input from L4, which we previously showed is necessary for their sensory response. Nevertheless, a component of

bioRxiv preprint doi: https://doi.org/10.1101/456574; this version posted October 30, 2018. The copyright holder for this preprint (which was not certified by peer review) is the author/funder, who has granted bioRxiv a license to display the preprint in perpetuity. It is made available under aCC-BY-NC 4.0 International license.

this reduction could be due to direct monosynaptic inhibition from NMCs (Fig. 5d). In line with our previous work that employed optogenetic suppression of L4 excitatory neurons directly, we note that FS units in L5 also showed strong and consistent deactivation when L4 was suppressed by NMC photostimulation. However, it is interesting to note that despite this reduction in L5 FS unit activity, we did not observe a net disinhibition across the population of recorded L5 RS units. This apparent discrepancy might be explained by the fact that compared to our previous work, photostimulating NMCs resulted in a much stronger suppression of both L4 and L2/3, likely leading to a profound reduction in L2/3 to L5 excitatory drive. Alternatively, photoactivation of NMCs might cause presynaptic inhibition of glutamatergic release at intracortical/thalamocortical synapses onto L5 PCs[60] or even drive the release of neuropeptides that suppress L5 cells through pre- or post-synaptic mechanisms.

Our circuit mapping experiments revealed both MCs and NMCs exhibit dense, reciprocal connectivity with specific excitatory populations. Thus both SST subtypes participate in potent recurrent inhibitory loops that might be critical for network stabilization, gain control, or competitive interactions between neural ensembles within each layer. Interestingly, NMCs and MCs also receive different sources of long-range input: NMCs but not MCs receive direct thalamic input from VPM, whereas MCs are known to receive long-range inputs from primary motor cortex[61–65]. Taken together, these circuit features suggest that NMCs and MCs might be specialized to regulate different streams of input to the cortical microcircuit. The major 'bottom-up' pathway to the barrel cortex is the lemniscal thalamocortical projection from VPM which carries temporally and spatially precise exteroceptive signals from the whiskers and which primarily targets L4 and acts as

bioRxiv preprint doi: https://doi.org/10.1101/456574; this version posted October 30, 2018. The copyright holder for this preprint (which was not certified by peer review) is the author/funder, who has granted bioRxiv a license to display the preprint in perpetuity. It is made available under aCC-BY-NC 4.0 International license.

a key driver of cortical activity. By virtue of their dense reciprocal connectivity with L4, as well as their direct connections from VPM, NMCs will generate feedback and feedforward inhibition targeted to L4 PCs. This inhibition is likely to occur on slower timescales than PV-mediated inhibition; thus, rather than enforcing temporally precise responses, NMC-mediated inhibition might control amplification of bottom-up sensory signals that is thought to occur in L4. In contrast, MCs will have little effect on the integration of bottom-up signals in L4. However, other important long-range afferents to the barrel cortex, such as those from motor cortices, contralateral S1, and the paralemniscal pathway projection from POm, target the infragranular and supragranular layers (including L1). Inputs from these projections are thought to exert a primarily modulatory effect on barrel cortex activity, and in many cases might carry 'top-down' signals conveying contextual/predictive information[66]. MCs are positioned to directly influence the integration of these signals, and indeed MC-mediated inhibition is capable of gating dendritic integration of these inputs. The parallel structure of MC and NMC networks could allow S1 to independently gate its sensitivity to top-down inputs without changing its sensitivity to bottom-up inputs, and vice versa. In turn, differential modulation of these SST sub-circuits, either by local or long range excitatory input, by VIP-interneuron mediated inhibition[25,67–69] or neuromodulation[25,48,70,71] could represent a mechanism by which the brain dynamically fine-tunes the balance between bottom-up and top-down information during sensory integration.

The stark differences in the inputs to MCs and NMCs suggest that they will likely exhibit different patterns of activity *in vivo*. For technical reasons, most studies of SST activity in awake animals have focused on SST cells in superficial cortical layers, which are

bioRxiv preprint doi: https://doi.org/10.1101/456574; this version posted October 30, 2018. The copyright holder for this preprint (which was not certified by peer review) is the author/funder, who has granted bioRxiv a license to display the preprint in perpetuity. It is made available under aCC-BY-NC 4.0 International license.

mostly MCs. However, some recent studies have observed that subtypes of SST cells with either wide or narrow spike waveforms (which might correspond to MCs and NMCs) are differentially modulated by changes in arousal, behavior, and rewarding stimuli[4,5,25,27]. A pressing question for future investigation will be to determine how local and long-range connectivity contributes to the unique activity patterns of SST subtypes, and conversely, to determine how distinct SST subtypes differentially shape the dynamics of the cortical microcircuit in different sensory and behavioral contexts.

Diversity of SST cells

Our physiological data support the notion of at least two major SST subclasses, defined by their input/output connectivity with L4 or L2/3 and L5. Our single-cell RNA-seq data identified 10 distinct SST subtypes that show good correspondence to 16 SST clusters obtained from single-cell RNA-seq analysis on SST neurons from V1 and ALM cortex[57]. Several of the clusters identified by our analysis split into multiple, smaller clusters in the analysis by Tasic et al.[57], likely due to greater resolution afforded by the greater sequencing depth and/or different parameters used for clustering in this latter study. A unique aspect of our approach is that we additionally included the X94-GFP transgene in our SST cell purification and sequencing, so that we could correlate the transcriptomic data with our physiological analysis of the X94 line. Together with triple-label RNA in situ hybridizations, our sequencing results strongly suggest that L4/L5 NMCs labeled in the X94 mouse line correspond to a transcriptomically distinct class of SST neurons characterized by *Hpse* expression. Our RNA *in situ* hybridization studies further demonstrate that transcriptomically defined SST subtypes show distinct cortical lamination patterns.

bioRxiv preprint doi: https://doi.org/10.1101/456574; this version posted October 30, 2018. The copyright holder for this preprint (which was not certified by peer review) is the author/funder, who has granted bioRxiv a license to display the preprint in perpetuity. It is made available under aCC-BY-NC 4.0 International license.

Previous reports have associated the anatomical location, axonal targeting patterns and physiological properties of a subset of Martinotti cells with expression of calretinin (encoded by the *calbindin2* or *Calb2* gene)[31,58,72,73]. Curiously, from single-cell RNA-seq studies, cluster SST-Etv1_3 in Tasic et al.[57] - which corresponds to cluster m1 identified in this study - has been interpreted to represent this subset of Martinotti cells based largely on *Calb2* expression and enrichment in L2/3 and L5[5]. This poses a conundrum, as we find that 16% of X94-GFP NMC cells cluster with putative *Calb2+* Martinotti cells in cluster m1/SST-Etv1_3 (Figure 7a and Figure S14). It should be noted, however, that triple-label RNA in situ hybridizations confirm that the GFP$^+$ cells are depleted in *Calb2* expression (Figure 7b), suggesting that this cluster is heterogenous, at least with respect to *Calb2* expression. Moreover, *Calb2* expression is enriched in multiple clusters including not just m1 but also m4 and m8 (Figure 7a), precluding the reliance on this gene as a unique molecular marker of cells that are transcriptomically distinct. Future studies will be required to understand the apparent heterogeneity of what have been classically defined as Martinotti cells and whether their molecular identity and distinction from NMCs can be refined by a more granular analysis based on genome-wide transcriptomics.

More generally, an outstanding question for future work is to address how sub-classes of SST neurons identified by single cell transcriptomics differ from one another functionally, potentially due to their local and long-range connectivity and their sensitivity to different neuromodulators. Previous studies on MC-subtypes have outlined at least two distinct sub-classes of MCs[25,31,56], yet the functional roles of these putatively distinct MC subtypes remains essentially unknown. One route to address the functional implications of this high diversity of SST neurons is to use marker genes to generate intersectional driver

bioRxiv preprint doi: https://doi.org/10.1101/456574; this version posted October 30, 2018. The copyright holder for this preprint (which was not certified by peer review) is the author/funder, who has granted bioRxiv a license to display the preprint in perpetuity. It is made available under aCC-BY-NC 4.0 International license.

lines[31,58,72] that target each of the 10 clusters, which would greatly facilitate further physiological and anatomical analysis.

We find that NMCs comprise a large fraction of L5 SST cells and perhaps of SST cells more generally (see Fig. S1g and supplementary text). If NMCs are so prevalent, one might ask why they have been reported on only sparingly. Beyond studies which used the X94 line[29,61,62], close examination of the literature reveals several reports of cells with L4-targeting morphologies and other properties characteristic of NMCs[74–77], which have sometimes been called 'Lorente de Nó cells' in attribution to their earliest describer[78–80]. The previous lack of genetic tools to target these cells may have hindered detailed investigation of L5 NMCs until now; however, L5 NMCs bear striking resemblances to non-Martinotti SST cells in L4 (see Fig. S4 and supplementary text) which are well studied by comparison[46,48,49,81]. It is also likely that NMCs have sometimes been misclassified as fast-spiking cells due to their quasi-fast-spiking intrinsic properties, especially in studies done without genetic or immunohistochemical markers for somatostatin and parvalbumin. This issue likely also applies to studies performing *in vivo* extracellular recordings, since spike waveforms of NMCs are similar to those of parvalbumin-expressing FS cells[4,5,30].

In this study we relied on four transgenic lines for SST neurons (SST-IRES-Cre, X94, X98 and GIN). Although the latter three GFP lines proved useful, heterogeneity within the GFP$^+$ population within these lines (particularly the GIN line)[82,83] and our single-cell RNA-seq data imply that they each are likely to label a mixture of what may be functionally distinct SST subtypes, while other subtypes of SST cells are not covered by these lines at all, such as long-range projecting SST cells that are most prevalent in L6[23,24,29,72]. Importantly,

bioRxiv preprint doi: https://doi.org/10.1101/456574; this version posted October 30, 2018. The copyright holder for this preprint (which was not certified by peer review) is the author/funder, who has granted bioRxiv a license to display the preprint in perpetuity. It is made available under aCC-BY-NC 4.0 International license.

our 2P mapping experiments (using the SST-Cre line) show that cells sampled from the SST population in an unbiased manner connect to L4 or L5 in a mutually exclusive manner; this argues that the distinction between NMCs and MCs is a genuine dichotomy which generalizes to the broader SST population. However, it is certain that these two groups, particularly MCs, can be further subdivided, and examining the connectivity of these finer SST subdivisions will very likely add further nuance to the scheme we describe here. For example, recent work suggests that specific subtypes of MCs are differentially connected to L5 PC subtypes[56,84] and receive different amounts of VIP innervation[25]. Achieving a full understanding of connectivity and functional interactions among SST and PC subtypes will require a more sophisticated understanding of the taxonomy of cortical cell-types, as well as the development of new genetic tools and circuit mapping methods.

Taken together, the data in this study establish two new fundamental inhibitory motifs in the cortex: two subnetworks of SST cells that interconnect with specific cortical compartments – the input and output cortical layers, potentially providing a means to fine tune cortical computation in the barrel cortex during different sensory or behavioral demands. Since most cortical regions appear to contain numerous subtypes of SST cells, we hypothesize that similar architectures will be present in other cortical regions, such as primary visual cortex. Consistent with this notion, other studies have shown that subtypes of SST cells with distinct morphologies, molecular and electrophysiological properties, and connectivity exist in the hippocampus[85–88]. More generally, the approached we employed here to connect the anatomy, physiology, synaptic connectivity and transcriptional profile of specific neuronal subtypes may represent a generalizable strategy to define neuronal subtypes and reveal their unique contributions to brain activity and behavior. With respect

bioRxiv preprint doi: https://doi.org/10.1101/456574; this version posted October 30, 2018. The copyright holder for this preprint (which was not certified by peer review) is the author/funder, who has granted bioRxiv a license to display the preprint in perpetuity. It is made available under aCC-BY-NC 4.0 International license.

to SST neurons' role in sensory computation, our data raise the possibility that sub-networks of dendrite-targeted interneurons fine tune the balance between bottom up and top down input in cortical processing.

Methods

All experiments were performed in accordance with the guidelines and regulations of the Animal Care and Use Committee of the University of California, Berkeley.

Transgenic mice

The following mouse lines were used for this study: the Scnn1-tg3-Cre line (JAX stock # 009613), the Emx1-IRES-Cre line (JAX stock #005628), the PV-IRES-cre line (B6;129P2-Pvalbtm1(cre)Arbr/J ; JAX stock #008069), the SST-IRES-cre line (JAX stock 013044), the GIN line (FVB-Tg(GadGFP)45704Swn/J; JAX stock #003718), the X94-GFP line (Tg(Gad1-EGFP)94Agmo/J; JAX stock 006334), the X98-GFP line (Tg(Gad1/EGFP)98Agmo/J); JAX stock 006340), the Ai9 Rosa-LSL-tdTomato line (JAX stock # 007909). Mice were housed in cohorts of five or fewer with a light:dark cycle of 12:12 hours, and were used for experimentation during their subjective night.

Viral Infection

Neonatal mice (p0-3) were deeply cryo-anesthetized and placed in a head mold. Viral aliquots were loaded into a Drummond Nanoject injector and injected into 4 sites in the barrel cortex of the left hemisphere. At each site, virus was injected at multiple depths (2 depths for scnn1-tg3-cre, 3 depths for emx1-IRES-Cre and SST-IRES-Cre mice and for CRE-

bioRxiv preprint doi: https://doi.org/10.1101/456574; this version posted October 30, 2018. The copyright holder for this preprint (which was not certified by peer review) is the author/funder, who has granted bioRxiv a license to display the preprint in perpetuity. It is made available under aCC-BY-NC 4.0 International license.

DOG injections) in increments of 18.4 nL or 36.8 nL (for SST-IRES-Cre and CRE-DOG injections), for a total of ~150-440 nL of virus injected per mouse. Following injections, mice were moved to an incubation chamber for recovery, and were returned to the dam once they regained color and began to move. Viruses used were AAV9.CAGGS.Flex.ChR2-tdTomato.WPRE.SV40 (acquired from the University of Pennsylvania Vector Core; undiluted for scnn1-tg3-cre, diluted 1:1 with PBS for emx1-IRES-Cre mice), AAV9-2YF-hSyn-DIO-ChrimsonR-mRuby2-Kv2.1, AAV2/8.EF1a.C-CreintG.WPRE.hGH and AAV2/8.EF1a.N-Cretrcintc.WPRE.hGH (acquired from the Massachusetts Ear and Eye Institute). For CRE-DOG experiments, we injected a mixture of 1 part AAV2/8.EF1a.C-CreintG.WPRE.hGH, 1 part and AAV2/8.EF1a.N-Cretrcintc.WPRE.hGH, and 1 part AAV9.CAGGS.Flex.ChR2-tdTomato.WPRE.SV40. In some initial slice experiments, we used a similar cocktail but with 2 parts AAV9.CAGGS.Flex.ChR2-tdTomato.WPRE.SV40.

Brain slice recording

Acute thalamocortical slices were prepared from mice (ages p14-29, at least 14 days after viral injection) as previously described (Adesnik and Scanziani, 2010b). Slices were placed in a recording chamber and constantly perfused with oxygenated artificial cerebro-spinal fluid (NaCl 119 mM, KCl 2.5 mM, $MgSO_4$ 1.3 mM, NaH_2PO_4 1.3 mM, glucose 20 mM, $NaHCO_3$ 26 mM, $CaCl_2$ 2.5 mM) maintained at 32° C (21° C for multiphoton mapping experiments). Slices were oriented with the caudal surface facing up in the recording chamber. To ensure minimal disruption of vertical connectivity, all slices used for recording were inspected under infrared illumination at 40x magnification and/or post-hoc confocal imaging to confirm that pyramidal cell apical dendrites stayed roughly parallel with the surface of the slice or receded slightly deeper as they progressed apically. Whole

bioRxiv preprint doi: https://doi.org/10.1101/456574; this version posted October 30, 2018. The copyright holder for this preprint (which was not certified by peer review) is the author/funder, who has granted bioRxiv a license to display the preprint in perpetuity. It is made available under aCC-BY-NC 4.0 International license.

cell recordings were performed using glass micropipettes (2-5MΩ resistance) pulled on a Sutter P-1000 Micropipette Puller. Pipettes were filled with a Cs^+ based internal ($CsMeSO_4$ 135 mM, NaCl 8 mM, HEPES 10 mM, Na_3GTP 0.3 mM, MgATP 4 mM, EGTA 0.3 mM, QX-314-Cl 5 mM, TEA-Cl 5mM) or a potassium gluconate based internal (K-gluconate 135 mM, NaCl 8 mM, HEPES 10 mM, Na_3GTP 0.3 mM, MgATP 4 mM, EGTA 0.3 mM). In some experiments, biocytin (0.4-1%) was dissolved into the internal solution to enable morphological recovery. Voltage recordings were not corrected for the junction potential. Series resistance was monitored with negative voltage steps during each trial, and was compensated up to 60%. Data were analyzed from recordings in which series resistance remained stable and below 30MΩ. Data were acquired and filtered at 2.2 kHz using a Multiclamp 700B Amplifier (Axon Instruments) and digitized at 20 kHz (National Instruments). All data were acquired using custom written MATLAB (Mathworks) software.

Characterization of intrinsic properties

In all recordings using K-based internal solution, an F-I curve was measured at the start of the experiment using a series of 1-second current injections, at -200 pA, -100 pA, and then proceeding in 50 pA increments from +50 to +500 pA. In some experiments, additional current steps were manually designated and performed online to aid in estimation of rheobase. Resting membrane potential was defined as the median membrane potential during a baseline period measured immediately after break-in. Input resistance was calculated with Ohm's law using the steady state membrane potential during subthreshold current injections steps (current clamp) and/or the steady state current during 5 mV

bioRxiv preprint doi: https://doi.org/10.1101/456574; this version posted October 30, 2018. The copyright holder for this preprint (which was not certified by peer review) is the author/funder, who has granted bioRxiv a license to display the preprint in perpetuity. It is made available under aCC-BY-NC 4.0 International license.

voltage steps (voltage clamp). Action potential onset was detected using code adapted from the Berg lab's *Spike_threshold_*PS function, which defines onset as the point of maximum positive slope in the phase space of the membrane potential and its first derivative [89]. Spike width was measured as the full-width of each spike at the voltage halfway between the action potential threshold and the peak amplitude (half-max). Rheobase was estimated using the average of 1) a linear fit (with coefficients constrained to be nonnegative using the *lsqnonneg* function in MATLAB) of the F-I relation during the last subthreshold current injection step and the first few suprathreshold steps and 2) linear extrapolation of the current necessary to reach threshold based on measurements of the resting membrane potential, input resistance, and average threshold value of the first action potentials evoked during suprathreshold injections. These two measures were usually in good agreement. Adaptation index was calculated (following the Allen Brain Institute's Cell Types Database protocol) for each current injection using the expression:

$$\frac{1}{N-1}\sum_{n=1}^{N-1}\frac{ISI_{n+1}-ISI_n}{ISI_{n+1}+ISI_n}$$

Where N is the number of spikes during that current step and ISI is the interspike interval.

Paired recording connectivity testing

We first targeted whole-cell recordings to a fluorescent (GFP+ or TdTomato+) SST cell, and then subsequently patched nearby neurons in the same slice. In some cases, we recorded serially from several neurons while maintaining the recording of the first neuron, in order to test multiple connections. Monosynaptic excitatory connectivity onto SST cells was

bioRxiv preprint doi: https://doi.org/10.1101/456574; this version posted October 30, 2018. The copyright holder for this preprint (which was not certified by peer review) is the author/funder, who has granted bioRxiv a license to display the preprint in perpetuity. It is made available under aCC-BY-NC 4.0 International license.

tested by driving trains of 10 spikes in the presynaptic cell at 70 Hz via current injection, while monitoring for EPSCs in the postsynaptic cell. Stimulation was repeated at least 15 times in all pairs tested. Monosynaptic inhibitory connectivity from SST cells onto other neurons was tested by driving spikes in the presynaptic cell while monitoring postsynaptically for IPSCs (Cs-based internal, postsynaptic cell held at +10mV) or IPSPs (K-based internal, postsynaptic cell depolarized to approximately -52mV). Electrical connectivity between SST cells was tested by hyperpolarizing each cell with 1-second current injections (at least 15 trials) while monitoring for hyperpolarization in the other cell.

For L5SST-L5PC pairs, we recorded from both pyramidal tract and intratelencephalic type PCs, which could be distinguished by their laminar positions (preferentially L5B versus L5A), morphology visualized via infrared (large soma versus smaller soma) and post-hoc confocal imaging (thick-tufted apical dendrites versus slender-tufted), and/or their intrinsic properties (initial burst/doublet spiking followed by non-adapting spikes versus continuously adapting regular-spiking phenotype; Hattox and Nelson, 2007; Kim et al., 2015; Schubert et al., 2001). We did not observe any significant differences in the connectivity of either L5PC type with L5MCs or NMCs. For L5SST-L4PC pairs, we did not distinguish between spiny stellate and pyramidal/star-pyramidal excitatory cells.

For paired recordings between L5 SST cells and L4 FS/PV cells, we identified FS/PV cells using PV-Cre; LSL-TdTomato mice in some experiments (Fig. S7i). However, it was often difficult to visualize X94 cells using these animals due to the TdTomato fluorescence being much brighter than the GFP fluorescence. In other experiments (Fig. S7h), we targeted

bioRxiv preprint doi: https://doi.org/10.1101/456574; this version posted October 30, 2018. The copyright holder for this preprint (which was not certified by peer review) is the author/funder, who has granted bioRxiv a license to display the preprint in perpetuity. It is made available under aCC-BY-NC 4.0 International license.

FS/PV cells in L4 by looking for L4 neurons with large cell bodies under IR, and then confirmed the identity of these cells electrophysiologically, with the primary criteria separating them from being narrow spike widths (slightly shorter than the average NMC spike) and little or no spike frequency accommodation during high amplitude steps of current injection.

To classify SST-TdT cells as putative NMCs or MCs, we fit a support vector machine (cross validated 10-fold) to perform binary classification of L5 GIN cells and L5 X94 cells using only their intrinsic electrophysiological properties. We found that a classifier based on only two measures (spike width and estimated rheobase) performed just as well as multivariate classification based on a large number of metrics (~85% accuracy).We then used this classifier to predict the identity of a different dataset of L5 SST cells recorded in SST-TdT mice. This approach is likely to have resulted in a small number of SST-TdT cells being misclassified; however, the connectivity of putative NMCs and MCs were highly similar to the connectivity of NMCs and MCs identified using the X94 and GIN lines. Furthermore, our conclusions about the differences in connectivity rates of L5 MCs and NMCs with L4 and L5 PCs are unchanged by the exclusion of the SST-TdT dataset, with the exception of L5PC→L5SST connections – a circuit which has been studied in some detail by others. This approach also effectively assumes a dichotomy in L5 SST cells, since we have only two labels (MC and NMC) to provide as training data, which is an important caveat since it is likely that further subdivisions of SST cells exist in L5 [29]. In a handful of cases, we recorded from SST-TdT cells which appeared to be FS cells [93], with very narrow spikes, low input resistances, and a near complete lack of spike-frequency accommodation during high amplitude current injection steps; these neurons were excluded from further analysis.

bioRxiv preprint doi: https://doi.org/10.1101/456574; this version posted October 30, 2018. The copyright holder for this preprint (which was not certified by peer review) is the author/funder, who has granted bioRxiv a license to display the preprint in perpetuity. It is made available under aCC-BY-NC 4.0 International license.

Using paired recordings, we tested 544 total possible connections between 146 L5 SST cells (39 L5 GIN cells, 53 L5 X94 cells, 54 L5 SST-TdT cells) and PCs/FS cells in L4 and L5. Data from a subset of these neurons (n = 17 L5 GIN cells) were included in a previous study [55]. This dataset was unbalanced, and because in some cases we tested multiple connections onto the same L5 SST cell, included some non-independent observations. Because of this, we used Monte Carlo permutation tests to test for significant differences between the connectivity rates of MCs and NMCs. We generated a permuted dataset with the same observation structure (same number of L5 SST cells and same number of connections tested per L5 SST cell) in place for MCs and NMCs by randomly resampling with replacement at both levels. We then measured the difference in observed connectivity rate for the MC and NMC groups, and repeated this procedure 100,000 times to generate a null distribution of rate differences. We used this distribution to perform a 1-tailed test for significant differences between MC and NMC connectivity rates for each type of connection tested (Table S1).

Optogenetic connectivity mapping *in vitro*

Experiments were done in slices from Emx1-Cre; GIN or Emx1-Cre; X94 mice injected with an AAV driving Cre-dependent expression of ChR2 in all excitatory cells. Whole cell voltage clamp recordings were performed in GFP+ L5 cells to target L5 MCs (Emx1-Cre; GIN) or L5 NMCs (Emx1-Cre; X94). A digital micromirror device was used to focally photo-stimulate excitatory cells in different regions of the slice in order to map the spatial profile of excitatory inputs to recorded MCs and NMCs.

bioRxiv preprint doi: https://doi.org/10.1101/456574; this version posted October 30, 2018. The copyright holder for this preprint (which was not certified by peer review) is the author/funder, who has granted bioRxiv a license to display the preprint in perpetuity. It is made available under aCC-BY-NC 4.0 International license.

Prior to experiments, slices were briefly visually inspected with epifluorescence under a 5x objective to confirm that a wide area containing dense, even expression of fluorescence (tagged to an opsin) was present in the barrel cortex. Recordings were targeted to within this region, which typically covered the entire lateral extent of barrel cortex in 4-5 slices. Slices in which expression appeared faint or uneven were discarded.

In some experiments, it was necessary to locate fluorophore-positive cells in slices also containing an excitatory opsin. To avoid excitotoxicity that can result from excessive illumination of opsin-containing neurons, we limited illumination to very brief intervals (1-2 seconds) while searching for fluorophore-positive cells. In some cases where the target cells were weakly fluorescent (young GIN and X94 animals), we searched for these cells while keeping the slice submerged in sucrose-substituted ACSF. Once target cells were located, this solution was washed out and replaced with normal recording ACSF prior to patching these cells and starting experiments.

DMD-based excitatory input mapping

Laser light was generated using a 1W 445nm diode laser (Ultralasers) and routed via a liquid light guide into a CEL5500 digital micromirror device (DMD) (Digital Light Innovations). The projection from the DMD was then collimated and integrated into the light path of the microscope, before being focused onto the slice chamber using a 5x (Olympus). For experiments using widefield illumination, the DMD passively reflected but not spatially modulate light. Prior to photo-stimulation, infrared and epifluorescence images were captured using an IR-1000 CCD camera (DAGE-MTI) and imported into MATLAB.

bioRxiv preprint doi: https://doi.org/10.1101/456574; this version posted October 30, 2018. The copyright holder for this preprint (which was not certified by peer review) is the author/funder, who has granted bioRxiv a license to display the preprint in perpetuity. It is made available under aCC-BY-NC 4.0 International license.

Excitatory mapping experiments were performed using a modified version of a previously described protocol [55]. Mapping was performed over an area extending from pia to the white matter, covering 2-4 barrel columns laterally (~400 to ~800 μm). For mapping excitatory inputs to GIN and X94 cells, the DMD was used to pattern light into a square region (75 μm x 75 μm). Each stimulation site was spaced 40μm apart from adjacent ones, resulting in some overlap of adjacent stimuli. We chose to 'ramp' our photostimulation, starting each stimulus with the light off and linearly increasing the light intensity over time. Ramping in this manner minimizes activation of fibers of passage [94]. In each trial, a 'sawtooth' light stimulus composed of three successive 25ms ramps of light (1.25 mW/mm^2 final intensity) was applied to one stimulus site (unlike in Pluta et al., 2015, which used only a single ramp per trial). This protocol was chosen in order to maximize the short-term facilitation of excitatory inputs to L5 SST cells, though in practice we found it was usually possible to observe responses during the first ramp alone. Ten regions were stimulated per second in a serial, pseudorandom order, with 4 second breaks after every 10 seconds of mapping. Control experiments were performed using identical stimulation conditions while recording from $ChR2^+$ neurons in all layers. These experiments determined the spatial resolution of photostimulation and confirmed that spiking was elicited in ChR2+ neurons only when regions very close to the soma were stimulated. We also included n = 2 experiments mapping inputs to L5 X94 cells which were performed using the exact mapping protocol described in (Pluta et al., 2015), though our results and conclusions were not substantially altered by their exclusion.

All data were analyzed using custom written MATLAB software. Data preprocessing consisted of removing baseline offsets and slow fluctuations from recordings by

bioRxiv preprint doi: https://doi.org/10.1101/456574; this version posted October 30, 2018. The copyright holder for this preprint (which was not certified by peer review) is the author/funder, who has granted bioRxiv a license to display the preprint in perpetuity. It is made available under aCC-BY-NC 4.0 International license.

subtracting a down-sampled and median-filtered versions. Charge was calculated as the integral of the preprocessed recordings during photo-stimulation and the subsequent 25 milliseconds. To aggregate maps across cells, we first rotated the average map collected in each experiment in order to horizontally orient the laminar boundaries of the mapped area. Maps were next translated vertically to align the L4-L5 laminar boundary, and translated horizontally to align either the home column or the soma position of the recorded cell, before being horizontally cropped to an area ±300μm of their center and then averaged to yield a summary map.

For L4 stimulation experiments, we used widefield photostimulation through a 5x objective. We used two stimulation protocols: prolonged, 1-second ramps of linearly increasing light intensity and trains of ten pulses (1ms duration) at 40 Hz. We stimulated at 4 different intensities for each protocol. Since we sometimes recorded multiple neurons in the same slice (see Fig. S5), we fit generalized linear mixed effects models to the dose-response function of light-intensity versus evoked response (EPSC charge transfer or number of spikes), with fixed effects coefficients for the slope of this function for each cell-type and random effects slope coefficients for each slice and neuron in the dataset as well as a constant intercept term. F-tests were used to test for differences in fixed effects coefficients. For paired analysis of L4 NMCs and L5 MCs/NMCs (Fig. S5), paired t-tests were used to test for differences in L4-evoked responses at maximum stimulus intensity.

Two-photon CGH-based inhibitory output mapping

Laser light was generated using a 5W 1040 nm femtoTrain laser (Sepctra-Physics) and power was modulated on short time scales using a Pockels cell (Conoptics) and a high

bioRxiv preprint doi: https://doi.org/10.1101/456574; this version posted October 30, 2018. The copyright holder for this preprint (which was not certified by peer review) is the author/funder, who has granted bioRxiv a license to display the preprint in perpetuity. It is made available under aCC-BY-NC 4.0 International license.

speed shutter (UniBlitz). Light was delivered to the sample using a VIVO 2- Photon workstation (3i) based on a Sutter Moveable Objective Microscope (Sutter) and the hologram was created using a Phasor 2-Photon computer-generated holography system (3i) with Slidebook software (3i) (Fig. S9a). The holograms used for stimulation were 2D discs of diameter 15 um centered on points with 20 um spacing, making a 400 um x 400 um grid in the focal plane (Fig. S9b,c). Stimulation consisted of 4 or 10 ms square pulses to the Pockels cell with voltages calibrated to produce 200 or 250 mW average power on sample, respectively. The choice of 4 ms at 200 mW or 10 ms at 250 mW stimulation was determined slice to slice based on opsin expression. Power for each hologram was calibrated empirically to account for power loss due to diffraction efficiency degradation away from the zero-order of the SLM. There was an inter-trial interval of 100 ms between the end of one stimulation and the start of the next stimulation. Under these conditions, SST cells spiked reliably and with high radial resolution (Fig. 3c, Fig. S9c,d) and moderate axial resolution (Fig. S9f,g). Given the sparsity of SST neurons (Fig. 3b), this level of spatial resolution provided a good tradeoff between sampling many cells with fewer targets and spiking cells with high spatial resolution. In addition, reliably evoked spikes were produced with low latency and jitter when stimulating randomly through the target grid at 10 Hz. Under these conditions, most evoked spikes occurred in the first 20 ms after the onset of stimulation (Fig. S9e,h).

Space clamp error will inevitably affect somatic measurements of currents from distally located SST→PC synapses; however, we recorded IPSCs using a cesium-based internal solution (which included the ion channel blockers tetraethylammonium and QX-314) and performed experiments at room temperature, which ameliorate this to some extent [95]. We

bioRxiv preprint doi: https://doi.org/10.1101/456574; this version posted October 30, 2018. The copyright holder for this preprint (which was not certified by peer review) is the author/funder, who has granted bioRxiv a license to display the preprint in perpetuity. It is made available under aCC-BY-NC 4.0 International license.

also used a holding potential of +40 mV to increase the IPSC driving force. In these experiments, internal solutions also contained 5 μM Alexa 488 hydrazide (ThermoFisher Scientific) to aid visualization with multiphoton imaging, and ~5 mM kynurenic acid Sodium salt (abcam) was added to the external ACSF to block glutamatergic activity.

To determine which locations evoked responses in the voltage-clamp recordings, first we detected IPSCs using a Bayesian modeling approach via Gibbs sampling [43]. To obtain point estimates IPSC times from the posterior distribution over IPSC times, we binned the IPSC time samples for each trial at 1 ms resolution to create a posterior timeseries of when IPSCs were likely occurring. We then threshholded those timeseries (using *findpeaks* in MATLAB) to compute point estimates of IPSC times. Because the vast majority of evoked spikes recorded from opsin expressing SST cells occurred with short latency (Fig. S9c,f), we estimated the evoked rate at each location from a 30 ms time window starting 5ms after the onset of each stimulation and the background rate of IPSCs for each patched cell from the last 25 ms of all inter-trial intervals. Taking a Poisson distribution with the estimated background rate as the null distribution for all locations for each cell, we could then calculate a p-value for the hypothesis that there are no evoked IPSCs each location (i.e. there is no increase in IPSC rate). We then detected locations with evoked responses using the Benjamini-Hochberg False Detection Rate (FDR) procedure with q = 0.1 [96]. We chose this relatively liberal FDR rate because any false positives will likely be thrown out after the temporal statistics are taken into account.

To determine if a location with evoked rates in both simultaneously patched cells was in fact a common input from a single source, we employed a statistical test that compares a

bioRxiv preprint doi: https://doi.org/10.1101/456574; this version posted October 30, 2018. The copyright holder for this preprint (which was not certified by peer review) is the author/funder, who has granted bioRxiv a license to display the preprint in perpetuity. It is made available under aCC-BY-NC 4.0 International license.

computed synchrony statistic against a null distribution computed from resampled event time series. Specifically, the test we use employs a null distribution where all synchrony is a result of processes at timescales longer than some given duration [45]. The intuition is that the chosen duration should match the general timing of evoked IPSCs such that any synchrony under this null arises only because IPSCs across cells are being generated by two separate presynaptic SST cells stimulated on the same trials. When we reject this null, we have evidence that the synchrony is coming from a process that operates at a finer timescale than the general evoked IPSC statistics: that is, a single presynaptic SST cell is generating highly time-locked IPSCs in two postsynaptic PCs such that the across-trial-within-cell variance of IPSC times is greater than the within-trial-across-cell IPSC times. In our case, the duration of the timescale we want to test against can be estimated from both the timing statistics of evoked spiking of SST cells as wells as the peristimulus time histogram (PSTH) of IPSCs for all trials at all detected input locations across all PC input maps (Fig. S9e,h; Fig. S10g). Using these statistics as guidance, we chose 10 ms as the timescale for our null distribution. In detail, we first summarize the synchrony of events between two simultaneously patched cells at each location where both cells receive input. The statistic we use to quantify synchrony is the sum of the center and two flanking bins of the cross correlation of the binary event time series for simultaneously recorded cells. We then created a null distribution for this statistic at each of these locations using the event series resampling described in [45] which allowed us to estimate a p-value for each location (Fig. S10h,i,j,k). We then detected common spatiotemporal input using these p-values and the Benjamini-Hochberg FDR procedure with q = .05, aggregating all tests across all paired maps. The common input probability for a simultaneously patched pair could then be

bioRxiv preprint doi: https://doi.org/10.1101/456574; this version posted October 30, 2018. The copyright holder for this preprint (which was not certified by peer review) is the author/funder, who has granted bioRxiv a license to display the preprint in perpetuity. It is made available under aCC-BY-NC 4.0 International license.

computed as the total number of detected common input locations for that pair divided by the total number of unique detected input locations for the pair (i.e. the cardinality of the union of the sets of input locations for the two cells).

To align the input maps across cells, we first aligned each input map to a two-photon image of the tissue taken at the time of recording based on previous calibrations between the SLM coordinate frame (e.g. the input map frame) and the two-photon imaging frame. Next, the tissue-aligned maps were then registered via an affine transform to a confocal image of the fixed slice which had been stained with DAPI and in which the opsin expressing cells could be visualized as well as the patched cells which had been filled with biocytin. This allowed each map to be registered to each other based on the laminar borders, in particular the L4-L5 boundary.

Biocytin staining and reconstruction

Following experiments, slices were transferred to 4% paraformaldehyde at 4° for several days. Slices were then repeatedly washed in TBS and subsequently incubated in block solution at room temperature for two hours. Next, 1:1000 streptavidin-Alexa647 conjugate was added to the solution and allowed to stain for 2 hours. Slices were then washed again and mounted/DAPI-stained on coverslips using VectaShield.

Stained neurons were imaged on a confocal microscope, along with the DAPI signal in order to identify laminar boundaries. These images allowed us to qualitatively assess whether recorded cells were L1-targeting MCs or L4-targeting NMCs. We reconstructed a subset of filled neurons, with the goal of performing a bulk quantification of how MC and NMC neurites are distributed with respect to the cortical layers (Fig. 1c, Fig S2e). Since detailed

bioRxiv preprint doi: https://doi.org/10.1101/456574; this version posted October 30, 2018. The copyright holder for this preprint (which was not certified by peer review) is the author/funder, who has granted bioRxiv a license to display the preprint in perpetuity. It is made available under aCC-BY-NC 4.0 International license.

reconstructions of the morphologies of these neurons have already been carried out by others [29,31,36,40,48,61,72,83], we adopted a high-throughput, semi-automated approach to perform 2D reconstruct MCs and NMCs (Fig. S2c). We imaged neurons using a 10x air objective and used the Imaris software package to automatically trace filled neurites. Subsequently, we manually edited these traces and annotated layer boundaries. These reconstructions did not distinguish between axon and dendrite and contained small scale errors (e.g. neurites passing near each other were sometimes spuriously connected). However, comparison of semi-automated reconstructions with detailed 3D reconstructions (performed manually in Imaris, after imaging with a 60x oil immersion objective and/or a 20x air objective) showed that the semi-automated approach yielded an accurate measurement of neurite density in each layer (Fig. S2a,b).

Immunohistochemistry

Animals were perfused with 10mL cold PBS followed by 15mL 4% PFA. Brains were kept in PFA at 4 degrees for 2 hours, then washed 3 times for 15 min each in PBS while rotating. Samples cryopreserved for 24 hours in 30% sucrose in PBS at 4 degrees. 40um sections were taken with a microtome. Each section washed with 0.5mL goat blocking solution for 1 hour at 4 degrees, then overnight at 4 degrees with rat primary antibody for somatostatin in blocking solution (MAB354; Millipore; 1:100). The next day, sections washed 3 times for 15 min in PBS with 0.25% Triton X-100 (PBS-T) at room temperature while gently shaking. Sections washed with 0.5mL in blocking solution containing goat anti-rat Alexa 647 secondary antibody for 1 hour (A21247; Life Technologies Corporation; 1:200). Sections washed 3 times for 15 minutes in PBS-T, then mounted on slides and coverslipped.

bioRxiv preprint doi: https://doi.org/10.1101/456574; this version posted October 30, 2018. The copyright holder for this preprint (which was not certified by peer review) is the author/funder, who has granted bioRxiv a license to display the preprint in perpetuity. It is made available under aCC-BY-NC 4.0 International license.

Preparation for *in vivo* recording

Mice were anesthetized with isoflurane (2.5% vapor concentration). The scalp was removed, the fascia retracted and the skull lightly etched with a 27 gauge needle. Following application of Vetbond to the skull surface, a custom stainless steel headplate was fixed to the skull with dental cement (Metabond). Mice were allowed to recover from surgery for at least 2 d. Then mice were habituated to head-fixation on a free-spinning circular treadmill for 2–10 d. On the day of recording, mice were briefly anesthetized with isoflurane (2%), the skull over V1 was thinned and a small (< 250 μm) craniotomy was opened over S1 with a fine needle.

Tactile stimulus presentation

To stimulate the whiskers, a vertical metal bar (0.5-mm diameter) was rapidly (~50 ms) moved into the whisking field using a stepper motor with submicron precision. The bar was presented at eight different positions, evenly spanning the entire rostral-caudal axis of the whisking field, in a randomly ordered sequence. An additional ninth position that did not contact the whiskers was used to compute non-contact evoked firing rates. The horizontal distance between adjacent stimulus positions was 5.3 mm. Most mice habituated quickly to the presentation of the tactile stimulus assessed by lack of a change in whisking or running speed during stimulus presentation. Mice that did not habituate were excluded from this study. Mice were neither punished nor rewarded for any aspect of their behavior. Most mice ran consistently for hundreds of trials. Of eight stimulus positions, 3–5 contacted the principal whisker. For the X94 experiments eight mice and for the X98 experiments

bioRxiv preprint doi: https://doi.org/10.1101/456574; this version posted October 30, 2018. The copyright holder for this preprint (which was not certified by peer review) is the author/funder, who has granted bioRxiv a license to display the preprint in perpetuity. It is made available under aCC-BY-NC 4.0 International license.

seven mice were used for recordings focused on collecting data from L2/3. Control experiments were performed in three additional mice.

Optogenetic stimulation *in vivo*

For optogenetic stimulation of ChR2 *in vivo*, we used blue light (center wavelength: 455 nm, 25 mW) from the end of a 1-mm fiber-coupled LED (Thorlabs) controlled by digital outputs (NI PCIe-6353). The fiber was placed as close to the craniotomy as possible (< 3 mm). The illumination area was set to illuminate a wide area including all of S1.

Trials lasted 3 seconds and were separated by 1s inter trial intervals. The motor started moving after 1000ms and remained in the whisker field for 1500ms. The LED switched on for 750ms after 1500ms in 50% of the trials. The period of light was chosen to influence the stable steady-state of the response to the whisker stimulus, and all analysis was performed during this time window.

In vivo extracellular multielectrode electrophysiology

A 16- or 32-channel linear electrode with 25-µm spacing (NeuroNexus, A1x16-5mm-25-177-A16 or A1x32-5mm-25-177-A32) was guided into the brain using micromanipulators (Sensapex) and a stereomicroscope (Leica). Electrical activity was amplified and digitized at 30 kHz (Spike Gadgets) and stored on a computer hard drive. The cortical depth of each electrical contact was determined by zeroing the bottom contact to the surface of the brain. Electrodes were inserted ~25° from vertical, nearly perpendicular to the brain′s surface. After some recordings a laminar probe coated with the lipophilic dye DiD was used to mark each electrode track to quantitatively assess its insertion angle and depth with *post hoc*

bioRxiv preprint doi: https://doi.org/10.1101/456574; this version posted October 30, 2018. The copyright holder for this preprint (which was not certified by peer review) is the author/funder, who has granted bioRxiv a license to display the preprint in perpetuity. It is made available under aCC-BY-NC 4.0 International license.

histologic reconstructions. The laminar depth of recorded units was corrected for the insertion angle and the local curvature of the neocortex.

Analysis of *in vivo* data

Spiking activity was extracted by filtering the raw signal between 800 and 7,000 Hz. Spikedetection was performed using the UltraMega Sort package. Detected spike waveforms were sorted using the MClust package (http://redishlab.neuroscience.umn.edu/MClust/MClust.html). Waveforms were first clustered automatically using KlustaKwik and then manually corrected to meet criteria for further analysis. With the exception of eight burst-firing units, included units had no more than 3% of their individual waveforms violating a refractory period of 2 ms. Individual units were classified as either fast-spiking or regular spiking using a k-means cluster analysis of spike waveform components. Since the best separation criterion was the trough-to-peak latency of the large negative-going deflection and clustering is nondeterministic, we defined all units with latencies shorter than 0.36 ms as fast-spiking and all units with latencies larger than 0.38 ms as regular-spiking. Cells with intermediate latencies were excluded from further analysis. Putative ChR2-expressing cells were identified by dramatic increases in spike rates to blue-light stimulation. The depth of each unit was assigned based on the calculated depth of the electrode on the array that exhibited its largest amplitude-sorted waveform. Layer boundaries were determined following a previously established approach[55].

Firing rates were computed from counting spikes in a 750ms window starting 500 ms after onset of the motor movement, which coincided with the onset of the LED during

bioRxiv preprint doi: https://doi.org/10.1101/456574; this version posted October 30, 2018. The copyright holder for this preprint (which was not certified by peer review) is the author/funder, who has granted bioRxiv a license to display the preprint in perpetuity. It is made available under aCC-BY-NC 4.0 International license.

optogenetic suppression trials. Unless otherwise stated, we only analyzed trials when the animal was moving (at least 1cm/s) and not accelerating or decelerating abruptly (not more than 1.5 s.d. deviation from the animal's mean running speed). Average running speed across the population was 41 ± 25 cm/s (n = 20 animals). Two animals were excluded because they ran fewer than 15% of total trials.

Tissue Dissociation and FACS and 10X Chromium

Six triple transgenic SST-TdT-X94 mice (age P97) were euthanized and their brains vibratome sectioned in the same manner used for acute slice experiments (described above), with the exception that slices were cut to 600 µm thickness. The somatosensory cortex was microdissected from the slices using a fine scalpel [55] and allowed to recover in carbogenated 34°C sucrose ACSF for 30 min. Following recovery, tissue was transferred to a solution of 10U/ml Papain (Worthington LK003176), dissolved in HEPES-ACSF (NaCl 120mM, KCl 5mM, MgCl2 2mM, Glucose 25mM, CaCl2 5mM, HEPES 10mM, pH 7.4 and supplemented with 1mMol solution of kynurenic acid sodium salt (Abcam 120256) and previously activated with 2.5 mM Cysteine and 2.5 mM ethylenediaminetetraacetic acid (EDTA) for 20 min at 34°C, and incubated for 25 min at 34°C under carbogen. Digestion was attenuated with 4°C Stop Solution (10% ovomuccoid inhibitor (Worthington LK003182, resuspended in EBSS to manufacturer's specifications) in HEPES-ACSF). In a volume of 3 mL, the tissue was gently triturated through a series of fire polished borosilicate glass pipettes with decreasing aperture diameters of 2mm (50 passes), 1mm (50 passes), and 0.5mm (15 passes). The resulting homogenate was passed through a 40µm cell strainer, layered over 3 mls of 20% Percoll (P4937 Sigma) in Stop Solution, and

bioRxiv preprint doi: https://doi.org/10.1101/456574; this version posted October 30, 2018. The copyright holder for this preprint (which was not certified by peer review) is the author/funder, who has granted bioRxiv a license to display the preprint in perpetuity. It is made available under aCC-BY-NC 4.0 International license.

spun for 5 minutes at 400 RFC at 4°C to remove non-cellular debris. The pellet of cell bodies was resuspended in 0.2 µm-filtered Sorting Solution (HEPES-ACSF, 2% FBS) to approximately 106 cells/ml. Using a BD Influx sorter, we collected GFP+; tdTomato+ and cells into Sorting Solution (GFP+). We then collected a separate population of tdTomato+ irrespective of GFP fluorescence (tdT+) from the same batch of dissociated cells. The sorted cells were pelleted at 400 RCF at 4°C for 5 min, and resuspended in approximately 20µl Sorting Solution. 4 µl of the cell suspension was used to confirm cell concentration and cell quality by visual inspection. Separately, we performed the same procedure on two other batches of triple transgenic SST-TdT-X94 mice (age p45), but in these experiments we performed only the latter sort- collecting SST cells based on tdTomato fluorescence alone.

Single-Cell RNA Sequencing and Analysis

We prepared single cell cDNA libraries from the isolated cells using the Chromium™ Single Cell 3' System according to manufacturer's instructions, with the sole following modification: The quantified cell suspension was directly added to the reverse transcription master mix, along with the appropriate volume of water to achieve the approximate cell capture target. We omitted the 0.04% weight/volume BSA (400 µg/ml) washing step to avoid inevitable cell loss. 2470 tdT+ and 1100 GFP+ cells were applied to individual channels of the Single Cell 3' Chip. The completed libraries were sequenced an Illumina HiSeq4000 to produce paired-end 100nt reads.

The libraries were processed with the 10X Genomics Cell Ranger (v. 2.0.0) pipeline, resulting in the capture of 2611 cells (232 GFP+; tdTomato+ and 2379 tdTomato+

bioRxiv preprint doi: https://doi.org/10.1101/456574; this version posted October 30, 2018. The copyright holder for this preprint (which was not certified by peer review) is the author/funder, who has granted bioRxiv a license to display the preprint in perpetuity. It is made available under aCC-BY-NC 4.0 International license.

irrespective of GFP fluorescence). We then used the scone (v. 1.4.0) R/Bioconductor package [97] to filter out lowly-expressed genes (fewer than 2 UMI's in fewer than 5 cells) and low-quality libraries (using the metric_sample_filter function with arguments hard_nreads = 2000, zcut = 3). This procedure resulted in a final set of 2263 cells and an average of 3,160 genes detected per cell.

Clustering of Single-Cell RNA-seq

We used the zinbwave (v. 1.3.0) Bioconductor package [98] to infer a low-dimensional representation of the data (K=10; epsilon = 1000), adjusting for batch, percentage of ribosomal genes, and total number of expressed features (computed by scater (v. 1.8.0) [99]). Clustering was performed on the ten-dimensional space inferred by zinbwave, using the Louvain algorithm, implemented in the FindClusters function of the Seurat package (Butler et al., 2018; resolution = 2). This procedure resulted in 15 clusters. We then used the clusterExperiment (v. 2.1.1) Bioconductor package [100] to merge those clusters that did not show differential expression (using the function mergeClusters with arguments mergeMethod = "adjP", cutoff = 0.05, and DEMethod = "limma"). This procedure resulted in a final set of 13 clusters. The majority of GFP+ cells fell into three merged clusters, namely m10, m1, and m12. Assignment of cluster identities was done by matching each cluster marker genes to the markers of a set of cells collected from the anterior lateral motor cortex and primary visual cortex by [57]. Given the absence of SST expression, we concluded that three clusters (m5, m6, and m7; total of 163 cells) were contaminants and focused on the remaining 10 clusters (2100 cells) for subsequent analysis. We then used the scmap (v.

bioRxiv preprint doi: https://doi.org/10.1101/456574; this version posted October 30, 2018. The copyright holder for this preprint (which was not certified by peer review) is the author/funder, who has granted bioRxiv a license to display the preprint in perpetuity. It is made available under aCC-BY-NC 4.0 International license.

1.2.0) Bioconductor package [101] to map the clusters onto the 2299 SST neurons identified in VISp and ALM in (Tasic et al., 2017).

Identification of cluster marker genes & *in situ* Hybridization methods

Cluster classifier gene selection: We used the clusterExperiment (v. 2.1.6) Bioconductor package [100] to infer a hierarchy of the clusters and to identify the top differentially expressed genes for each cluster, using the "OneAgainstAll" method of the getBestFeatures function, which creates contrasts to compare each cluster to the average of all the other clusters (Supplementary File 1). For each cluster all genes from the getBestFeatures object with a positive logFC value were examined by heat map; those that best characterized binary behavior across a given cluster definition (high expression within and low/no expression otherwise) were screened for potential quality *in situ* probe (good signal:noise) in the Allen Institute Brain Atlas > ISH DATA.

ISH: Brains from three male P140 day-old mice of the genotype X94-eGFP; SST-Cre > Rosa26 LSL-tdTomato were embedded in Tissue Freezing Media on dry ice. These fresh frozen tissues were subsequently sectioned on a cryostat into 10 um coronal sections containing barrel cortex. Slides were subsequently fixed in paraformaldehyde for 15' after which they were dehydrated, protease IV digested and incubated with commercially available ACDBiotechne probes for the following genes: tdTomato (317041-C1 and C2), Calb2 (313641- C1), Hpse (412251-C1), Tacr1 (428781- C2), Timp3 (471311-C2), Pld5 (custom C2), Crh (316091- C1), Calb1 (428431- C2), and eGFP-o4 (538851-C3) according to ACDBio Fresh Frozen manual assay protocol, followed by DAPI and mounting in Vectashield. Five to seven micron optical sections were imaged at 20x using a Zeiss LSM

bioRxiv preprint doi: https://doi.org/10.1101/456574; this version posted October 30, 2018. The copyright holder for this preprint (which was not certified by peer review) is the author/funder, who has granted bioRxiv a license to display the preprint in perpetuity. It is made available under aCC-BY-NC 4.0 International license.

880 and filters for Alexa 488, Atto 550, Atto 647 and DAPI using Zen software. Z-projections and signal thresholding were performed in FIJI, using the Cell Counter plugin to record marks from manual cell counting calls. Co-expression spatial profiles are presented as a cell frequency table as triple positive as compared to double-positive (Fig. 7B) or rastered on a common anatomy reference to bin normalized counts of cluster classifier+/tdTomato+ (as compared to total tdTomato+) by their laminar position within S1 cortex (Fig. 7C).

Code availability

All the code used for the analysis of the single-cell RNA-seq data is publicly available at https://github.com/drisso/x94.

Supplementary Text

Comparison of L5 X94 cells and L4 non-Martinotti SST cells

Unlike L5 non-Martinotti SST cells, L4 non-Martinotti SST cells (sometimes identified as low-threshold spiking or 'LTS' cells) are well described [29,46,48,49,81,102]. Several lines of evidence suggest that these L4 non-Martinotti SST cells belong to a similar or the same cell-type as the L5 cells labeled by the X94 line. First, many L4 SST cells are labeled by the X94 line. Like L5 X94 cells, these neurons are non-Martinotti cells with axons that target L4 rather than L1. Furthermore, L4 X94 cells have intrinsic properties which are very similar to those of L5 X94 cells (Fig S3 b-e). A recent study reported that the L4 SST cells which are not labeled by X94 display the same phenotype as X94+ L4 SST cells [48], suggesting that all or nearly all L4 SST cells are X94-like, non-Martinotti cells, at least in the mouse barrel cortex.

bioRxiv preprint doi: https://doi.org/10.1101/456574; this version posted October 30, 2018. The copyright holder for this preprint (which was not certified by peer review) is the author/funder, who has granted bioRxiv a license to display the preprint in perpetuity. It is made available under aCC-BY-NC 4.0 International license.

Second, we observed that excitatory synapses from L4 PCs to L5 X94 cells exhibited what appeared to be asynchronous EPSCs during sustained high frequency firing in the presynaptic cell, which continued even after the cessation of presynaptic spiking (Fig. S8c). Asynchronous release of glutamate is uncommon in cortical circuits; to the best of our knowledge, the only other published observation is at the synapse from L4 PCs onto L4 SST cells [46]. Similarly, were also able to observe asynchronous IPSCs in L4PCs during sustained high frequency firing of a connected L5 NMC.

Third, excitatory input mapping to L4 X94 cells revealed that these neurons receive input from the same locations as L5 X94 cells- L4 and the L5B/L6 border (Fig. S3f, h, j). Additionally, during L4 stimulation experiments, L4 X94 cells recorded at the same time as L5 X94 cells had almost identical responses (Fig. S5), indicating similar degrees of L4 input to both L4 and L5 X94s. Furthermore, the connectivity of L5 X94s is broadly similar to the reported connectivity of L4 SST cells, since both are densely interconnected with L4 PCs and L4 FS cells. The connectivity of L5 X94 cells does differ from that of L4 SST cells in some respects. For example, L4FS cells appear to connect to L5 X94 cells less often than has been reported for L4FS→ L4SST connections (Fig. S7a-c). Additionally, whereas L4SST→L4FS synapses are also reported to be more powerful than L4SST→L4PC synapses [48], we found that L5X94→L4PCand L5X94→ L4FS synapses evoked IPSPs/IPSCs of similar amplitudes (Fig. S7d-j), though our sample size was relatively limited.

Finally, our transcriptomic data reveal that X94-GFP cells are concentrated in a cluster defined by the Hpse marker gene. SST cells expressing this gene are found almost exclusively in L4 and L5 and display a similar pattern of lamination to X94-GFP cells.

bioRxiv preprint doi: https://doi.org/10.1101/456574; this version posted October 30, 2018. The copyright holder for this preprint (which was not certified by peer review) is the author/funder, who has granted bioRxiv a license to display the preprint in perpetuity. It is made available under aCC-BY-NC 4.0 International license.

Overall L4 SST cells and L5 X94 cells exhibit strikingly similar electrophysiological, morphological, molecular, and synaptic features, indicating that cells from both groups might be considered 'NMCs'. Working under this assumption, roughly what fraction of SST cells in the barrel cortex are NMCs? The X94 line labels approximately 15% of SST cells in the infragranular layers. This can be considered a lower bound on the fraction of NMCs in L5, since the X94 line may not label all the cells with an NMC phenotype, as is the case in L4. In the subset of L5 SST-TdT cells that we filled with biocytin and could successfully recover the morphology, we found that 19/52 cells (37%) possessed NMC morphologies, 31/52 (60%) possessed MC morphologies, and 2/52 could not be placed in either category. Consistent with this, a support vector machine trained to distinguish L5 GIN cells from L5 X94 cells based on their intrinsic properties (Fig. S1g) labeled 48% of L5 SST-TdT cells as putative NMCs. However, L5 NMCs often appeared to have larger cell bodies than MCs, which could potentially have made L5 NMCs easier to locate or patch and thereby introduce a bias in this assessment. Thus it is likely that between 15-40% of L5 SST cells are NMCs. L4 and L5 respectively host approximately 10% and 40% of all SST cells in S1, so assuming nearly all L4 SST cells are NMCs, we estimate that L4 and L5 NMCs represent 16-26% of all SST cells in S1.

L4 GIN cells

Consistent with the idea that L4 SST cells are nearly all non-Martinotti, we observed that L4 cells labeled by the GIN line also exhibited non-Martinotti morphologies (Fig. S3a). L4 GIN cells had intrinsic properties which were significantly different from those of L5 GIN (MC) cells, but similar to those of L4 X94 cells and L5 X94 (NMC) cells (Fig. S3b-e). Furthermore,

bioRxiv preprint doi: https://doi.org/10.1101/456574; this version posted October 30, 2018. The copyright holder for this preprint (which was not certified by peer review) is the author/funder, who has granted bioRxiv a license to display the preprint in perpetuity. It is made available under aCC-BY-NC 4.0 International license.

the excitatory input maps for L4 GIN cells showed that these neurons received laminar patterns of input very similar to those of L4 and L5 X94 cells, which were dominated by L4 input. The input maps of L4 X94 cells, L5 X94 cells, and L4 GIN cells were all significantly different than the input maps for L5 GIN MCs in terms of the fraction of input originating from L4 and L6 (Fig. S3g, i, j). These results indicate that L4 GIN cells are distinct from L5 GIN MCs. and suggest that L4 GIN cells can also be considered NMCs on the basis of their similarities with X94 cells. Thus, while the GIN line primarily labels MCs in L5, it is more heterogeneous across all the cortical layers, labeling a mixture of MCs and NMCs.

We exploited this fact in order to implement a paired experimental design for our L4 stimulation experiments. The aim of these experiments was to compare the amount of L4 input received by L5 NMCs and L5 MCs, which required us to perform experiments in two sets of animals (SCNN1-Cre; X94 mice and SCNN1-Cre; GIN mice). Whenever possible, while recording from an L5 X94 (NMC) or L5 GIN (MC), we also recorded simultaneously from an L4 X94 or L4 GIN (both NMCs). This configuration acts as a control for possible variability (e.g. in opsin expression, slice health) that is bound to occur to some extent between different slices and animals.

We observed that both L4 GIN cells and L4 X94 cells both received strong input during L4 photostimulation. Furthermore, we observed no significant difference in the responses of these two populations, indicating that we achieved the same degree of L4 activation in both experimental conditions ($p>0.05$ for EPSC charge transfer and spiking, for both types of photostimulation; F-test of linear mixed effects model coefficients). The responses of both

bioRxiv preprint doi: https://doi.org/10.1101/456574; this version posted October 30, 2018. The copyright holder for this preprint (which was not certified by peer review) is the author/funder, who has granted bioRxiv a license to display the preprint in perpetuity. It is made available under aCC-BY-NC 4.0 International license.

L4 GIN and L4 X94 cells were similar to those of L5 X94 cells for all measures, suggesting that L4 provides a similar degree of drive to L4 NMCs and L5 NMCs (Fig. S5a-h).

In contrast, L5 GIN MCs received much less input from L4 than the other groups. In many conditions, we observed essentially no evoked excitation in L5 MCs; because we concurrently observed very strong excitation in L4 NMCs, we can confidently conclude that this result is due to a near absence of L4PC→L5MC connectivity (Fig. S5a-h). When L5 GIN MCs did exhibit L4-evoked EPSCs (typically only during high intensity stimulation, Fig. S5c,d,i,j), their onset occurred at a considerably longer latency than in L5 NMCs (Fig. 5k, 4.6 ms vs 3.6 ms; $p < 0.001$; two-sample t-test, $T(30) = -3.66$) suggesting that they were polysynaptic rather than monosynaptic.

Acknowledgements

We are grateful to Ariel Agmon (West Virginia University) for generously providing X94 mice. We thank Christopher Douglas and Kirill Chesnov for technical assistance. We thank Daniel Mossing, Scott Pluta, and Elena Ryapolova-Webb for help with piloting experiments that did not ultimately make it into this study. We thank Ming-Chi Tsai, Alan Mardinly, Scott Pluta, Evan Lyall, Kelly Clancy, Daniel Mossing, and Ian Oldenburg for helpful comments and discussion. This work was supported by National Institute of Neurological Disorders and Stroke grant DP2NS087725-01 and the New York Stem Cell Foundation. A.N. is supported by the National Institute of Neurological Disorders and Stroke of the National Institutes of Health under Ruth L. Kirschstein National Research Service Award F31NS093925. B.M.S. is supported by a Fannie and John Hertz Foundation Fellowship and an NSF Graduate Research Fellowship. L.P. is supported by IARPA MICRONS contract

bioRxiv preprint doi: https://doi.org/10.1101/456574; this version posted October 30, 2018. The copyright holder for this preprint (which was not certified by peer review) is the author/funder, who has granted bioRxiv a license to display the preprint in perpetuity. It is made available under aCC-BY-NC 4.0 International license.

D16PC00003 and DARPA SIMPLEX contract N66001-15-C-4032. R.K.C., D.S., D.R., J.N. and H.A. were also supported by a grant from the National Institute of Mental Health to J.N. (U19MH114830). H.A. is a New York Stem Cell Foundation Robertson Investigator.

Author contributions

Conceptualization, A.N. and H.A.; Methodology, A.N., B.M.S., D.R., L.P.; Investigation, A.N., B.M.S., J.V., B.S., D.S., R.K.C., and A.Y.E.; Resources, S.S.; Formal Analysis, A.N., B.M.S., and D.R.,; Writing – Original Draft, A.N.; Writing – Review & Editing, A.N., B.M.S., L.P., D.R., J.N., and H.A.; Funding Acquisition, H.A. and J.N.; Supervision, H.A., J.N., and L.P.

bioRxiv preprint doi: https://doi.org/10.1101/456574; this version posted October 30, 2018. The copyright holder for this preprint (which was not certified by peer review) is the author/funder, who has granted bioRxiv a license to display the preprint in perpetuity. It is made available under aCC-BY-NC 4.0 International license.

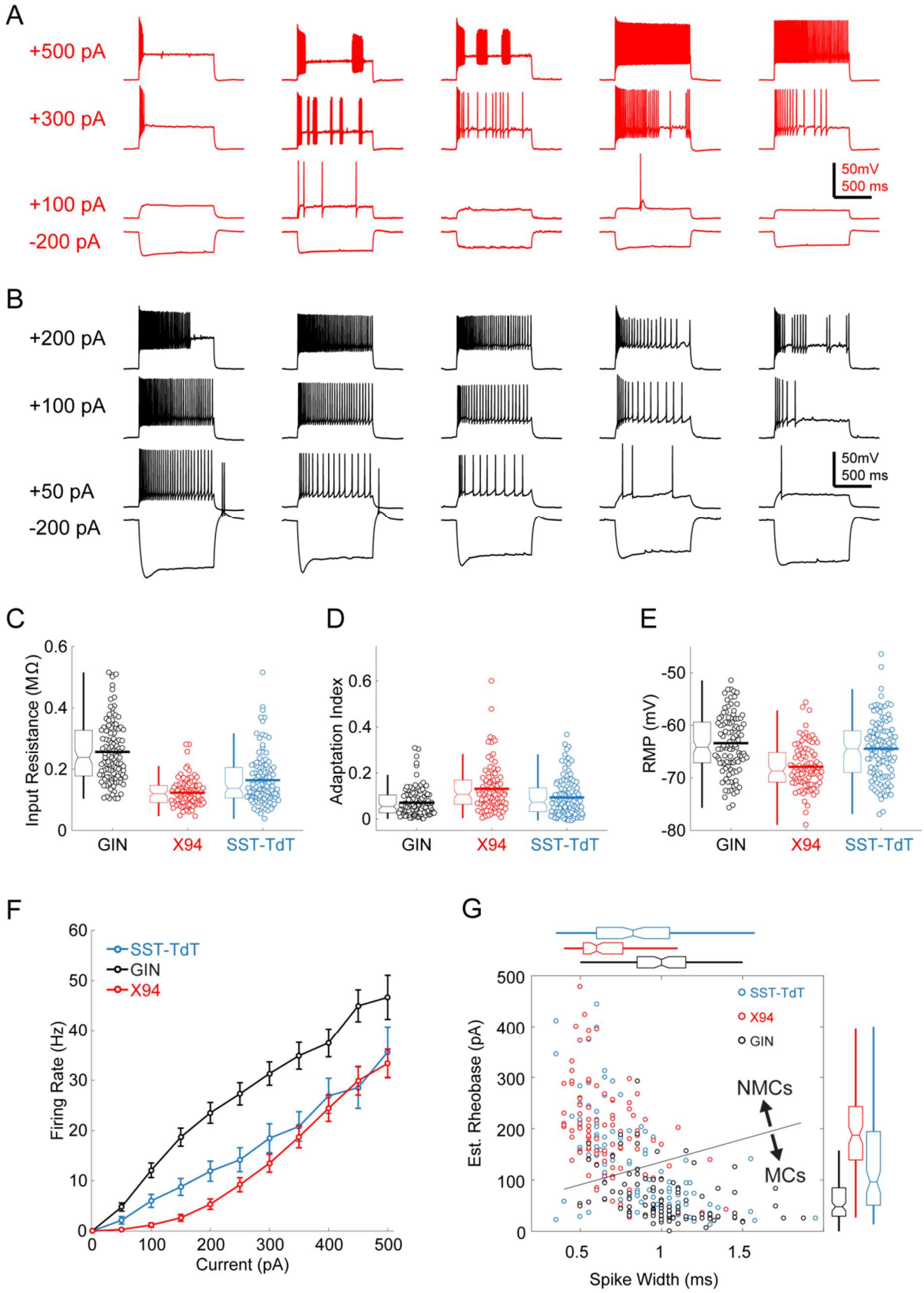

bioRxiv preprint doi: https://doi.org/10.1101/456574; this version posted October 30, 2018. The copyright holder for this preprint (which was not certified by peer review) is the author/funder, who has granted bioRxiv a license to display the preprint in perpetuity. It is made available under aCC-BY-NC 4.0 International license.

Supplementary Figure 1. Intrinsic properties of L5 SST cells; related to Figure 1.

(A) Example traces showing diverse spiking responses of L5 X94 cells during current injection.

(B) As in A, but for L5 GIN cells. Note that less current is being injected due to the greater input resistance of these cells.

(C) Swarm and box-and-whisker plots of input resistance for L5 GIN cells (black), L5 X94 cells (red), and L5 SST-TdT cells (gray). Thick horizontal line indicates distribution mean.

(D,E) As in C, but for spike frequency adaptation index and resting membrane potential.

(F) FI curves from L5 cells recorded in the SST-TdT line (gray), GIN line (black), or X94 line (red).

(G) Scatter plot showing estimated rheobase and median spike width for L5 GIN cells (black), L5 X94 cells (red), and L5 SST-TdT cells (gray). Box and whisker plots summarizing population statistics for these variables are in the margins. The blue line indicates the decision boundary for a linear support vector machine trained to classify L5 GIN cells and L5 X94 cells based on these two variables; this classifier was in turn used to classify SST-TdT cells as putative NMCs or MCs.

bioRxiv preprint doi: https://doi.org/10.1101/456574; this version posted October 30, 2018. The copyright holder for this preprint (which was not certified by peer review) is the author/funder, who has granted bioRxiv a license to display the preprint in perpetuity. It is made available under aCC-BY-NC 4.0 International license.

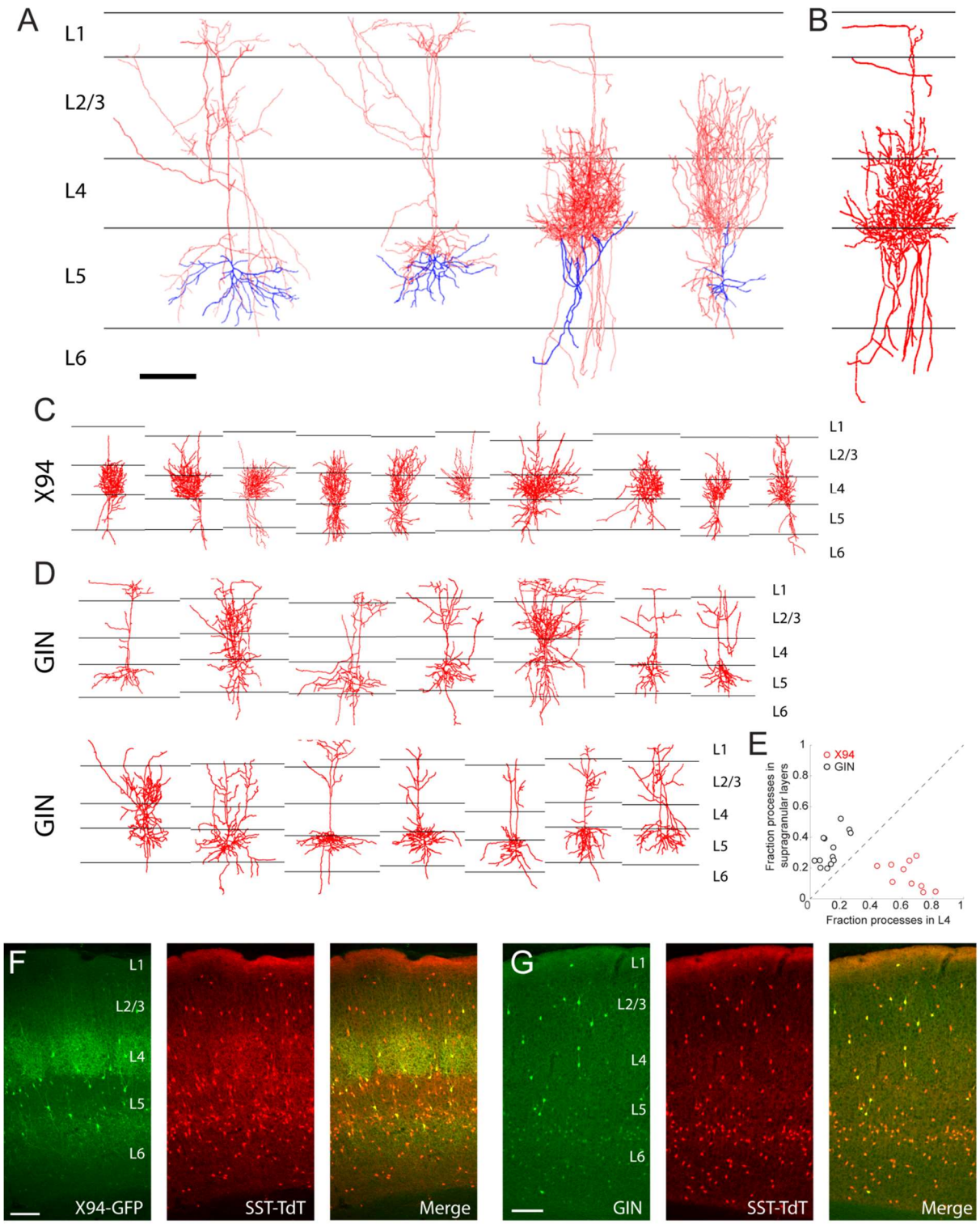

Supplementary Figure 2. Morphological reconstruction of L5 SST cells; related to Figure 1.

bioRxiv preprint doi: https://doi.org/10.1101/456574; this version posted October 30, 2018. The copyright holder for this preprint (which was not certified by peer review) is the author/funder, who has granted bioRxiv a license to display the preprint in perpetuity. It is made available under aCC-BY-NC 4.0 International license.

(A) Examples of biocytin reconstructions done manually at high magnification of two L5 MCs (left two) and two L5 NMCs (right two) showing axonal (red) and dendritic (blue) morphology. Scale bar 150 μm.

(B) An example of a semi-automated reconstruction done at 10x magnification of an L5 NMC (compare to the third reconstruction in A).

(C) Semi-automated reconstructions of L5 X94 cells

(D) As in C, but for L5 GIN cells.

(E) Comparison of neurite density of L5 GIN cells and L5 X94 cells in L4 versus the supragranular layers.

(F) Coronal section of barrel cortex in an X94-GFP; SST-TdT mouse. TdTomato fluorescence can be seen in all layers, with a dense band in L1 from the axons of MCs. Dense axonal arborization of X94-GFP cells is visible in L4, and upper L6 to a lesser extent, but not in L1.

(G) As in F, but for a GIN; SST-TdT mouse.

bioRxiv preprint doi: https://doi.org/10.1101/456574; this version posted October 30, 2018. The copyright holder for this preprint (which was not certified by peer review) is the author/funder, who has granted bioRxiv a license to display the preprint in perpetuity. It is made available under aCC-BY-NC 4.0 International license.

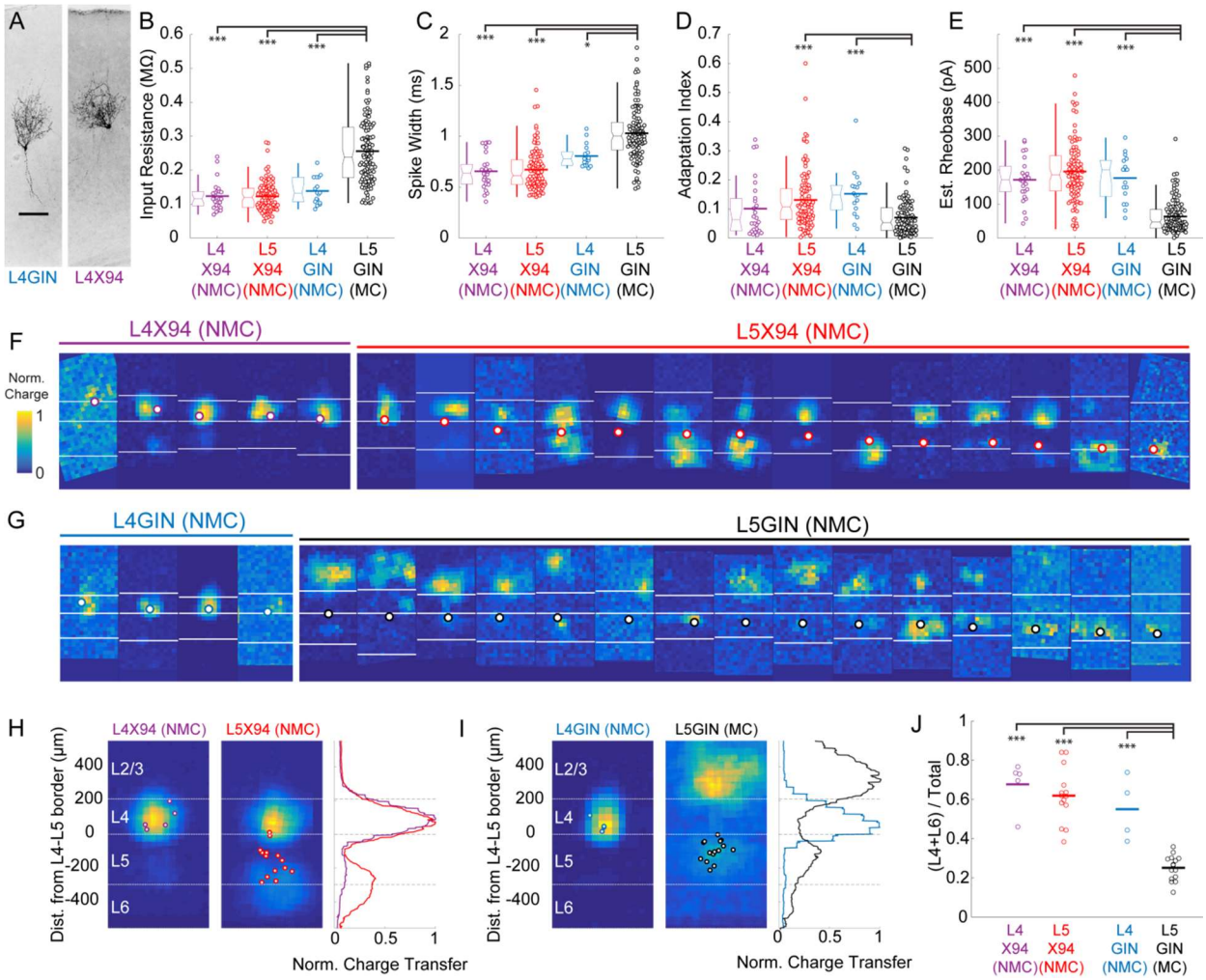

Supplementary Figure 3. Comparison of intrinsic properties and excitatory inputs for L4 and L5 SST cells; related to Figure 1.

(A) Biocytin fills of an L4 GIN cell (left) and an L4 X94 cell (right), both exhibiting non-Martinotti morphology.

(B) Input resistances for L4X94, L5 X94, L4 GIN, and L5 GIN populations. Data are displayed as swarm plots, accompanied by Tukey box plots. The thick horizontal bar within the swarm indicates population mean. The L4 X94, L4 GIN, and L5 X94 populations have significantly lower input resistances than the L5 GIN population (L4 X94, $p = 3.8 \cdot 10^{-9}$; L5 X94, $p = 3.8 \cdot 10^{-9}$; L4 GIN, $p = 3.8 \cdot 10^{-5}$; Wilcoxon rank-sum test versus L5 GIN population).

(C) As in B, but for spike width. The L4 X94, L4 GIN, and L5 X94 populations have significantly shorter spike widths than the L5 GIN population (L4 X94, $p = 4.0 \cdot 10^{-9}$; L5 X94, $p = 3.8 \cdot 10^{-9}$; L4 GIN, $p = 0.029$; Wilcoxon rank-sum test versus L5 GIN population).

bioRxiv preprint doi: https://doi.org/10.1101/456574; this version posted October 30, 2018. The copyright holder for this preprint (which was not certified by peer review) is the author/funder, who has granted bioRxiv a license to display the preprint in perpetuity. It is made available under aCC-BY-NC 4.0 International license.

(D) As in B, but for adaptation index score. The L4 GIN and L5 X94 populations have significantly shorter spike widths than the L5 GIN population (L5 X94, $p = 1.5 \cdot 10^{-6}$; L4 GIN, $p = 1.4 \cdot 10^{-4}$; Wilcoxon rank-sum test) but the L4 X94 was not significantly different.

(E) As in B, but for estimated rheobase. The L4 X94, L4 GIN, and L5 X94 populations have significantly shorter spike widths than the L5 GIN population (L4 X94, $p = 7.2 \cdot 10^{-9}$; L5 X94, $p = 3.8 \cdot 10^{-9}$; L4 GIN, $p = 6.4 \cdot 10^{-7}$; Wilcoxon rank-sum test versus L5 GIN population).

(F) All excitatory input maps for X94 cells in L4 (left, orange) and L5 (right, red). Bordered white dots indicate the location of the recorded soma.

(G). As in F, but for GIN cells in L4 (gray) and L5 (black).

(H) Average maps for L4 and L5 NMCs. Both groups receive strong input from L4. L5 NMCs receive stronger inputs on average from the infragranular layers, though there was no significant difference between these groups nor a significant correlation of the depth of the recorded cell with the relative amount of input received from the deeper layers.

(I) As in H, but for GIN cells. L4 GIN cells (NMCs) receive inputs primarily from L4 (similar to X94 cells) and are very different from L5 GIN cells (MCs).

(J) L5 GIN MCs received a significantly smaller proportion of excitatory charge transfer originating from L4 and L6 than other cell types (L4 X94, $p = 7.2 \cdot 10^{-9}$; L5 X94, $p = 3.8 \cdot 10^{-9}$; L4 GIN, $p = 6.4 \cdot 10^{-7}$; Wilcoxon rank-sum test versus L5 GIN population).

Single asterisk indicates $p<0.05$, three asterisks indicates $p<0.001$.

bioRxiv preprint doi: https://doi.org/10.1101/456574; this version posted October 30, 2018. The copyright holder for this preprint (which was not certified by peer review) is the author/funder, who has granted bioRxiv a license to display the preprint in perpetuity. It is made available under aCC-BY-NC 4.0 International license.

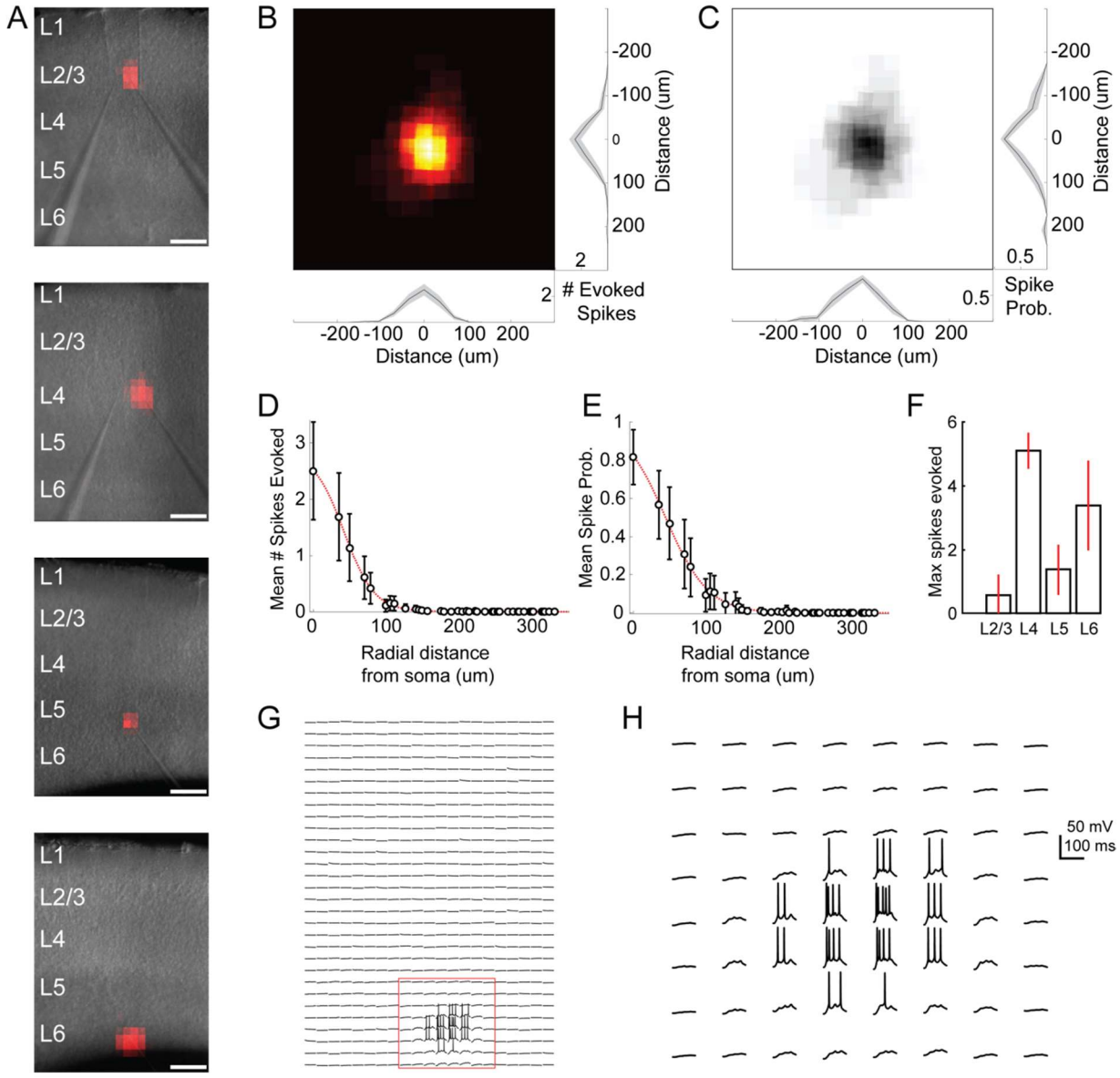

Supplementary Figure 4. Excitation profiles of ChR2+ cells in Emx-Cre DMD-based one photon optogenetic mapping experiments; related to Figure 1.

(A) Example spiking heatmaps recorded from cells in L2-6, overlaid on infrared images of slices. Scale bar indicates 175µm.

(B) Average map of # of evoked spikes per trial in n = 20 ChR2+ cells. Maps are centered on the somata of recorded cells.

(C) As in B, but for probability of evoking at least 1 spike per trial.

(D) Average number of spikes evoked as a function of radial distance from ChR2+ cell soma.

bioRxiv preprint doi: https://doi.org/10.1101/456574; this version posted October 30, 2018. The copyright holder for this preprint (which was not certified by peer review) is the author/funder, who has granted bioRxiv a license to display the preprint in perpetuity. It is made available under aCC-BY-NC 4.0 International license.

(E) As in D, but for probability of evoking at least one spike.

(F) Max number of spikes evoked per trial at the most effective stimulus site (e.g. over the soma) for ChR2+ cells in different layers. Errorbars denote 95% C.I.

(G) Example traces corresponding to the bottom heatmap in A. Spiking is evoked only during perisomatic photostimulation.

(H) Expanded view of red boxed region in F. Bursts of spikes are evoked in a single trial during direct stimulation of the soma.

bioRxiv preprint doi: https://doi.org/10.1101/456574; this version posted October 30, 2018. The copyright holder for this preprint (which was not certified by peer review) is the author/funder, who has granted bioRxiv a license to display the preprint in perpetuity. It is made available under aCC-BY-NC 4.0 International license.

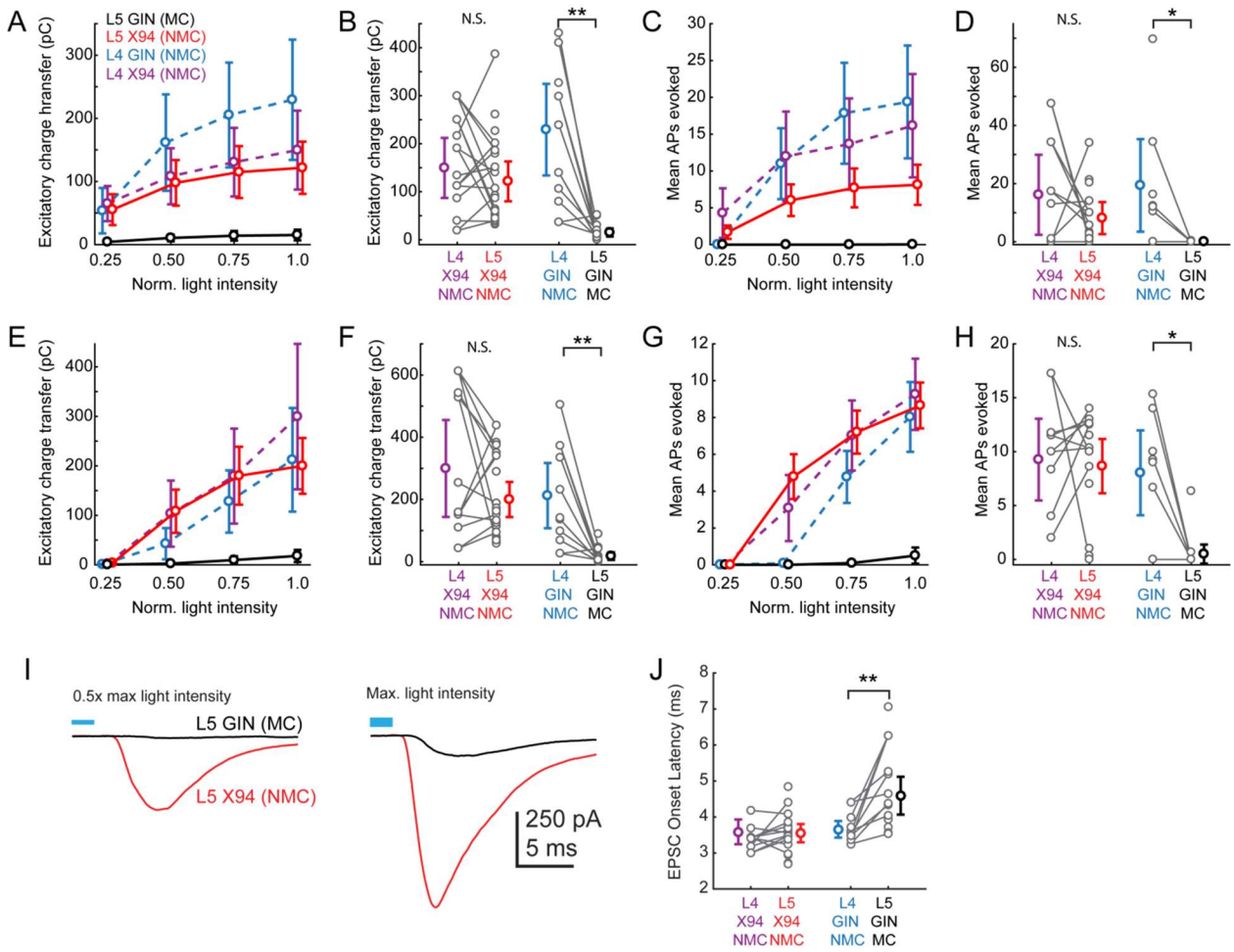

Supplementary Figure 5. Responses of L4 and L5 SST cells to L4 photo-stimulation; related to Figure 2.

(A) Dose response profile of excitatory charge transfer evoked during 1 second ramp stimulation of L4 for X94 cells in L4 (purple) and L5 (red) and for GIN cells in L4 (blue) and L5 (black). To assess differences between groups, we fit a linear mixed-effects model with fixed effects parameters for the slope of the stimulus-response function and random effects slope parameters for each slice and cell recorded, along with a single intercept term. The L5 GIN cell group had a significantly lower fixed effects slope coefficient than the L5 X94 ($p = 2.1 \cdot 10^{-5}$), L4 X94 ($p = 3.1 \cdot 10^{-5}$), and L4 GIN groups ($p = 2.0 \cdot 10^{-9}$).

(B) Mean excitatory charge transfer evoked during maximum intensity 1 second ramp stimulation of L4. Gray lines indicate pairs of cells recorded in the same slice. Charge transfer was not significantly different between L4 X94 cells and L5 X94 cells on a pairwise basis (169.1 ± 91.5 pC versus 118.7 ± 44.0 pC ; p = 0.10, paired t-test), but was significantly different between L4 GIN cells and L5 GIN cells (229.4 ± 95.3 pC versus 15.2 ± 8.4 pC; p = 0.002, paired t-test).

bioRxiv preprint doi: https://doi.org/10.1101/456574; this version posted October 30, 2018. The copyright holder for this preprint (which was not certified by peer review) is the author/funder, who has granted bioRxiv a license to display the preprint in perpetuity. It is made available under aCC-BY-NC 4.0 International license.

(C,D) As in A,B, but for mean number of action potentials evoked in L5 SST cells recorded in current clamp during 1 second ramp photo-stimulation. F-tests on coefficients of a linear mixed-model indicated that the L5 GIN cell group had a significantly lower fixed effects slope coefficient than the L5 X94 ($p = 0.03$), L4 X94 ($p = 1.0 \cdot 10^{-3}$), and L4 GIN groups ($p = 1.7 \cdot 10^{-4}$). The mean number of spikes evoked was not significantly different between L4 X94 cells and L5 X94 cells on a pairwise basis (20.4 ± 23.7 spikes versus 9.0 ± 6.0 spikes ; $p = 0.14$, paired t-test), but was significantly different between L4 GIN cells and L5 GIN cells (19.4 ± 16.0 spikes versus 0.03 ± 0.05 spikes; $p = 0.034$, paired t-test).

(E,F). As in A,B, but for excitatory charge transfer in L5 SST cells recorded in voltage clamp during a train of ten 1ms pulses at 40 Hz. F-tests on coefficients of a linear mixed-model indicated that the L5 GIN cell group had a significantly lower fixed effects slope coefficient than the L5 X94 ($p = 1.2 \cdot 10^{-6}$), L4 X94 ($p = 3.5 \cdot 10^{-9}$), and L4 GIN groups ($p = 5.2 \cdot 10^{-16}$). Charge transfer was not significantly different between L4 X94 cells and L5 X94 cells on a pairwise basis (309.1 ± 220.6 pC versus 191.5 ± 58.8 pC ; $p = 0.055$, paired t-test), but was significantly different between L4 GIN cells and L5 GIN cells (212.2 ± 104.7 pC versus 18.0 ± 12.2 pC; $p = 0.002$, paired t-test).

(G,H). As in A,B, but for mean number of action potentials evoked in L5 SST cells recorded in current clamp during a train of ten 1ms pulses at 40 Hz. F-tests on coefficients of a linear mixed-model indicated that the L5 GIN cell group had a significantly lower fixed effects slope coefficient than the L5 X94 ($p = 1.2 \cdot 10^{-6}$), L4 X94 ($p = 5.3 \cdot 10^{-9}$), and L4 GIN groups ($p = 2.2 \cdot 10^{-14}$). The mean number of spikes evoked was not significantly different between L4 X94 cells and L5 X94 cells on a pairwise basis (9.8 ± 6.2 spikes versus 8.6 ± 2.6 spikes; $p = 0.56$, paired t-test), but was significantly different between L4 GIN cells and L5 GIN cells (8.0 ± 3.9 spikes versus 0.5 ± 0.9 spikes; $p = 0.0068$, paired t-test).

(I) Plots of the grand average EPSC evoked at mild intensity (top; 0.625 $mW \cdot mm^2$) pulse and maximum intensity stimulation (bottom; 1.25 $mW \cdot mm^2$) of L4 for L5 MCs (black) and L5 NMCs (red). Low intensity stimulation produced robust EPSCs in L5 NMCs but not L5 MCs. High intensity stimulation was able to evoke EPSCs L5 MCs but with a delayed onset.

(J) Plot of average EPSC onset latency in response to maximum intensity pulse stimulation of L4 (as seen in bottom panel of I) in different SST cell populations. Gray dots indicate individual cells in each group; cells connected by gray lines indicate neurons recorded in the same preparation (usually simultaneously). EPSC onset latency is uniformly longer for L5 MCs compared to paired L4 NMCs.

Errorbars indicate mean ± 95% confidence interval.

bioRxiv preprint doi: https://doi.org/10.1101/456574; this version posted October 30, 2018. The copyright holder for this preprint (which was not certified by peer review) is the author/funder, who has granted bioRxiv a license to display the preprint in perpetuity. It is made available under aCC-BY-NC 4.0 International license.

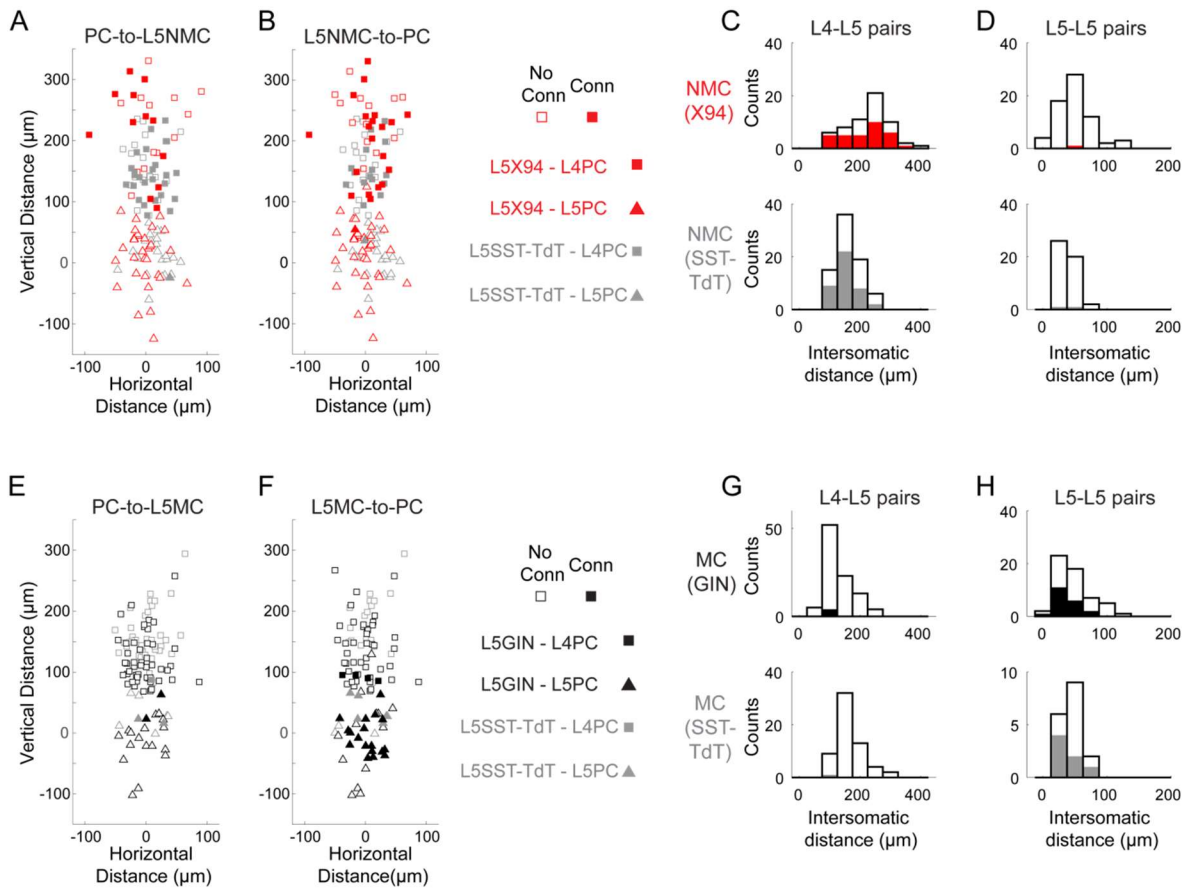

Supplementary Figure 6. Distances of connections tested in paired recordings; related to Figure 4.

(A) Scatterplot showing the relative distances between pairs tested for monosynaptic excitatory connections from L4 and L5 PCs onto L5 NMCs. Squares represent L5 NMC - L4 PC pairs; triangles represent L5 NMC - L5 PC pairs. Filled markers indicate that a connection was observed; open markers indicate no connection was observed. Red symbols indicate pairs tested in X94 mice; gray symbols indicate pairs tested in SST-TdT mice where the L5 NMC was identified electrophysiologically. The origin represents the position of the L5 NMC soma (note that these were located at variable distances from the L4-L5 border).

(B) As in A, but for monosynaptic inhibitory connections from L5 NMCs onto L4 and L5 PCs.

(C) Histogram showing the distribution of intersomatic distances between pairs of L5 NMCs and L4 PCs. Empty bars indicate the number of pairs tested per binned distance; filled bars indicate the number of positive connections (unidirectional in either direction or bidirectional) detected at that bin. Top: pairs in X94 mice. Bottom: pairs in SST-TdT mice.

(D) As in C, but for pairs of L5 NMCs and L5 PCs.

bioRxiv preprint doi: https://doi.org/10.1101/456574; this version posted October 30, 2018. The copyright holder for this preprint (which was not certified by peer review) is the author/funder, who has granted bioRxiv a license to display the preprint in perpetuity. It is made available under aCC-BY-NC 4.0 International license.

(E-H) As in A-D, but for pairs of L5 MCs and L4/L5 PCs. Other than the layer-specific connectivity biases of MCs and NMCs, we did not observe any significant relationship between intersomatic distance (vertical, horizontal, or Euclidean) and connection probability.

bioRxiv preprint doi: https://doi.org/10.1101/456574; this version posted October 30, 2018. The copyright holder for this preprint (which was not certified by peer review) is the author/funder, who has granted bioRxiv a license to display the preprint in perpetuity. It is made available under aCC-BY-NC 4.0 International license.

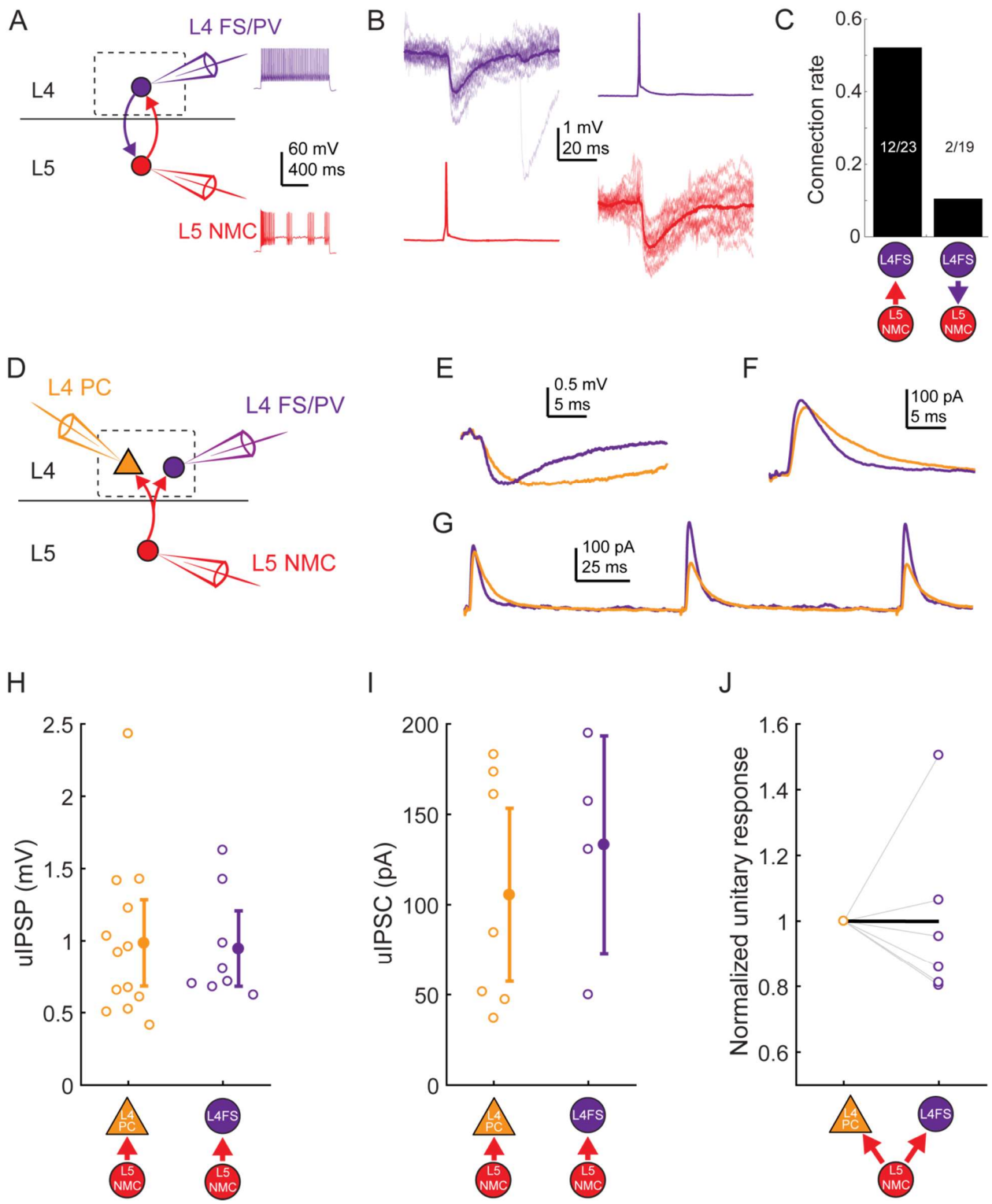

Supplementary Figure 7. L5 NMC connectivity onto L4 FS cells; related to Figure 4.

(A) Schematic of paired recordings between L4 FS/PV cells (purple) and L5 NMCs. Inset: example spiking in response to depolarizing current injection.

bioRxiv preprint doi: https://doi.org/10.1101/456574; this version posted October 30, 2018. The copyright holder for this preprint (which was not certified by peer review) is the author/funder, who has granted bioRxiv a license to display the preprint in perpetuity. It is made available under aCC-BY-NC 4.0 International license.

(B) Monosynaptic IPSPs could be observed in L4 FS cells in response to single spikes in L5 NMCs (left) and vice versa (right)

(C) Bar graph showing connection rates for L5 NMC - L4FS pairs. Connections from L5 NMCs onto L4 FS cells were observed frequently, whereas connections from L4 FS cells onto L5 NMCs occurred rarely.

(D) In some experiments, divergence from L5 NMCs was observed by holding one L5 NMC while serially patching L4 PCs and L4 FS/PV cells.

(E) Example IPSPs in an L4 PC and L4 FS/PV cell evoked by the same L5 NMC.

(F) As in E, but while using a Cs-based internal to record IPSCs (holding potential +10mV) in an L4 PC and an L4 FS/PV cell.

(G) As in F, but while evoking multiple spikes in the L5 NMC at 10 Hz.

(H) Amplitude of unitary IPSPs evoked by L5 NMCs in L4 PCs (0.98 ± 0.30 mV) and L4 FS cells (0.94 ± 0.26 mV). Summary data are represented as mean ± 95% C.I.

(I) Amplitude of unitary IPSCs (recorded using cesium-based internal solution) evoked by L5 NMCs in L4 PCs (105 ± 48 pA) and L4 FS cells (133 ± 60 pA). Summary data are represented as mean ± 95% C.I.

(J) Comparison of unitary response amplitudes (IPSPs or IPSCs) for pairs in which serial recordings were established for an L5 NMC -to- L4 PC connection (left) and an L5 NMC -to- L4 FS/PV connection (right), normalized to the amplitude of the L4 PC response. Thick black line connects the mean normalized L4 PC unitary response (by definition, 1) and mean normalized L4 FS/PV unitary response (0.99 ± 0.52).

bioRxiv preprint doi: https://doi.org/10.1101/456574; this version posted October 30, 2018. The copyright holder for this preprint (which was not certified by peer review) is the author/funder, who has granted bioRxiv a license to display the preprint in perpetuity. It is made available under aCC-BY-NC 4.0 International license.

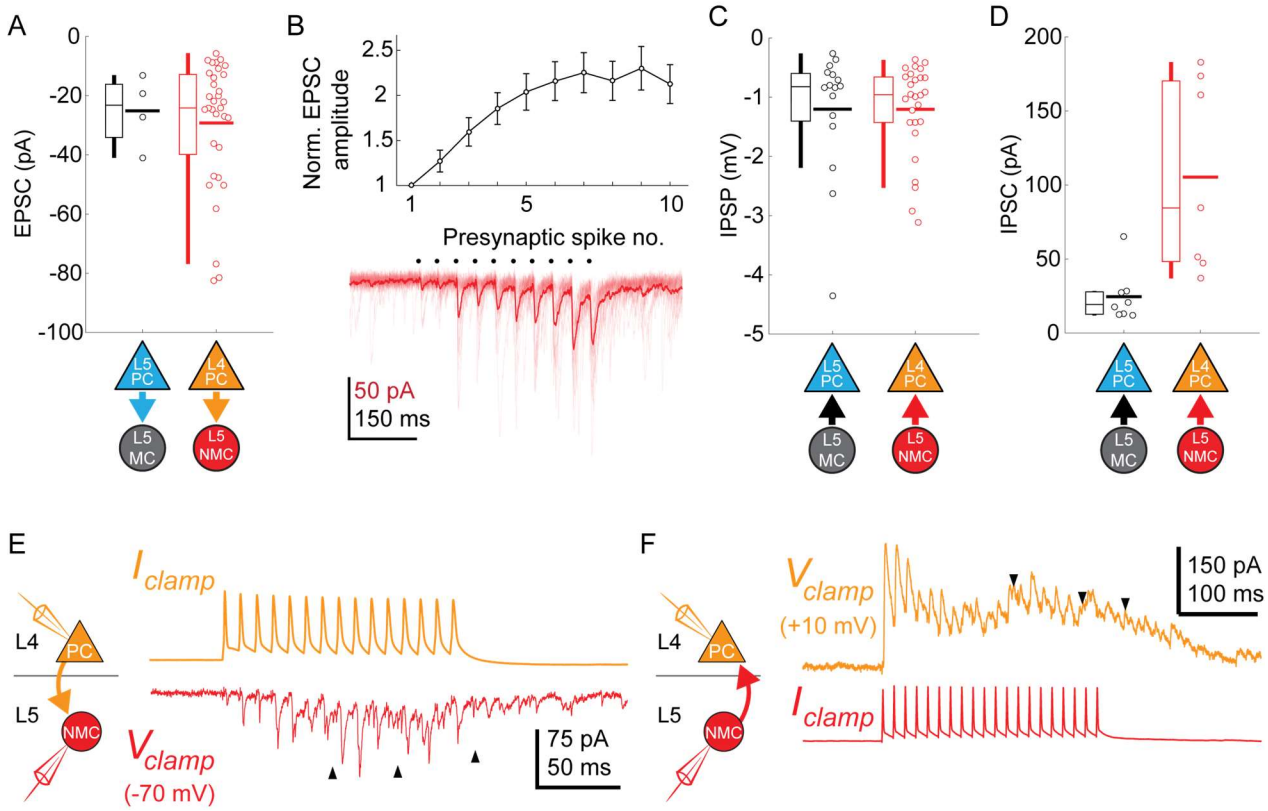

Supplementary Figure 8. Synaptic properties of L5 SST connections; related to Figure 4.

(A) Swarm plots and Tukey box plots of evoked EPSC amplitude in connections onto L5 MCs (black) and L5 NMCs (red), measured as the largest EPSC evoked during a train of presynaptic firing at 70 Hz.

(B) Facilitation dynamics of EPSCs onto L5 NMCs. Bottom: example of facilitating EPSCs in response to a train of 10 spikes at 70 Hz in an L4 PC. Top: Mean EPSC amplitude evoked in L5 NMCs while stimulating L4 PCs at 70 Hz, normalized to EPSC amplitude after the initial spike. Errorbars represent mean ± S.E.M.

(C) Swarm plots and Tukey box plots of evoked IPSP amplitude in connections from L5 MCs (black) and L5 NMCs (red) onto L4/L5 PCs.

(D) As in D, but for IPSCs recorded in L4/L5 PCs (holding potential +10mV) using a Cs-based internal. Unlike IPSPs, IPSCs evoked by L5 NMCs onto L4PCs are stronger than those evoked by L5 MCs onto L5 PCs; this may reflect differences in space clamp error when recording from L4 PCs vs L5 PCs.

(E) Sustained high frequency spiking in L4 PCs appeared to evoke asynchronous EPSCs in L5 NMCs (indicated by black arrows) which continued even after the cessation of spiking.

bioRxiv preprint doi: https://doi.org/10.1101/456574; this version posted October 30, 2018. The copyright holder for this preprint (which was not certified by peer review) is the author/funder, who has granted bioRxiv a license to display the preprint in perpetuity. It is made available under aCC-BY-NC 4.0 International license.

(F) As in C, but for L5 NMC -to-L4PC connections. Sustained high frequency spiking in L5 NMCs appeared to evoke asynchronous IPSCs in L4 PCs (indicated by black arrows) which continued even after the cessation of spiking.

bioRxiv preprint doi: https://doi.org/10.1101/456574; this version posted October 30, 2018. The copyright holder for this preprint (which was not certified by peer review) is the author/funder, who has granted bioRxiv a license to display the preprint in perpetuity. It is made available under aCC-BY-NC 4.0 International license.

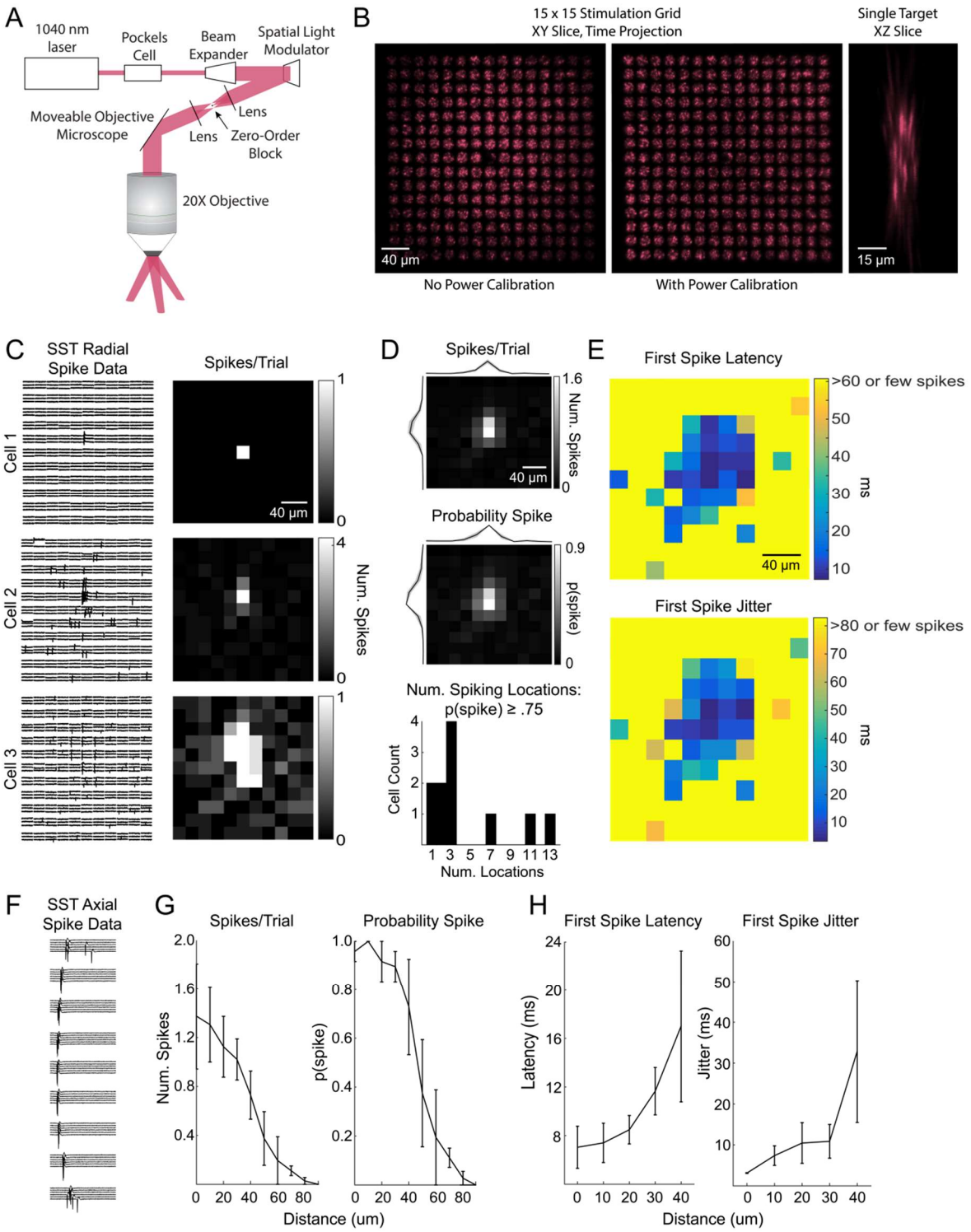

Supplementary Figure 9. Excitation profiles of st-ChrimsonR-expressing SST cells in multiphoton holographic SST-Cre mapping experiments; related to Figure 3.

(A) Schematic of the CGH-based stimulation microscope.

bioRxiv preprint doi: https://doi.org/10.1101/456574; this version posted October 30, 2018. The copyright holder for this preprint (which was not certified by peer review) is the author/funder, who has granted bioRxiv a license to display the preprint in perpetuity. It is made available under aCC-BY-NC 4.0 International license.

(B) Imaging stimulation holograms with two-photon induced fluorescence in a thin fluorescent slide. Left: Time projection of a stimulation sequence covering a 15 x 15 grid of targets at 20 μm spacing before power calibration. Middle: As in Left but with power calibration. Left: XZ slice of a single target. Note that excitation is confined to a small volume and that power calibration results in more uniform excitation radially. The decrease in fluorescence in the middle of the two stimulation grids is due to the zero-order block.

(C) Example plots of the lateral resolution of photo-stimulation. Left column: Raw cell-attached data of light-evoked spiking for example SST cells. Right column: average number of spikes evoked per trial at each location. Locations are 20 μm apart as in mapping experiments.

(D) Radial spike count statistics. Top: Average map of the number of evoked spikes per trial in st-ChrimsonR+ cells (n= 11). Maps are centered on the somata of recorded cells. Middle: As in top, but for probability of evoking at least 1 spike per trial. Bottom: Histogram of number of locations per cell which evoked a spike at least 75% of the trials.

(E) Radial spike timing statistics. Top: Average first spike latency for st-ChrimsonR+ cells (n = 11). Yellow indicates that the average was > 60 ms or that too few spikes were observed across cells at those locations to obtain a good estimate. Bottom: Average first spike jitter, computed as the full-width half-maximum of the first spike times. Yellow indicates a jitter of greater than 80 msec or that too few spikes were observed across cells at those locations.

(F) Data from an example cell as the hologram is moved axially. Distance between locations is 10 μm.

(G) Axial spike count statistics. Left: Average number of evoked spikes as a function of axial distance for st-ChrimsonR+ cells (n=4). Right: As in left, but for the probability of at least one spike per trial.

(H) Axial spike timing statistics. Left: Average first spike latency as a function of axial distance (n=4 cells). Right: First spike jitter as a function of axial distance for st-ChrimsonR+ cells (n = 3).

bioRxiv preprint doi: https://doi.org/10.1101/456574; this version posted October 30, 2018. The copyright holder for this preprint (which was not certified by peer review) is the author/funder, who has granted bioRxiv a license to display the preprint in perpetuity. It is made available under aCC-BY-NC 4.0 International license.

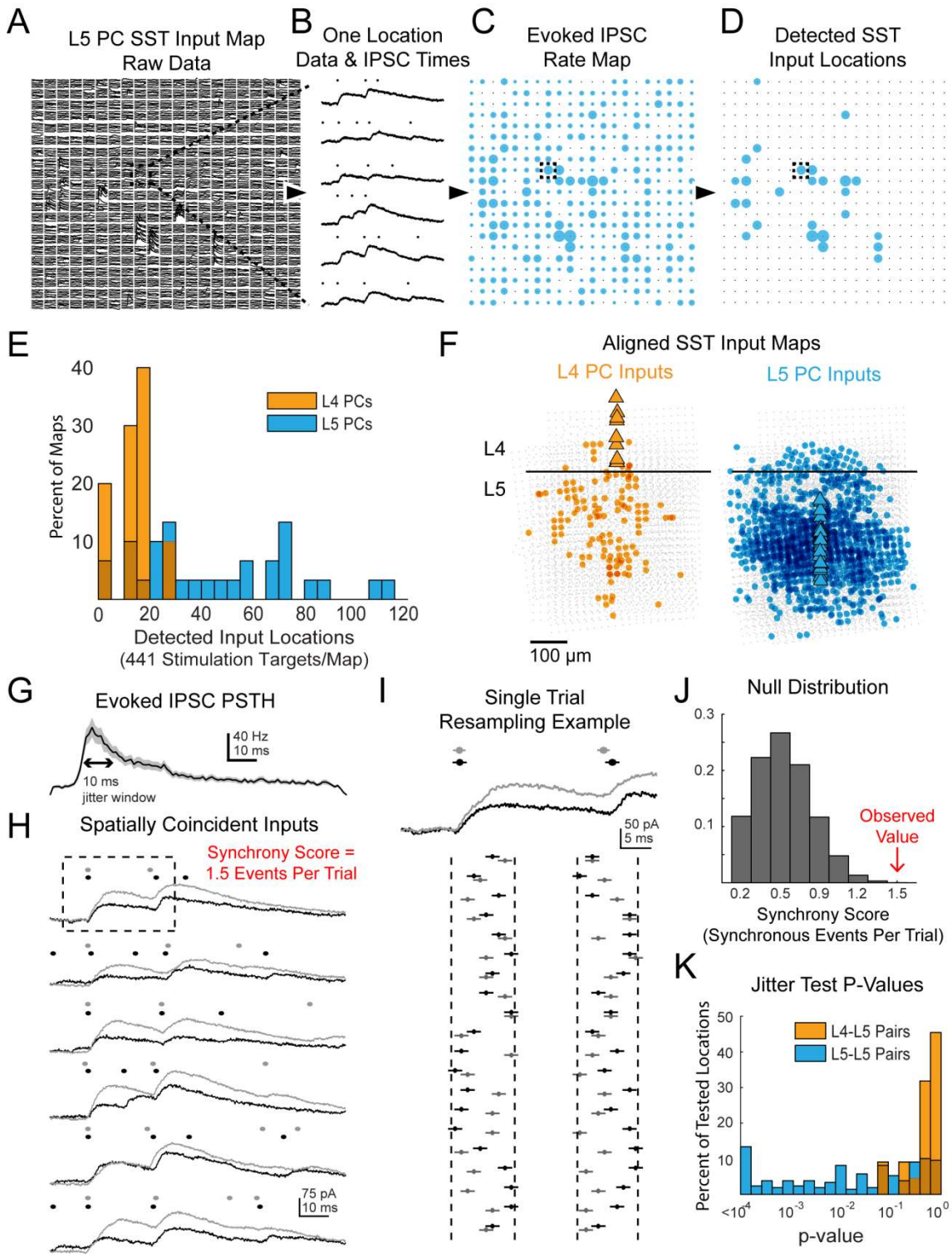

bioRxiv preprint doi: https://doi.org/10.1101/456574; this version posted October 30, 2018. The copyright holder for this preprint (which was not certified by peer review) is the author/funder, who has granted bioRxiv a license to display the preprint in perpetuity. It is made available under aCC-BY-NC 4.0 International license.

Supplementary Figure 10. Data processing and additional results for multiphoton SST output mapping; related to Figure 3.

(A) Example of raw data a single map onto a L5 PC. Dashed box shows location for which data is shown in B.

(B) Example of Bayesian PSC detection on all 6 trials from a single location from the map in A.

(C) A map showing the evoked IPSC rates at each location for the map from A. Dashed box shows location of data from B.

(D) As in C except only locations which pass FDR detection are shown.

(E) Histograms showing the number of locations with evoked IPSCs in each map recorded for both L4 and L5 PCs.

(F) Overall spatial input distributions for SST cells in L5 to both L4 PCs (left, n = 10) and L5 PCs (right, n = 28). Maps are aligned vertically to the L4-L5 border and horizontally to the PC soma. For this representation all inputs are plotted with the same size circle.

(G). PSTH of IPSC times aggregated from all locations with detected evoked IPSC rates. A 10 ms duration which matches the jitter duration for temporal synchrony is marked for comparison.

(H) As in B except showing data and IPSC detection for two simultaneously recorded L5 PCs. The synchrony score for this location is 1.5 events/trial. Dashed box shows data used for I.

(I) Example of 20 resamplings of the events during the analysis window for the first trial shown in H. Vertical dashed lines show discrete event jittering windows. Horizontal lines on each event span 2ms such that if the lines from two events overlap then they would be counted as synchronous.

(J) Null distribution of synchrony score from event time series resampling of the data in H. The observed value is from the far right extreme of the distribution.

(K) Histograms of p-values for all spatially overlapping locations for all pairs from jitter synchrony tests.

bioRxiv preprint doi: https://doi.org/10.1101/456574; this version posted October 30, 2018. The copyright holder for this preprint (which was not certified by peer review) is the author/funder, who has granted bioRxiv a license to display the preprint in perpetuity. It is made available under aCC-BY-NC 4.0 International license.

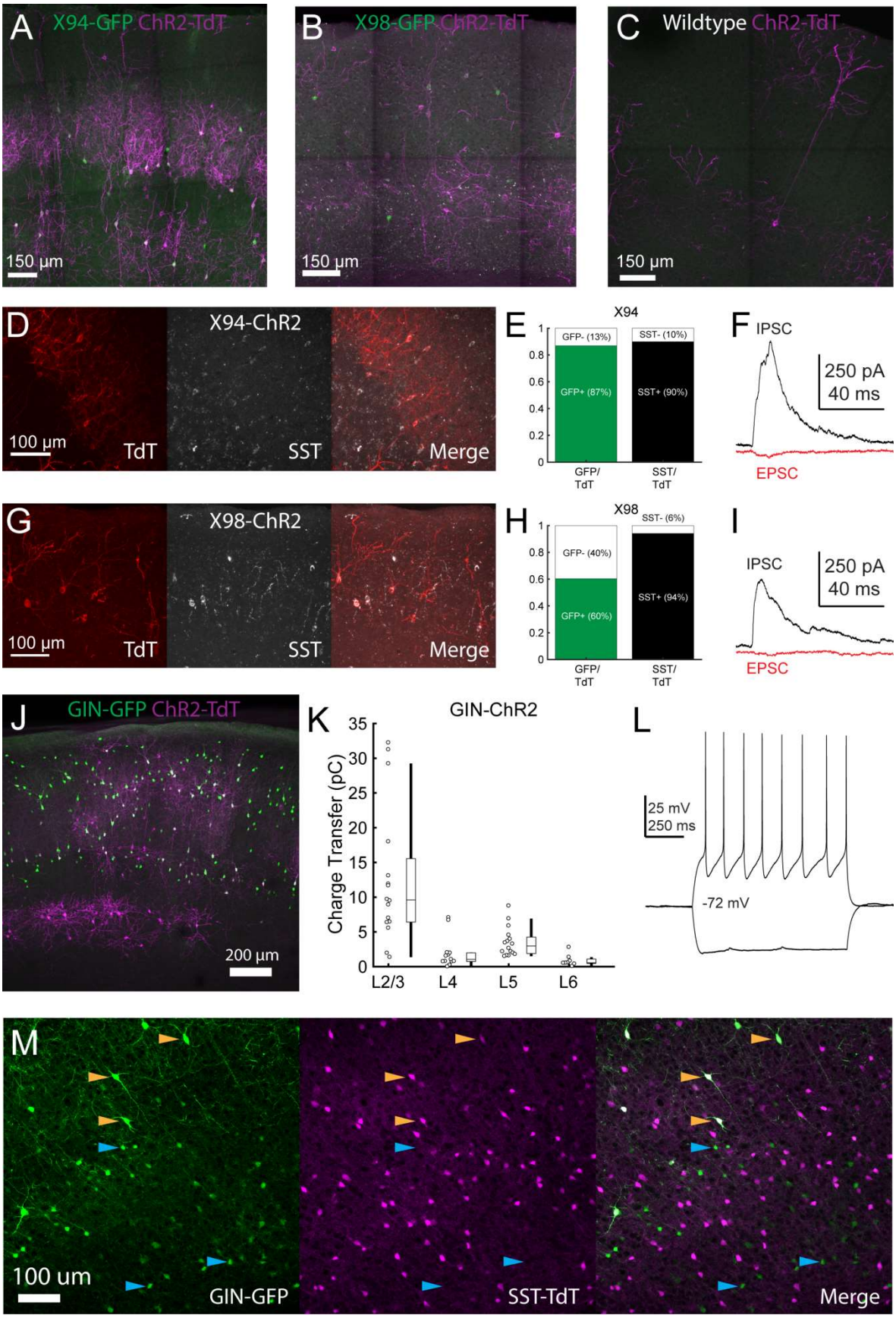

bioRxiv preprint doi: https://doi.org/10.1101/456574; this version posted October 30, 2018. The copyright holder for this preprint (which was not certified by peer review) is the author/funder, who has granted bioRxiv a license to display the preprint in perpetuity. It is made available under aCC-BY-NC 4.0 International license.

Supplementary Figure 11. Validation of Cre-DOG for optogenetic manipulation of SST subtypes in X94, GIN, and X98 mice; related to Figure 5.

(A) Max projection of confocal images of barrel cortex of an X94 mouse injected with Cre-DOG AAVs (AAV2/8. EF1a.C-CreintG WPRE.hGH and AAV2/8. EF1a. N-Cretrcintc WPRE.hGH) along with AAV9.CAGGS.Flex.ChR2-tdTomato.WPRE.SV40 showing expression of GFP (green) and ChR2-TdT (magenta) expression.

(B) As in A, but for an X98 mouse.

(C) As in A, but for a wildtype mouse.

(D) Immunohistochemical staining for SST in X94-ChR2 mice. Left: ChR2-TdT expression (red). Middle: SST staining (white) Right: Merge

(E) Quantification of the fraction of TdT+ cells in which GFP (left, green bar) and SST (right, black bar) was observed.

(F) Example EPSC and IPSC traces recorded in an L4 neuron during photostimulation in a slice from an X94-ChR2 mouse.

(G - I) As in D - F, but for X98-ChR2 mice.

(J) Max projection of a confocal image from a GIN mouse injected with Cre-DOG AAVs (AAV2/8. EF1a.C-CreintG WPRE.hGH and AAV2/8. EF1a. N-Cretrcintc WPRE.hGH) along with AAV9.CAGGS.Flex.ChR2-tdTomato.WPRE.SV40 showing expression of GFP (green) and ChR2-TdT (magenta) expression.

(K) Median charge transfer of evoked IPSCs in each PC recorded in GIN-ChR2 slices, grouped by layer and accompanied by box and whisker plots.

(L) Example current injection traces from an L6, TdT+ non-Martinotti neuron recorded in a GIN-ChR2 slice.

(M) Confocal images from a triple transgenic GIN; SST-TdT animal. Left: GFP (green). Middle: TdT (magenta). Right: merge. Yellow arrows indicate TdT+ cells with bright GFP expression, which are likely MCs. Blue arrows indicate TdT- cells with dimmer GFP expression, which are preferentially located in L6.

bioRxiv preprint doi: https://doi.org/10.1101/456574; this version posted October 30, 2018. The copyright holder for this preprint (which was not certified by peer review) is the author/funder, who has granted bioRxiv a license to display the preprint in perpetuity. It is made available under aCC-BY-NC 4.0 International license.

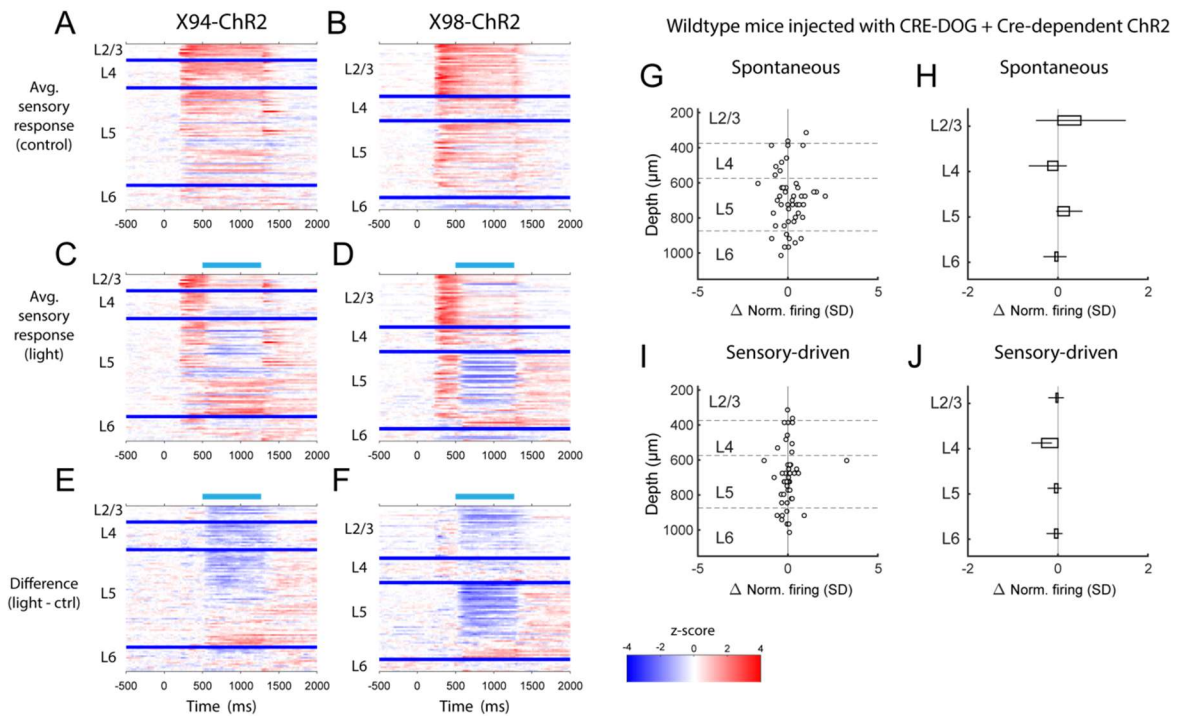

Supplementary Figure 12. PSTHs of RS unit sensory responses during *in vivo* optogenetic manipulation of MCs and NMCs; related to Figure 6

(A) Heatmaps showing the mean normalized firing rate of all RS units recorded in X94-ChR2 mice during sensory stimulation, in the absence of optogenetic stimulation. Each row represents a single unit, and units are grouped according to the layer in which they were recorded. Within each layer group, units are sorted based on the degree to which they are modulated by optogenetic stimulation. Thick blue bars indicate divisions between layers.

(B) As in A, but for RS units recorded in X98-ChR2 mice.

(C) Heatmaps showing the mean normalized firing rate of all RS units recorded in X94-ChR2 mice during sensory stimulation along with optogenetic stimulation. Units are arranged as in A. Light blue bar indicates the period when optogenetic stimulation occurred.

(D) As in C, but for RS units recorded in X98-ChR2 mice.

(E) Heatmaps showing the difference in the mean normalized firing rate of all RS units recorded in X94-ChR2 mice between sensory stimulation with and without optogenetic stimulation, e.g. panel C subtracted from panel A.

(F) As in E, but for RS units recorded in X98-ChR2 mice.

bioRxiv preprint doi: https://doi.org/10.1101/456574; this version posted October 30, 2018. The copyright holder for this preprint (which was not certified by peer review) is the author/funder, who has granted bioRxiv a license to display the preprint in perpetuity. It is made available under aCC-BY-NC 4.0 International license.

(G) Change in normalized spontaneous firing of RS units versus depth below pia for wildtype mice injected with the same viral cocktail as X94/X98-ChR2 mice

(H) Mean change in normalized spontaneous firing rate by layer for wildtype mice. Errorbars indicate 95% confidence interval. No significant effects were observed in any layer.

(I) As in G, but during sensory-driven activity.

(J) As in H, but during sensory-driven activity. No significant effects were observed in any layer.

bioRxiv preprint doi: https://doi.org/10.1101/456574; this version posted October 30, 2018. The copyright holder for this preprint (which was not certified by peer review) is the author/funder, who has granted bioRxiv a license to display the preprint in perpetuity. It is made available under aCC-BY-NC 4.0 International license.

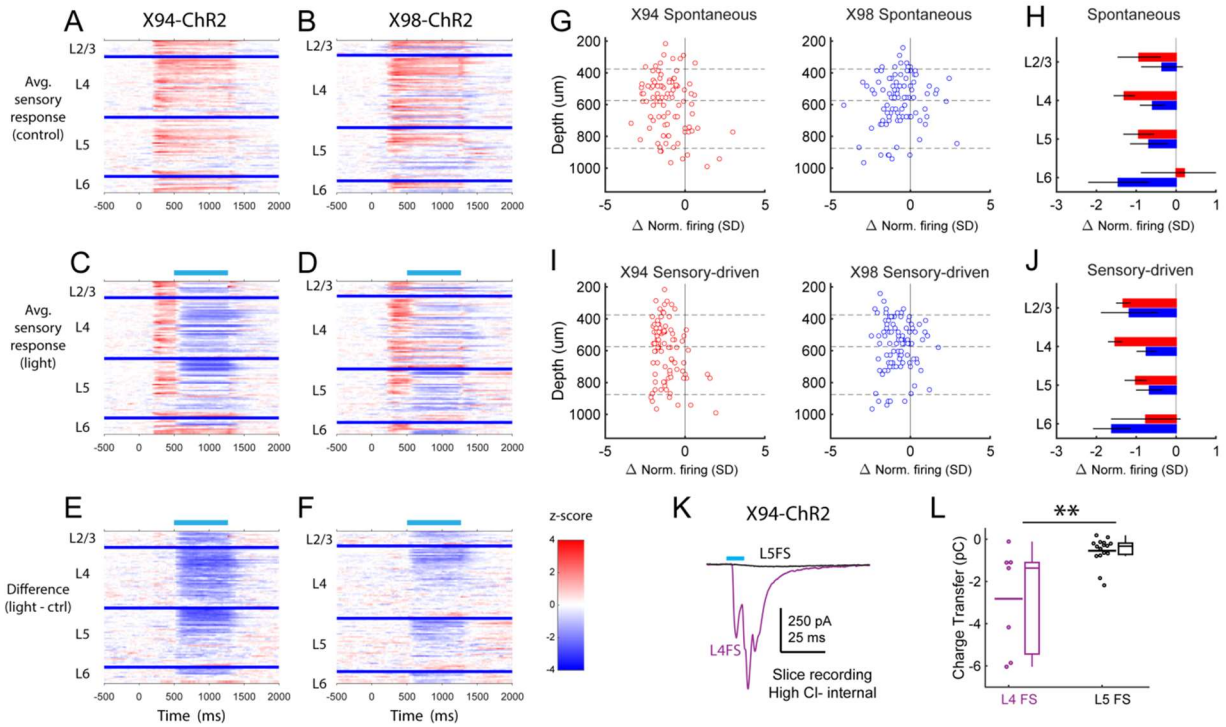

Supplementary Figure 13. PSTHs of FS unit sensory responses during *in vivo* optogenetic manipulation of MCs and NMCs; related to Figure 6

(A) Heatmaps showing the mean normalized firing rate of all FS units recorded in X94-ChR2 mice during sensory stimulation, in the absence of optogenetic stimulation. Each row represents a single unit, and units are grouped according to the layer in which they were recorded. Within each layer group, units are sorted based on the degree to which they are modulated by optogenetic stimulation. Thick blue bars indicate divisions between layers.

(B) As in A, but for FS units recorded in X98-ChR2 mice.

(C) Heatmaps showing the mean normalized firing rate of all FS units recorded in X94-ChR2 mice during sensory stimulation along with optogenetic stimulation. Units are arranged as in A. Light blue bar indicates the period when optogenetic stimulation occurred.

(D) As in C, but for FS units recorded in X98-ChR2 mice.

(E) Heatmaps showing the difference in the mean normalized firing rate of all FS units recorded in X94-ChR2 mice between sensory stimulation with and without optogenetic stimulation, e.g. panel C subtracted from panel A.

(F) As in E, but for FS units recorded in X98-ChR2 mice.

bioRxiv preprint doi: https://doi.org/10.1101/456574; this version posted October 30, 2018. The copyright holder for this preprint (which was not certified by peer review) is the author/funder, who has granted bioRxiv a license to display the preprint in perpetuity. It is made available under aCC-BY-NC 4.0 International license.

(G) Change in normalized spontaneous firing of FS units versus depth below pia for X94-ChR2 (left, red) and X98-ChR2 (right, blue) mice.

(H) Mean change in normalized firing rate by layer for X94-ChR2 (red bars) and X98-ChR2 (blue bars). Errorbars indicate 95% confidence interval.

(I) As in G, but during sensory stimulation.

(J) As in H, but during sensory stimulation.

(K) Examples of L4 (purple) and L5 (black) FS cells recorded in X94-ChR2 slices under pharmacological blockade of glutamate. Traces show the average response to X94-ChR2 stimulation, which occurs during the light blue bar. Cells were recorded using a high chloride internal solution and voltage clamped at -70 mV; inward synaptic currents presumably reflect monosynaptic GABAergic conductances.

(L) Under the conditions described in K, X94-ChR2 stimulation evoked a significantly larger amount of charge transfer in L4 FS cells ($n = 7$) than in L5 FS cells ($n = 16$; $p = 0.0021$, student's T-test).

bioRxiv preprint doi: https://doi.org/10.1101/456574; this version posted October 30, 2018. The copyright holder for this preprint (which was not certified by peer review) is the author/funder, who has granted bioRxiv a license to display the preprint in perpetuity. It is made available under aCC-BY-NC 4.0 International license.

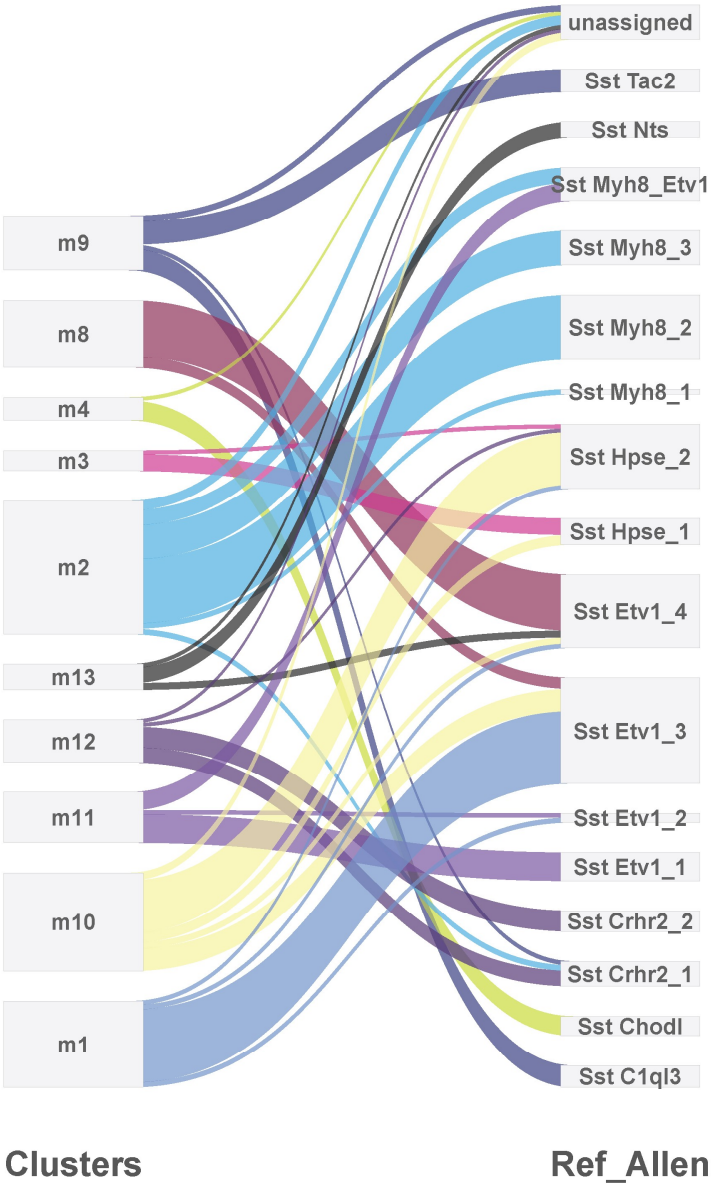

Supplementary Figure 14. Comparison of cortical SST neuron clusters predicted by two independent analyses. Clusters predicted from the single-cell RNA-sequencing experiments described here (left) were compared to the clusters identified in an analysis of SST neurons by Tasic et al. (2017) (right) using the method described in [101]. The differences in outputs can mostly be accounted for by the splitting of the clusters identified in the present analysis, which could be due to the different sequencing platforms used (droplet-based 3' end sequencing vs. full coverage Smart-seq), sequencing depth (low vs. high), and/or cortical area (primary somatosensory cortex vs. primary visual cortex + anterior lateral motor cortex).

bioRxiv preprint doi: https://doi.org/10.1101/456574; this version posted October 30, 2018. The copyright holder for this preprint (which was not certified by peer review) is the author/funder, who has granted bioRxiv a license to display the preprint in perpetuity. It is made available under aCC-BY-NC 4.0 International license.

	GIN + X94			GIN + X94 + classified SST-TdT			All SST-TdT
	MCs	NMCs	p	MCs	NMCs	p	
L5SST→L4PC	**4/47 9%**	**21/34 62%**	$1.6 \cdot 10^{-4}$	**4/68 6%**	**36/67 54%**	$2.0 \cdot 10^{-5}$	**15/55 27%**
L4PC→L5SST	**0/50 0%**	**13/27 48%**	$5.8 \cdot 10^{-4}$	**1/95 1%**	**39/72 54%**	$<10^{-5}$	**27/91 30%**
L5SST→L5PC	**19/38 50%**	**1/38 3%**	$2.8 \cdot 10^{-4}$	**24/46 52%**	**2/65 3%**	$<10^{-5}$	**19/67 28%**
L5PC→L5SST	**2/22 9%**	**0/33 0%**	0.1431	**4/29 14%**	**1/60 2%**	0.02	**5/55 9%**

Supplementary Table 1. Connection rates for MCs and NMCs recorded in different transgenic lines; related to Figure 4. Left columns show paired recording data collected using the GIN and X94 lines to respectively target MCs and NMCs in L5. Right columns show the same data and additionally include data collected using the SST-TdT line, with L5 SST cells classified as putative MCs or NMCs based on their intrinsic properties. Columns not displaying p values show the number and fraction of SST-PC pairs in which a monosynaptic connection was detected for a given condition.

bioRxiv preprint doi: https://doi.org/10.1101/456574; this version posted October 30, 2018. The copyright holder for this preprint (which was not certified by peer review) is the author/funder, who has granted bioRxiv a license to display the preprint in perpetuity. It is made available under aCC-BY-NC 4.0 International license.

	SST-Cre	GIN-GFP	X94-GFP	X98-GFP
L2/3	All SST cells	Dense, MCs	Very sparse	Sparse, MCs
L4	All SST cells	Sparse, NMCs	Dense, NMCs	Very sparse
L5	All SST cells	Moderate, preferentially in 5A, MCs	Moderate, preferentially in 5B, NMCs	Dense, preferentially in L5B, MCs
L6	All SST cells	Sparse, Dim labeling of (non-SST?) cells	Sparse, preferentially in upper 6A, NMCs	Moderate

Supplementary Table 2. Summary of expression in SST reporter lines. Four mouse reporter lines were used in this study to target SST neurons and subtypes. Each row provides a description of the expression observed in the barrel cortex in a particular layer for each reported line.

bioRxiv preprint doi: https://doi.org/10.1101/456574; this version posted October 30, 2018. The copyright holder for this preprint (which was not certified by peer review) is the author/funder, who has granted bioRxiv a license to display the preprint in perpetuity. It is made available under aCC-BY-NC 4.0 International license.

References

1. Feldmeyer, D. Excitatory neuronal connectivity in the barrel cortex. *Front. Neuroanat.* **6,** 24 (2012).
2. Harris, K. D. & Shepherd, G. M. G. The neocortical circuit: themes and variations. *Nat. Neurosci.* **18,** 170–181 (2015).
3. Adesnik, H., Bruns, W., Taniguchi, H., Huang, Z. J. & Scanziani, M. A neural circuit for spatial summation in visual cortex. *Nature* **490,** 226–31 (2012).
4. Kim, D. *et al.* Distinct Roles of Parvalbumin- and Somatostatin- Expressing Interneurons in Working Memory Article Distinct Roles of Parvalbumin- and Somatostatin-Expressing Interneurons in Working Memory. *Neuron* **92,** 1–14 (2016).
5. Kvitsiani, D. *et al.* Distinct behavioural and network correlates of two interneuron types in prefrontal cortex. *Nature* **498,** 363–6 (2013).
6. Makino, H. *et al.* Learning enhances the relative impact of top-down processing in the visual cortex. *Nat Neurosci* **18,** 1116–1122 (2015).
7. Urban-Ciecko, J. & Barth, A. L. Somatostatin-expressing neurons in cortical networks. *Nat. Rev. Neurosci.* **17,** 401–9 (2016).
8. Kato, H. K., Asinof, S. K. & Isaacson, J. S. Network-Level Control of Frequency Tuning in Auditory Cortex. *Neuron* **95,** 412–423.e4 (2017).
9. Veit, J., Hakim, R., Jadi, M. P., Sejnowski, T. J. & Adesnik, H. Cortical gamma band synchronization through somatostatin interneurons. *Nat. Neurosci.* **20,** 951–959 (2017).
10. Adesnik, H. Synaptic Mechanisms of Feature Coding in the Visual Cortex of Awake Mice. *Neuron* **95,** 1147–1159.e4 (2017).
11. Apicella, A. J., Wickersham, I. R., Seung, H. S. & Shepherd, G. M. G. Laminarly orthogonal excitation of fast-spiking and low-threshold-spiking interneurons in mouse motor cortex. *J. Neurosci.* **32,** 7021–33 (2012).
12. Jiang, X. *et al.* Principles of connectivity among morphologically defined cell types in adult neocortex. *Science (80-.).* **350,** aac9462-aac9462 (2015).
13. Jiang, X., Wang, G., Lee, A. J., Stornetta, R. L. & Zhu, J. J. The organization of two new cortical interneuronal circuits. *Nat. Neurosci.* **16,** 210–8 (2013).
14. Anastasiades, P. G. *et al.* GABAergic interneurons form transient layer-specific circuits in early postnatal neocortex. *Nat. Commun.* **7,** 10584 (2016).
15. Otsuka, T. & Kawaguchi, Y. Cortical inhibitory cell types differentially form intralaminar and interlaminar subnetworks with excitatory neurons. *J. Neurosci.* **29,** 10533–40 (2009).
16. Yoshimura, Y. & Callaway, E. M. Fine-scale specificity of cortical networks depends on inhibitory cell type and connectivity. *Nat. Neurosci.* **8,** 1552–9 (2005).
17. Kapfer, C., Glickfeld, L. L., Atallah, B. V & Scanziani, M. Supralinear increase of recurrent inhibition during sparse activity in the somatosensory cortex. *Nat.*

bioRxiv preprint doi: https://doi.org/10.1101/456574; this version posted October 30, 2018. The copyright holder for this preprint (which was not certified by peer review) is the author/funder, who has granted bioRxiv a license to display the preprint in perpetuity. It is made available under aCC-BY-NC 4.0 International license.

Neurosci. **10,** 743–53 (2007).

18. Fino, E. & Yuste, R. Dense inhibitory connectivity in neocortex. *Neuron* **69,** 1188–203 (2011).
19. Bock, D. D. *et al.* Network anatomy and in vivo physiology of visual cortical neurons. *Nature* **471,** 177–82 (2011).
20. Scholl, B., Pattadkal, J. J., Dilly, G. A., Priebe, N. J. & Zemelman, B. V. Local Integration Accounts for Weak Selectivity of Mouse Neocortical Parvalbumin Interneurons. *Neuron* **87,** 424–437 (2015).
21. Hofer, S. B. *et al.* Differential connectivity and response dynamics of excitatory and inhibitory neurons in visual cortex. *Nat. Neurosci.* **14,** 1045–1052 (2011).
22. Packer, A. M. & Yuste, R. Dense, unspecific connectivity of neocortical parvalbumin-positive interneurons: a canonical microcircuit for inhibition? *J. Neurosci.* **31,** 13260–13271 (2011).
23. Yavorska, I. & Wehr, M. Somatostatin-Expressing Inhibitory Interneurons in Cortical Circuits. *Front. Neural Circuits* **10,** 1–18 (2016).
24. Tasic, B. *et al.* Adult mouse cortical cell taxonomy revealed by single cell transcriptomics. *Nat. Neurosci.* **advance on,** 1–37 (2016).
25. Muñoz, W., Tremblay, R., Levenstein, D. & Rudy, B. Layer-specific modulation of neocortical dendritic inhibition during active wakefulness. *Science (80-.).* **355,** 954 LP-959 (2017).
26. Ma, W. *et al.* Visual representations by cortical somatostatin inhibitory neurons--selective but with weak and delayed responses. *J. Neurosci.* **30,** 14371–9 (2010).
27. Reimer, J. *et al.* Pupil Fluctuations Track Fast Switching of Cortical States during Quiet Wakefulness. *Neuron* **84,** 355–362 (2014).
28. Nakajima, M., Görlich, A. & Heintz, N. Oxytocin modulates female sociosexual behavior through a specific class of prefrontal cortical interneurons. *Cell* **159,** 295–305 (2014).
29. Ma, Y., Hu, H., Berrebi, A. S., Mathers, P. H. & Agmon, A. Distinct subtypes of somatostatin-containing neocortical interneurons revealed in transgenic mice. *J. Neurosci.* **26,** 5069–82 (2006).
30. Muñoz, W., Tremblay, R. & Rudy, B. Channelrhodopsin-Assisted Patching: InVivo Recording of Genetically and Morphologically Identified Neurons throughout the Brain. *Cell Rep.* **9,** 2304–2316 (2014).
31. José Nigro, M., Hashikawa, Y. & Rudy, B. Diversity and connectivity of layer 5 somatostatin-expressing interneurons in the mouse barrel cortex. *J. Neurosci.* **38,** 2415–17 (2018).
32. Taniguchi, H. *et al.* A Resource of Cre Driver Lines for Genetic Targeting of GABAergic Neurons in Cerebral Cortex. *Neuron* **71,** 995–1013 (2011).
33. Oliva, a a, Jiang, M., Lam, T., Smith, K. L. & Swann, J. W. Novel hippocampal interneuronal subtypes identified using transgenic mice that express green

bioRxiv preprint doi: https://doi.org/10.1101/456574; this version posted October 30, 2018. The copyright holder for this preprint (which was not certified by peer review) is the author/funder, who has granted bioRxiv a license to display the preprint in perpetuity. It is made available under aCC-BY-NC 4.0 International license.

fluorescent protein in GABAergic interneurons. *J. Neurosci.* **20,** 3354–3368 (2000).

34. Markram, H. *et al.* Interneurons of the neocortical inhibitory system. *Nat. Rev. Neurosci.* **5,** 793–807 (2004).

35. Rudy, B., Fishell, G., Lee, S. & Hjerling-Leffler, J. Three groups of interneurons account for nearly 100% of neocortical GABAergic neurons. *Dev. Neurobiol.* **71,** 45–61 (2011).

36. Wang, Y. *et al.* Anatomical, physiological and molecular properties of Martinotti cells in the somatosensory cortex of the juvenile rat. *J. Physiol.* **561,** 65–90 (2004).

37. Kawaguchi, Y. Groupings of nonpyramidal and pyramidal cells with specific physiological and morphological characteristics in rat frontal cortex. *J. Neurophysiol.* **69,** 416–431 (1993).

38. Fanselow, E. E., Richardson, K. A. & Connors, B. W. Selective , State-Dependent Activation of Somatostatin-Expressing Inhibitory Interneurons in Mouse Neocortex. *J. Neurophysiol.* **100,** 2640–2652 (2008).

39. Kinnischtzke, A. K., Sewall, A. M., Berkepile, J. M. & Fanselow, E. E. Postnatal maturation of somatostatin-expressing inhibitory cells in the somatosensory cortex of GIN mice. *Front. Neural Circuits* **6,** 33 (2012).

40. Silberberg, G. & Markram, H. Disynaptic inhibition between neocortical pyramidal cells mediated by Martinotti cells. *Neuron* **53,** 735–46 (2007).

41. Yoshimura, Y., Dantzker, J. & Callaway, E. Excitatory cortical neurons form fine-scale functional networks. *Nature* **433,** (2005).

42. Morgenstern, N. A., Bourg, J. & Petreanu, L. Multilaminar networks of cortical neurons integrate common inputs from sensory thalamus. *Nat. Neurosci.* **19,** 1034–40 (2016).

43. Merel, J., Shababo, B., Naka, A., Adesnik, H. & Paninski, L. Bayesian methods for event analysis of intracellular currents. *J. Neurosci. Methods* **269,** 21–32 (2016).

44. Baker, C. A., Elyada, Y. M., Parra-Martin, A. & Bolton, M. Cellular resolution circuit mapping in mouse brain with temporal-focused excitation of soma-targeted channelrhodopsin. *Elife* **5,** 1–15 (2016).

45. Amarasingham, A., Harrison, M. T., Hatsopoulos, N. G. & Geman, S. Conditional modeling and the jitter method of spike resampling. *J. Neurophysiol.* **107,** 517–31 (2012).

46. Beierlein, M., Gibson, J. R. & Connors, B. W. Two dynamically distinct inhibitory networks in layer 4 of the neocortex. *J. Neurophysiol.* **90,** 2987–3000 (2003).

47. Berger, T. K., Perin, R., Silberberg, G. & Markram, H. Frequency-dependent disynaptic inhibition in the pyramidal network: a ubiquitous pathway in the developing rat neocortex. *J. Physiol.* **587,** 5411–25 (2009).

48. Xu, H., Jeong, H. Y., Tremblay, R. & Rudy, B. Neocortical Somatostatin-Expressing GABAergic Interneurons Disinhibit the Thalamorecipient Layer 4. *Neuron* **77,** 155–167 (2013).

49. Beierlein, M., Gibson, J. R. & Connors, B. W. A network of electrically coupled

bioRxiv preprint doi: https://doi.org/10.1101/456574; this version posted October 30, 2018. The copyright holder for this preprint (which was not certified by peer review) is the author/funder, who has granted bioRxiv a license to display the preprint in perpetuity. It is made available under aCC-BY-NC 4.0 International license.

interneurons drives synchronized inhibition in neocortex. *Nat. Neurosci.* **3,** 904–10 (2000).

50. Petersen, C. C. H. & Sakmann, B. The excitatory neuronal network of rat layer 4 barrel cortex. *J. Neurosci.* **20,** 7579–7586 (2000).
51. Berger, T. K., Silberberg, G., Perin, R. & Markram, H. Brief bursts self-inhibit and correlate the pyramidal network. *PLoS Biol.* **8,** (2010).
52. Levy, R. B. & Reyes, A. D. Spatial profile of excitatory and inhibitory synaptic connectivity in mouse primary auditory cortex. *J. Neurosci.* **32,** 5609–19 (2012).
53. Tang, J. C. Y. *et al.* Cell type–specific manipulation with GFP-dependent Cre recombinase. *Nat. Neurosci.* **18,** 1334–1341 (2015).
54. Lee, A. J. *et al.* Canonical Organization of Layer 1 Neuron-Led Cortical Inhibitory and Disinhibitory Interneuronal Circuits. *Cereb. Cortex* **2,** 1–13 (2014).
55. Pluta, S. *et al.* A direct translaminar inhibitory circuit tunes cortical output. *Nat Neurosci* **18,** 1631–1640 (2015).
56. Morishima, M., Kobayashi, K., Kato, S., Kobayashi, K. & Kawaguchi, Y. Segregated Excitatory–Inhibitory Recurrent Subnetworks in Layer 5 of the Rat Frontal Cortex. *Cereb. Cortex* 1–12 (2017). doi:10.1093/cercor/bhx276
57. Tasic, B. *et al.* Shared and distinct transcriptomic cell types across neocortical areas. *bioRxiv* 229542 (2017). doi:10.1101/229542
58. Paul, A. *et al.* Transcriptional Architecture of Synaptic Communication Delineates GABAergic Neuron Identity. *Cell* **0,** 5471–5490 (2016).
59. Wimmer, V. C., Bruno, R. M., de Kock, C. P. J., Kuner, T. & Sakmann, B. Dimensions of a Projection Column and Architecture of VPM and POm Axons in Rat Vibrissal Cortex. *Cereb. Cortex* **20,** 2265–2276 (2010).
60. Urban-Ciecko, J., Fanselow, E. E. & Barth, A. L. Neocortical somatostatin neurons reversibly silence excitatory transmission via GABAb receptors. *Curr. Biol.* **25,** 722–731 (2015).
61. Tan, Z., Hu, H., Huang, Z. J. & Agmon, A. Robust but delayed thalamocortical activation of dendritic-targeting inhibitory interneurons. *Proc. Natl. Acad. Sci. U. S. A.* **105,** 2187–2192 (2008).
62. Hu, H. & Agmon, A. Differential Excitation of Distally versus Proximally Targeting Cortical Interneurons by Unitary Thalamocortical Bursts. *J. Neurosci.* **36,** 6906–6916 (2016).
63. Ji, X. Y. *et al.* Thalamocortical Innervation Pattern in Mouse Auditory and Visual Cortex: Laminar and Cell-Type Specificity. *Cereb. Cortex* **26,** 2612–2625 (2016).
64. Kinnischtzke, A. K., Simons, D. J. & Fanselow, E. E. Motor Cortex Broadly Engages Excitatory and Inhibitory Neurons in Somatosensory Barrel Cortex. *Cereb. Cortex* **24,** 1–12 (2014).
65. Cruikshank, S. J., Urabe, H., Nurmikko, A. V & Connors, B. W. Pathway-Specific Feedforward Circuits between Thalamus and Neocortex Revealed by Selective

bioRxiv preprint doi: https://doi.org/10.1101/456574; this version posted October 30, 2018. The copyright holder for this preprint (which was not certified by peer review) is the author/funder, who has granted bioRxiv a license to display the preprint in perpetuity. It is made available under aCC-BY-NC 4.0 International license.

Optical Stimulation of Axons. *Neuron* **65,** 230–245 (2010).

66. Larkum, M. A cellular mechanism for cortical associations: an organizing principle for the cerebral cortex. *Trends Neurosci.* **36,** 141–51 (2013).

67. Lee, S., Kruglikov, I., Huang, Z. J., Fishell, G. & Rudy, B. A disinhibitory circuit mediates motor integration in the somatosensory cortex. *Nat. Neurosci.* **16,** 1662–70 (2013).

68. Pfeffer, C. K., Xue, M., He, M., Huang, Z. J. & Scanziani, M. Inhibition of inhibition in visual cortex: the logic of connections between molecularly distinct interneurons. *Nat. Neurosci.* **16,** 1068–76 (2013).

69. Pi, H.-J. *et al.* Cortical interneurons that specialize in disinhibitory control. *Nature* **503,** 521–4 (2013).

70. Polack, P.-O. & Contreras, D. Long-range parallel processing and local recurrent activity in the visual cortex of the mouse. *J. Neurosci.* **32,** 11120–31 (2012).

71. Xiang, Z., Huguenard, J. R. & Prince, D. a. Cholinergic Switching Within Neocortical Inhibitory Networks. *Science (80-.).* **281,** 985–988 (1998).

72. He, M. *et al.* Strategies and tools for combinatorial targeting of GABAergic neurons in mouse cerebral cortex. *Neuron* 1–16 (2016). doi:10.1016/j.neuron.2016.08.021

73. Xu, X., Roby, K. D. & Callaway, E. M. Mouse cortical inhibitory neuron type that coexpresses somatostatin and calretinin. *J. Comp. Neurol.* **499,** 144–160 (2006).

74. Fairén, A., Cobas, A. & Fonseca, M. Times of generation of glutamic acid decarboxylase immunoreactive neurons in mouse somatosensory cortex. *J. Comp. Neurol.* **251,** 67–83 (1986).

75. Helmstaedter, M., Sakmann, B. & Feldmeyer, D. Neuronal Correlates of Local, Lateral, and Translaminar Inhibition with Reference to Cortical Columns. *Cereb. Cortex* **19,** 926–937 (2009).

76. Kumar, P. & Ohana, O. Inter- and intralaminar subcircuits of excitatory and inhibitory neurons in layer 6a of the rat barrel cortex. *J. Neurophysiol.* **100,** 1909–22 (2008).

77. Porter, J. T., Johnson, C. K. & Agmon, A. Diverse types of interneurons generate thalamus-evoked feedforward inhibition in the mouse barrel cortex. *J. Neurosci.* **21,** 2699–2710 (2001).

78. Cobas, a, Welker, E., Fairén, a, Kraftsik, R. & Van der Loos, H. GABAergic neurons in the barrel cortex of the mouse: an analysis using neuronal archetypes. *J. Neurocytol.* **16,** 843–870 (1987).

79. Fairén, A. Cajal and Lorente de Nó on cortical interneurons: Coincidences and progress. *Brain Res. Rev.* **55,** 430–444 (2007).

80. Lorente de No, R. The Cerebral Cortex of the Mouse. *Somat. Mot. Res.* **9,** 3–36 (1992).

81. Ma, Y., Hu, H. & Agmon, a. Short-Term Plasticity of Unitary Inhibitory-to-Inhibitory Synapses Depends on the Presynaptic Interneuron Subtype. *J. Neurosci.* **32,** 983–988 (2012).

82. Halabisky, B., Shen, F., Huguenard, J. R. & Prince, D. A. Electrophysiological classification of somatostatin-positive interneurons in mouse sensorimotor cortex. *J.*

bioRxiv preprint doi: https://doi.org/10.1101/456574; this version posted October 30, 2018. The copyright holder for this preprint (which was not certified by peer review) is the author/funder, who has granted bioRxiv a license to display the preprint in perpetuity. It is made available under aCC-BY-NC 4.0 International license.

Neurophysiol. **96,** 834–845 (2006).

83. McGarry, L. M. *et al.* Quantitative classification of somatostatin-positive neocortical interneurons identifies three interneuron subtypes. *Front. Neural Circuits* **4,** 12 (2010).

84. Hilscher, M. M., Le, R. N., Edwards, S. J., Le, K. E. & Kullander, K. Chrna2-Martinotti Cells Synchronize layer 5 type A Pyramidal Cells via Rebound Excitation. 1–26 (2016). doi:10.1371/journal.pbio.2001392

85. Yuan, M. *et al.* Somatostatin-positive interneurons in the dentate gyrus of mice provide local-and long-range septal synaptic inhibition. *Elife* **6,** 1–25 (2017).

86. Harris, K. D. *et al.* Classes and continua of hippocampal CA1 inhibitory neurons revealed by single-cell transcriptomics. *bioRxiv* (2018).

87. Muller, C. & Remy, S. Dendritic inhibition mediated by O-LM and bistratified interneurons in the hippocampus. *Front. Synaptic Neurosci.* **6,** 1–15 (2014).

88. Lovett-Barron, M. *et al.* Regulation of neuronal input transformations by tunable dendritic inhibition. *Nat. Neurosci.* **15,** 423–30, S1-3 (2012).

89. Sekerli, M., Del Negro, C. A., Lee, R. H. & Butera, R. J. Estimating action potential thresholds from neuronal time-series: New metrics and evaluation of methodologies. *IEEE Trans. Biomed. Eng.* **51,** 1665–1672 (2004).

90. Hattox, A. M. & Nelson, S. B. Layer V neurons in mouse cortex projecting to different targets have distinct physiological properties. *J. Neurophysiol.* **98,** 3330–3340 (2007).

91. Kim, E. J., Juavinett, A. L., Kyubwa, E. M., Jacobs, M. W. & Callaway, E. M. Three Types of Cortical Layer 5 Neurons That Differ in Brain-wide Connectivity and Function. *Neuron* **88,** 1253–1267 (2015).

92. Schubert, D. *et al.* Layer-specific intracolumnar and transcolumnar functional connectivity of layer V pyramidal cells in rat barrel cortex. *J. Neurosci.* **21,** 3580–3592 (2001).

93. Hu, H., Cavendish, J. Z. & Agmon, A. Not all that glitters is gold: off-target recombination in the somatostatin–IRES-Cre mouse line labels a subset of fast-spiking interneurons. *Front. Neural Circuits* **7,** 1–4 (2013).

94. Adesnik, H. & Scanziani, M. Lateral competition for cortical space by layer-specific horizontal circuits. *Nature* **464,** 1155–60 (2010).

95. Williams, S. R. & Mitchell, S. J. Direct measurement of somatic voltage clamp errors in central neurons. *Nat. Neurosci.* **11,** 790–8 (2008).

96. Benjamini, Y. & Hochberg, Y. Controlling the False Discovery Rate : A Practical and Powerful Approach to Multiple Testing Author (s): Yoav Benjamini and Yosef Hochberg Source : Journal of the Royal Statistical Society . Series B (Methodological), Vol . 57 , No . 1 Published by : *J. R. Stat. Soc.* **57,** 289–300 (1995).

97. Cole, M. B. *et al.* Performance Assessment and Selection of Normalization Procedures for Single-Cell RNA-Seq. *bioRxiv* 235382 (2017). doi:10.1101/235382

98. Risso, D., Perraudeau, F., Gribkova, S., Dudoit, S. & Vert, J. P. A general and flexible

bioRxiv preprint doi: https://doi.org/10.1101/456574; this version posted October 30, 2018. The copyright holder for this preprint (which was not certified by peer review) is the author/funder, who has granted bioRxiv a license to display the preprint in perpetuity. It is made available under aCC-BY-NC 4.0 International license.

method for signal extraction from single-cell RNA-seq data. *Nat. Commun.* **9,** 1–17 (2018).

99. McCarthy, D. J., Campbell, K. R., Lun, A. T. L. & Wills, Q. F. Scater: Pre-processing, quality control, normalization and visualization of single-cell RNA-seq data in R. *Bioinformatics* **33,** 1179–1186 (2017).

100. Risso, D. *et al.* clusterExperiment and RSEC: A Bioconductor package and framework for clustering of single-cell and other large gene expression datasets. *PLOS Comput. Biol.* **14,** e1006378 (2018).

101. Kiselev, V. Y., Yiu, A. & Hemberg, M. scmap: projection of single-cell RNA-seq data across data sets. *Nat. Methods* **15,** (2018).

102. Gibson, J. R., Beierlein, M. & Connors, B. W. Functional Properties of Electrical Synapses Between Inhibitory Interneurons of Neocortical Layer 4. *J Neurophysiol* **93,** 467–480 (2005).